Article

Reductive carboxylation epigenetically instructs T cell differentiation

https://doi.org/10.1038/s41586-023-06546-y

Received: 8 January 2022

Accepted: 15 August 2023

Published online: 20 September 2023

Check for updates

Alison Jaccard[1,2], Tania Wyss[1,3], Noelia Maldonado-Pérez[4], Jan A. Rath[2,5,6,7], Alessio Bevilacqua[1,2], Jhan-Jie Peng[1,2,8], Anouk Lepez[6,7,9,10], Christine Von Gunten[2,5,6,7], Fabien Franco[1,2], Kung-Chi Kao[1,2], Nicolas Camviel[2,5,6], Francisco Martín[4], Bart Ghesquière[11,12], Denis Migliorini[6,7,9,10,13], Caroline Arber[2,5,6,7], Pedro Romero[1,14] ✉, Ping-Chih Ho[1,2,14] ✉ & Mathias Wenes[1,6,7,9,10,14] ✉

Protective immunity against pathogens or cancer is mediated by the activation and clonal expansion of antigen-specific naive T cells into effector T cells. To sustain their rapid proliferation and effector functions, naive T cells switch their quiescent metabolism to an anabolic metabolism through increased levels of aerobic glycolysis, but also through mitochondrial metabolism and oxidative phosphorylation, generating energy and signalling molecules[1–3]. However, how that metabolic rewiring drives and defines the differentiation of T cells remains unclear. Here we show that proliferating effector CD8$^+$ T cells reductively carboxylate glutamine through the mitochondrial enzyme isocitrate dehydrogenase 2 (IDH2). Notably, deletion of the gene encoding IDH2 does not impair the proliferation of T cells nor their effector function, but promotes the differentiation of memory CD8$^+$ T cells. Accordingly, inhibiting IDH2 during ex vivo manufacturing of chimeric antigen receptor (CAR) T cells induces features of memory T cells and enhances antitumour activity in melanoma, leukaemia and multiple myeloma. Mechanistically, inhibition of IDH2 activates compensating metabolic pathways that cause a disequilibrium in metabolites regulating histone-modifying enzymes, and this maintains chromatin accessibility at genes that are required for the differentiation of memory T cells. These findings show that reductive carboxylation in CD8$^+$ T cells is dispensable for their effector response and proliferation, but that it mainly produces a pattern of metabolites that epigenetically locks CD8$^+$ T cells into a terminal effector differentiation program. Blocking this metabolic route allows the increased formation of memory T cells, which could be exploited to optimize the therapeutic efficacy of CAR T cells.

After antigenic stimulation and expansion, most CD8$^+$ effector T (T_E) cells are short-lived effector cells (SLECs), but a small fraction consists of memory precursor effector cells (MPECs) that will survive in an antigen-independent manner and generate a pool of long-lived central memory T (T_{CM}) cells[4]. The potent cytotoxic nature of CD8$^+$ T cells has led to the development of several cell-based immunotherapies for cancer. These therapies include adoptive cell transfer (ACT), which consists of the ex vivo stimulation, expansion and re-infusion of either naturally occurring tumour-infiltrating lymphocytes (TILs) or genetically engineered autologous T cells, such as CAR T cells. Unfortunately, transferred cells are often terminally differentiated, and thus exhibit a low self-renewing and proliferative potential, resulting in poor therapeutic efficacy. Consistently, the use of T cells with memory features for ACT has been shown to provide more robust and sustained antitumour responses[5,6].

The differentiation of T_E versus memory T (T_M) cells is regulated by cytokines and transcription factors[7,8], as well as by post-translational modifications of histones to epigenetically alter chromatin accessibility[9,10]. In addition, activated CD8$^+$ T cells depend on increased anabolic metabolism to sustain their clonal expansion and effector function. Citrate, produced by the tricarboxylic acid (TCA) cycle, is a major source of cytosolic acetyl-coenzyme A (acetyl-CoA), which is a central metabolite supporting cell growth and function, by serving as a precursor of lipid synthesis and as a donor for acetylation[11].

[1]Department of Oncology, University of Lausanne, Lausanne, Switzerland. [2]Ludwig Institute for Cancer Research Lausanne, University of Lausanne, Épalinges, Switzerland. [3]Translational Data Science (TDS) Group, AGORA Cancer Research Center, Swiss Institute of Bioinformatics (SIB), Lausanne, Switzerland. [4]Department of Genomic Medicine, Pfizer-University of Granada-Junta de Andalucía, Centre for Genomics and Oncological Research (GENYO), Granada, Spain. [5]Department of Oncology, Lausanne University Hospital and University of Lausanne, Lausanne, Switzerland. [6]AGORA Cancer Research Center, Lausanne, Switzerland. [7]Swiss Cancer Center Léman, Lausanne, Switzerland. [8]Center for Molecular and Clinical Immunology, Chang Gung University, Taoyuan, Taiwan. [9]Brain Tumor and Immune Cell Engineering Group, Faculty of Medicine, University of Geneva, Geneva, Switzerland. [10]Center for Translational Research in Onco-Hematology, University of Geneva, Geneva, Switzerland. [11]Metabolomics Expertise Center, Center for Cancer Biology, VIB, KU Leuven, Leuven, Belgium. [12]Laboratory of Applied Mass Spectrometry, Department of Cellular and Molecular Medicine, KU Leuven, Leuven, Belgium. [13]Department of Oncology, Geneva University Hospitals (HUG), Geneva, Switzerland. [14]These authors jointly supervised this work: Pedro Romero, Ping-Chih Ho, Mathias Wenes. ✉e-mail: pedro.romero@unil.ch; ping-chih.ho@unil.ch; mathias.wenes@unige.ch

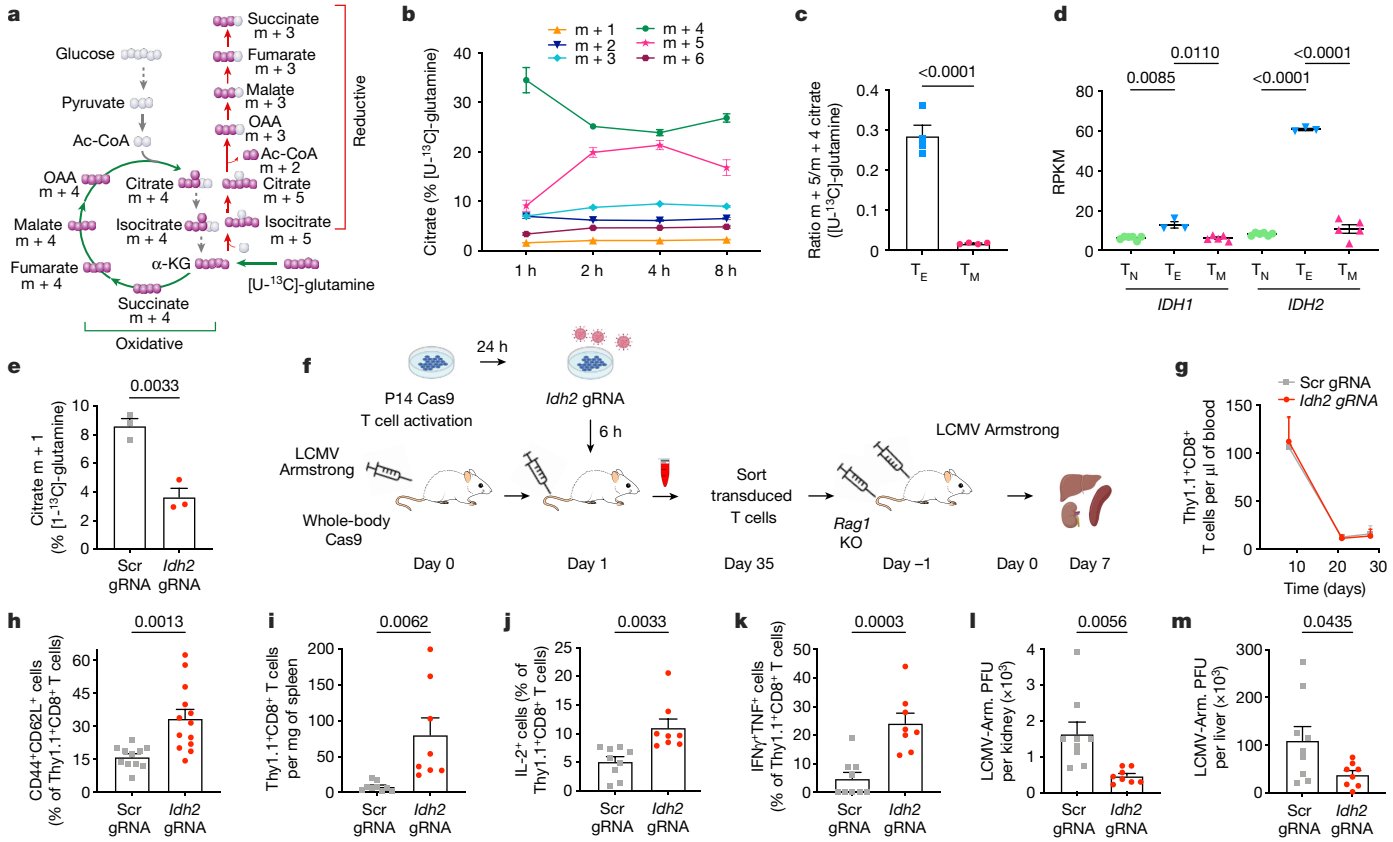

Fig. 1 | Deletion of *IDH2* inhibits RC in T_E cells and promotes the differentiation of T_M cells. a, Oxidative (green) and reductive (red) glutamine metabolism. Ac-CoA, acetyl-CoA; OAA, oxaloacetate. **b**, Citrate mass isotopologues in mouse $CD8^+$ T_E cells labelled with [U-^{13}C]-glutamine ($n = 3$ biological replicates). **c**, Ratio of m + 5 to m + 4 citrate detected by [U-^{13}C]-glutamine labelling in T_E or T_M cells ($n = 4$ biological replicates). **d**, Gene expression of *IDH1* and *IDH2* in $CD8^+$ T cells from volunteers who were vaccinated against yellow fever. Data are reads per kilobase of transcript per million reads mapped (RPKM) in the indicated cell subsets ($n = 3$ (T_E), $n = 5$ (T_M) and $n = 6$ (T_N) biological replicates). **e**, Percentage of m + 1 citrate labelling from [1-^{13}C]-glutamine in control scramble (Scr) gRNA-transduced cells or IDH2-deficient cells ($n = 3$ biological replicates). **f**, Schematic representation of the experiment. D, day. **g**, Number of Thy1.1$^+$ cells per microlitre of blood. **h**, Percentage of $CD44^+CD62L^+$ cells among Thy1.1$^+$ cells in the blood 28 days after infection. **i**, Number of Thy1.1$^+$ cells per milligram of spleen seven days after secondary challenge. **j**,**k**, Percentages of IL-2$^+$ (**j**) and IFNγ$^+$TNF$^+$ (**k**) cells among Thy1.1$^+$ cells after restimulation seven days after secondary challenge. **l**,**m**, LCMV-Armstrong viral titres per kidney (**l**) and liver (**m**). PFU, plaque-forming units. In **g**,**h**: $n = 13$ (*Idh2* gRNA) and $n = 11$ (Scr gRNA) biological replicates; pooled data from three independent experiments. In **i**–**m**: $n = 8$ (*Idh2* gRNA) and $n = 9$ (Scr gRNA) biological replicates; pooled data from two independent experiments. Data are mean ± s.e.m. and were analysed by one-way ANOVA using Tukey's multiple comparison test (**d**) or unpaired, two-tailed Student's *t*-test (**c**,**e**,**h**–**m**). The *P* value in **c** is 0.00005633.

Although citrate is mainly produced by the oxidation of pyruvate, fatty acids or amino acids, studies in cancer cells under hypoxia or with mitochondrial defects have shown that reductive carboxylation of glutamine (RC) is an indispensable contributor to the citrate pool[12,13]. RC can be mediated by two enzymes in mammalian cells: the $NADP^+$-dependent isocitrate dehydrogenase (IDH) 1 in the cytosol and IDH2 in the mitochondria[12]. Mutations in IDH1 or IDH2 in different cancer types lead to the production of the oncometabolite 2-hydroxyglutarate (2-HG), which induces epigenetic changes that drive oncogenesis[14]. A third IDH isoform (IDH3) is mitochondrial, NAD^+-dependent and only able to catalyse the oxidative reaction[15]. Although it has been suggested that $CD8^+$ T cells could reductively metabolize glutamine to lipids under hypoxia[13], how this affects the function and differentiation of T_E cells remains unknown.

T_E cells reductively carboxylate glutamine

To investigate oxidative versus reductive glutamine use in highly proliferating T_E-like $CD8^+$ T cells, we performed an in vitro kinetic labelling of [U-^{13}C]-glutamine in T cells three days after activation (Fig. 1a and Extended Data Fig. 1a). The accumulation of m + 4 metabolites versus m + 5 citrate and m + 3 malate, fumarate, succinate and aspartate identifies oxidative glutamine metabolism versus RC, respectively (Fig. 1a). In T_E cells, oxidative and reductive labelling into citrate quickly equilibrates (Fig. 1b), whereas RC in T_M cells (T_E cells cultured for four extra days in IL-15; Extended Data Fig. 1a) was barely detectable (Extended Data Fig. 1b). Consistently, T_E cells showed significantly higher levels of aspartate, malate and fumarate derived from reductive metabolism than did T_M cells (Extended Data Fig. 1c–e), and the ratios of reductive over oxidative metabolites were much higher in T_E than in T_M cells (Fig. 1c and Extended Data Fig. 1f–h). RC produces acetyl-CoA species for lipid biosynthesis[13], and, accordingly, we observed higher levels of glutamine labelling into fatty acids in T_E than in T_M cells (Extended Data Fig. 1i–k). In general, T_E cells consumed more glutamine and were more proliferative than T_M cells (Extended Data Fig. 1l,m).

To investigate which IDH isoform mediates RC in T cells, we analysed publicly available RNA sequencing (RNA-seq) data from human yellow-fever-tetramer-positive $CD8^+$ naive T (T_N), T_E and T_M cells from the blood of healthy volunteers who had been vaccinated with the yellow fever vaccine[16] (Extended Data Fig. 1n). The expression of all IDH isoforms was induced in T_E cells compared to T_N and T_M cells, which can be explained by the fact that T_E cells are highly metabolically active. However, among the IDH isoforms, the expression of IDH2 showed by far the highest fold-change increase (Fig. 1d and Extended Data Fig. 1o). We next characterized IDH gene expression in mouse

ovalbumin (OVA)-specific T cell subsets over the course of a transient bacterial infection with *Listeria monocytogenes* expressing OVA (LM-OVA). SLECs and MPECs were isolated seven days after infection and effector memory T (T_{EM}, $CD44^+CD62L^-$) and T_{CM} ($CD44^+CD62L^+$) cells were collected on day 28. The expression of IDH1 mRNA was not detectable, and IDH3 expression remained unaltered (Extended Data Fig. 1p), whereas the expression of IDH2 was significantly higher in SLECs than in MPECs, T_{EM} or T_{CM} cells (Extended Data Fig. 1q). We then generated 'IDH2-deficient' T cells by CRISPR–Cas9 deletion in P14 cells (Extended Data Fig. 1r). The significant reduction in m + 1 metabolites after [1-^{13}C]-glutamine labelling—the heavy carbon of which can only be incorporated into downstream metabolites through RC—confirmed the role of IDH2 in mediating RC in $CD8^+$ T cells (Fig. 1e and Extended Data Fig. 1s–v).

HIF-1α orchestrates metabolic adaptations after engagement of the T cell receptor (TCR)[17], and could thus drive the expression of IDH2 and RC in $CD8^+$ T cells. Indeed, inhibition of HIF-1α with echinomycin after T cell activation reduced the expression of IDH2 mRNA and protein (Extended Data Fig. 2a–c), as well as that of its known targets GLUT1 and PDK1 (Extended Data Fig. 2d,e; see ref. 18), whereas stabilization of HIF-1α by dimethyloxalylglycine (DMOG) further boosted the expression of IDH2 in T_E cells, and also in metabolically less active T_M cells (Extended Data Fig. 2f–h). In addition, computational analyses uncovered a binding site for the HIF-1α transcription factor on the promoter of mouse and human *IDH2* (Extended Data Fig. 2i). However, IDH2 is a bidirectional enzyme, and it was previously shown that reductive IDH2 activity is a function of the α-ketoglutarate (α-KG) and citrate ratio[19]. In line with this, we observed a markedly higher α-KG/citrate ratio in T_E than in T_M cells (Extended Data Fig. 2j). Next, we asked how the α-KG/citrate ratio is altered in T_E cells. High HIF activity, as well as promoting IDH2 expression, induces PDK1 expression (Extended Data Fig. 2e), which, by suppressing pyruvate dehydrogenase[20], limits the entry of carbon into the TCA cycle, thus explaining the decreased citrate levels that promote RC[21]. Indeed, using sodium dichloroacetate (DCA) to inhibit PDK1 in T_E cells decreased the α-KG/citrate ratio (Extended Data Fig. 2k), and consequently inhibited RC (Extended Data Fig. 2l–n). Altogether, our data suggest that IDH2-mediated RC is specifically used by T_E cells and is orchestrated through transcriptional and metabolic remodelling by HIF-1α.

Knockout of *IDH2* promotes T_M differentiation

To determine the role of IDH2-driven metabolism in T cell function and differentiation, we transferred *Idh2*-gRNA-transduced P14 cells into whole-body Cas9 mice that were infected with lymphocytic choriomeningitis virus (LCMV)-Armstrong concurrently with the activation of the P14 cells (Fig. 1f). Despite the essential role of RC in sustaining cancer-cell proliferation, deletion of *IDH2* did not alter the kinetics of the $CD8^+$ T cell response (Fig. 1g). However, the differentiation of IDH2-deficient $CD8^+$ T cells was skewed towards a memory phenotype, with a significantly higher proportion of circulating T_{CM} cells, and with the expression of TCF1 and IL-2 (Fig. 1h and Extended Data Fig. 2o–q). To functionally test the increased differentiation of T_M cells, we transferred equal amounts of either $Thy1.1^+$ control or IDH2-deficient $CD8^+$ T cells into naive *Rag1*-knockout (KO) hosts, followed by infection with LCMV-Armstrong (Fig. 1f). IDH2-deficient T cells showed a greater re-expansion capacity after secondary challenge (Fig. 1i), and maintained higher expression of TCF1 and CD62L seven days after secondary challenge (Extended Data Fig. 2r,s). Furthermore, deletion of *IDH2* increased the production of IL-2, IFNγ and TNF (Fig. 1j,k), which correlated with enhanced viral clearance in the kidneys and liver (Fig. 1l,m). We validated these observations in the LM-OVA bacterial-infection model (Extended Data Fig. 3a–m). Altogether, these data reveal that RC is dispensable for clonal expansion and antiviral effector functions, and that genetic deletion of *IDH2* instead promotes the differentiation of T_M cells.

Inhibition of IDH2 improves CAR T cell function

Successful ACT immunotherapy against cancer depends on the memory-like status of the adoptively transferred cells[6]. Because genetic deletion of *IDH2* favoured the differentiation of T_M cells, we evaluated whether the simple and straightforward integration of a small-molecule IDH2 inhibitor during the ex vivo manufacturing of T cells for ACT would be sufficient to enrich T_M cells, and thus could be a valuable strategy to improve therapeutic efficacy. We tested two structurally different small-molecule inhibitors of IDH2 (AGI-6780 and the US Food and Drug Administration (FDA)-approved AG-221 (enasidenib; referred to as IDH2i in this manuscript)), both of which were designed to inhibit mutant IDH2, but were also found to inhibit wild-type IDH2 (half-maximum inhibitory concentration (IC_{50}) values of around 2 μM (AGI-6780) and 1.8 μM (AG-221)) (Extended Data Fig. 4a). Activating and culturing T cells with either IDH2 inhibitor suppressed RC (Extended Data Fig. 4b,c) and induced the expression of the memory markers CD62L and TCF1, but did not affect activation markers or cell proliferation (Extended Data Fig. 4d–j). Notably, selective inhibition of IDH1 with AG-120 did not affect the expression of CD62L (Extended Data Fig. 4k,l), and IDH2i did not further boost the differentiation of T_M cells in activated splenic T cells from whole-body *Idh2*-KO mice (Extended Data Fig. 4m), showing that the induction of T_M cells by IDH2i is IDH2 specific. In addition, IDH2i-conditioned OVA-specific T cell differentiation was skewed from SLECs to MPECs and T_{CM} cells producing more cytokines, when transferred into mice followed by LM-OVA infection (Extended Data Fig. 4n–s), suggesting that short-term in vitro interference of IDH2 is sufficient to maintain a memory phenotype after in vivo transfer.

We then transduced mouse $CD8^+$ T cells with a CAR construct targeting the human oncogene HER2 (encoded by *ERBB2*) (Extended Data Fig. 5a), or with a control blue fluorescent protein (BFP), followed by ACT into mice bearing HER2-overexpressing B16 tumours (Extended Data Fig. 5b,c). Whereas transfer of a sub-therapeutic number of dimethyl sulfoxide (DMSO)-conditioned HER2-CAR T cells did not confer antitumour effects, as compared with the transfer of untreated or BFP-transduced T cells, infusion of IDH2i-conditioned HER2-CAR T cells provided substantial control of tumour growth (Fig. 2a and Extended Data Fig. 5d,e). The tumour-draining lymph nodes of IDH2i-CAR-treated mice contained more HER2-CAR T cells, with increased expression of TCF1 and CD62L (Fig. 2b–d), thus probably constituting a pool of potent T_M cells that are able to continuously generate antitumour T_E cells, as evidenced by the increased number of HER2-CAR T cells in the tumour (Fig. 2e). IDH2i also caused a shift towards a more progenitor exhausted and less terminally exhausted T cell phenotype (Fig. 2f,g), with increased total numbers of both TIL populations (Extended Data Fig. 5f,g). IDH2i-conditioned HER2-CAR TILs expressed higher levels of TCF1 and lower levels of the exhaustion markers PD-1, TIM3 and LAG3, and produced more cytokines and cytotoxic granules (Fig. 2h and Extended Data Fig. 5h–m). Of note, we observed a similar enhanced antitumour efficacy after ACT of IDH2i-conditioned transgenic OVA-specific $CD8^+$ T cells into Yumm1.7-OVA and B16-OVA tumour-bearing mice (Extended Data Fig. 5n–y and Extended Data Fig. 6a–m), including therapeutic synergy with anti-PD-1 treatment (Extended Data Fig. 6n–p), and by using AGI-6780 for in vitro conditioning of T cells before ACT into B16-OVA tumour-bearing mice (Extended Data Fig. 5z).

We next activated and expanded peripheral blood T cells from healthy human donors with IDH2i, which, as in mouse T cells, enhanced CD62L expression, and increased the population of stem cell memory T (T_{SCM})-like cells (defined as $CD45RA^+CD62L^+CD45RO^-CCR7^+CD95^+CD28^+CD27^+$) (Extended Data Fig. 7a–c). We then generated human brexu-cel-like CD19-28ζ CAR T cells in the presence of IDH2i or DMSO (Extended Data Fig. 7d). IDH2i conditioning did not affect transduction efficiency but strongly increased the expression of CD62L

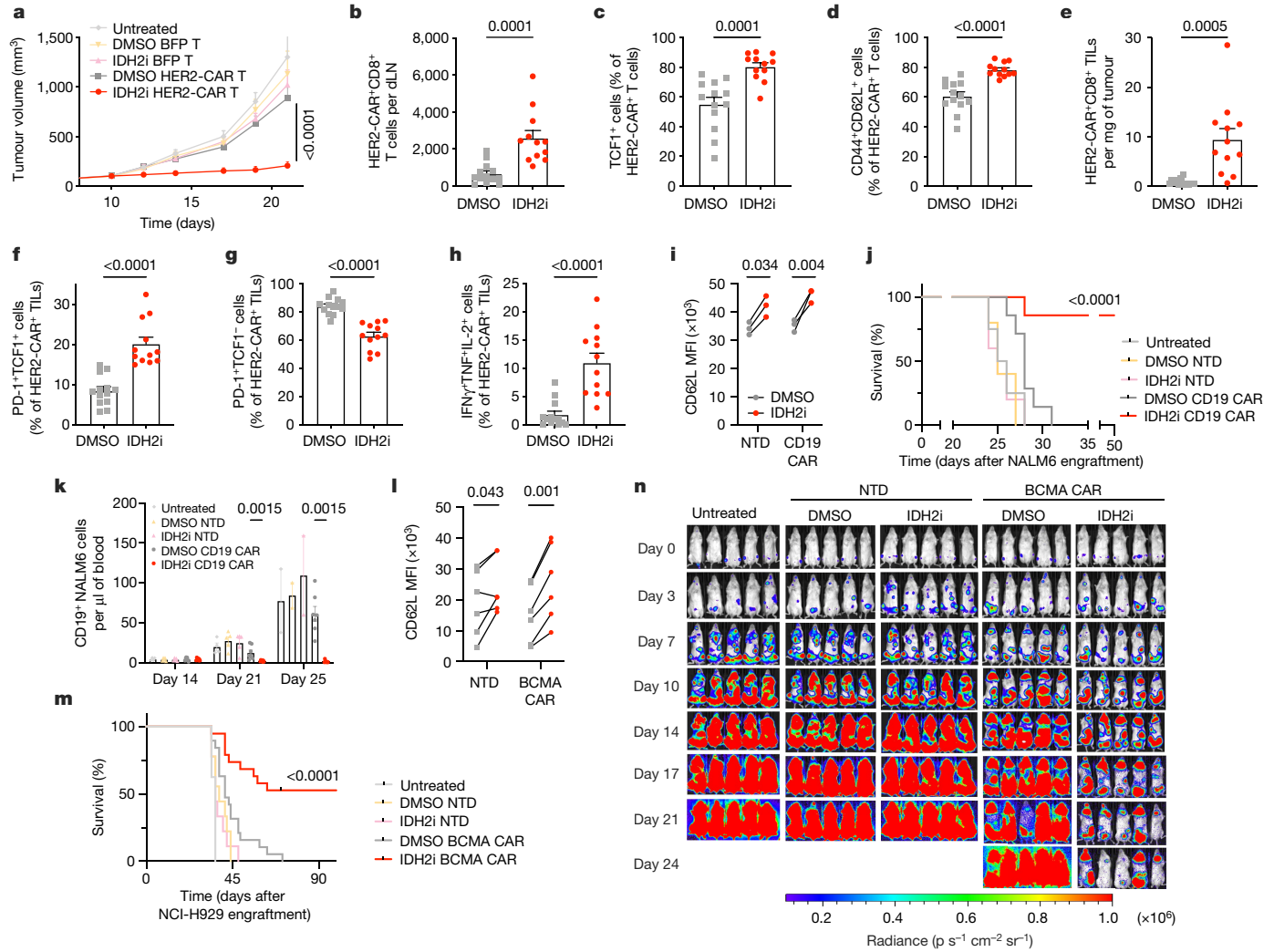

Fig. 2 | Inhibition of IDH2 improves the function of CAR T cells. a, Tumour growth of B16-HER2 tumour-bearing mice treated with DMSO-conditioned or IDH2i-conditioned BFP-transduced T cells or HER2-CAR T cells. **b**–**d**, Number of HER2-CAR$^+$ T cells (**b**) and their percentage of TCF1$^+$ (**c**) and CD44$^+$CD62L$^+$ cells (**d**) in tumour-draining lymph nodes (dLNs) at dissection. **e**, Number of HER2-CAR$^+$ TILs per milligram of tumour at dissection. **f**,**g**, Percentages of PD-1$^+$TCF1$^+$ cells (**f**) and PD-1$^+$TCF1$^-$ cells (**g**) among HER2-CAR$^+$ TILs. **h**, Percentage of IFNγ$^+$TNF$^+$IL-2$^+$ HER2-CAR$^+$ TILs. In **a**–**h**: $n = 12$ (IDH2i) and $n = 13$ (DMSO) biological replicates; pooled data from two independent experiments. **i**, Mean fluorescence intensity (MFI) of CD62L out of CD62L$^+$ CD19-CAR$^+$ CD8$^+$ T cells nine days after activation, in mice infused with non-transduced (NTD) or anti-CD19 CAR T cells ($n = 3$ biological replicates; pooled data from two independent experiments). **j**, Survival curve of NALM6 tumour-bearing mice infused with NTD or anti-CD19 CAR T cells. **k**, Number of CD19$^+$ NALM6 cells per microlitre of blood at days 14, 21 and 25 after tumour engraftment. In **j**,**k**: $n = 7$ (DMSO or IDH2i CAR), $n = 5$ (DMSO or IDH2i NTD) and $n = 4$ (untreated) mice; pooled data from two independent experiments using three human donors. **l**, MFI of CD62L out of CD62L$^+$ BCMA-CAR$^+$ CD8$^+$ T cells nine days after activation, in mice infused with NTD or BCMA CAR T cells ($n = 6$ biological replicates; pooled data from two independent experiments). **m**, Survival curve of NCI-H929 tumour-bearing mice treated by ACT. **n**, Representative bioluminescence images of NCI-H929 tumour burden. In **m**,**n**: $n = 19$ (DMSO or IDH2i CAR), $n = 9$ (DMSO or IDH2i NTD) and $n = 8$ (untreated) mice; pooled data from two independent experiments using two human donors. Data are mean ± s.e.m. and were analysed by unpaired (**a**–**h**) or paired (**i**,**l**) two-tailed Student's *t*-test, log-rank test (**j**,**m**) or two-way ANOVA using the original false discovery rate (FDR) test of Benjamini and Hochberg (**k**).

in both untransduced and CAR T cells (Fig. 2i). Notably, transfer of IDH2i-conditioned CAR T cells into NOD-scid-γc$^{-/-}$ (NSG) mice bearing NALM6 B-cell acute lymphoblastic leukaemia (B-ALL) cured almost all mice—in contrast with the transfer of DMSO-treated CAR T cells, which had only a marginal therapeutic effect (Fig. 2j,k).

Finally, we assessed the effect of IDH2 inhibition in two potential ACT applications for multiple myeloma. Autologous bone marrow-infiltrating lymphocytes (MILs) have been proposed as candidates for ACT after autologous transplantation of haematopoietic stem cells in high-risk patients with multiple myeloma[22]. We thus used IDH2i to activate and expand MILs that were isolated from patients with multiple myeloma, which enhanced the expression of CD62L and resulted in a T_{SCM}-like phenotype (Extended Data Fig. 7e–g). Next, we generated ide-cel-like B cell maturation antigen (BCMA) CAR T cells using an 11D5-3-BBζ CAR (Extended Data Fig. 7h). IDH2i conditioning again led to significant induction of CD62L in CD8$^+$ CAR T cells (Fig. 2l). Most compellingly, infusion of IDH2i-conditioned BCMA CAR T cells into an NCI-H929 myeloma xenograft mouse model markedly improved antitumour activity and survival (Fig. 2m,n and Extended Data Fig. 7i). IDH2 inhibition did not affect the expansion of peripheral blood mononuclear cells (PBMCs), CAR T cells or MILs (Extended Data Fig. 7j–l). Collectively, these data show that transient in vitro conditioning with an IDH2 inhibitor is sufficient to induce the formation of memory-like CD8$^+$ T cells with enhanced antitumour capacities in different mouse models of melanoma tumours and in human xenograft models of FDA-approved CAR T cell therapies for B-ALL and multiple myeloma.

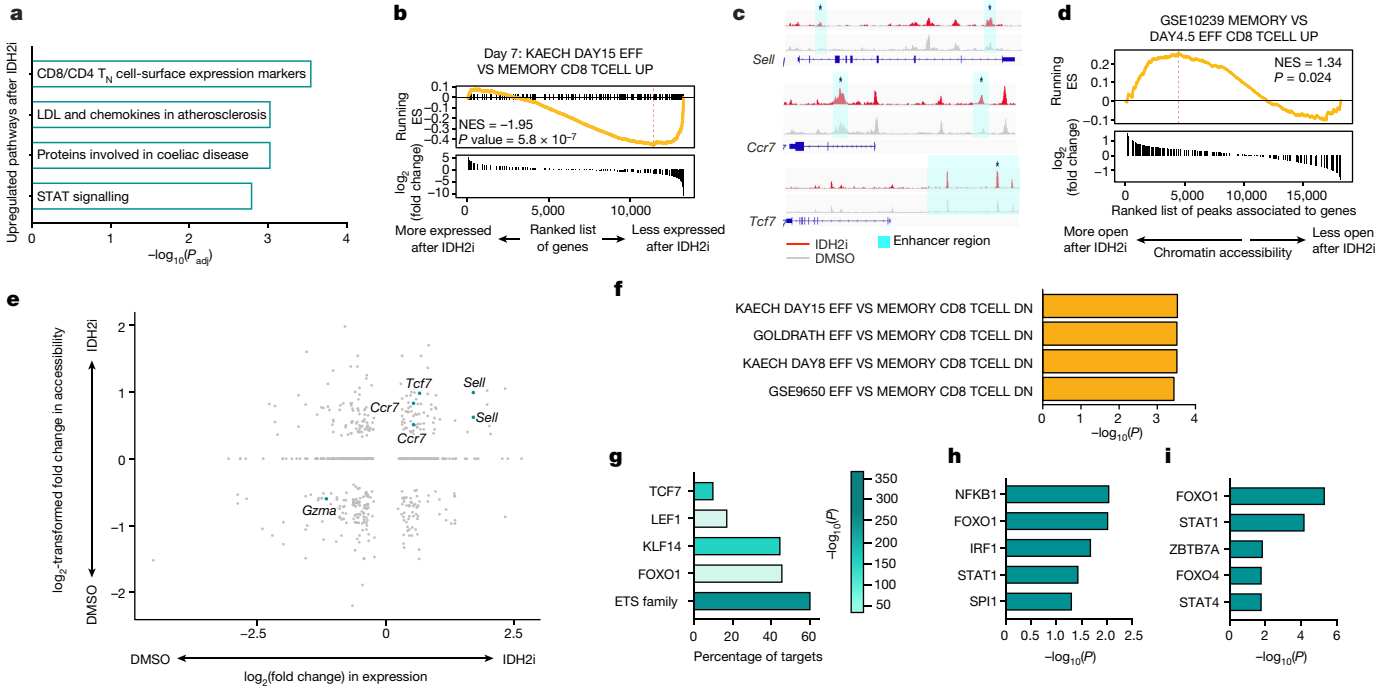

Fig. 3 | IDH2 inhibition leaves an epigenetic imprint. a, OVA-specific CD8$^+$ T cells were activated and cultured for seven days with IDH2i or DMSO, followed by RNA-seq analysis. Shown are pathways significantly enriched among upregulated genes after IDH2 inhibition, identified by Enrichr[23] in the Elsevier Pathway Collection (https://www.elsevier.com/solutions/pathway-studio-biological-research) ($n = 3$ biological replicates). LDL, low-density lipoprotein. **b**, GSEA of a memory-versus-effector signature from genes upregulated in IDH2i- compared to DMSO-conditioned T cells. NES, normalized enrichment score; running ES, running enrichment score. **c**, Representative ATAC-seq tracks in OVA-specific CD8$^+$ T cells activated and cultured for seven days with IDH2i or DMSO ($n = 3$ biological replicates). **d**, GSEA of a memory-versus-effector signature on more accessible chromatin regions after IDH2 inhibition. **e**, Differentially accessible chromatin regions in DMSO- versus IDH2i-conditioned cells (FDR $P < 0.05$), which were correlated with gene-expression data ($\log_2$-transformed fold change > 1 and $P_{adj} < 0.05$). **f**, Over-representation analysis of the indicated gene signatures from genes exhibiting higher chromatin accessibility and transcription after IDH2 inhibition. **g**, Top transcription factors identified in more open chromatin regions of IDH2i-conditioned cells using HOMER. **h**, Top five most significant mouse transcription factors identified by Enrichr in the TRRUST 2019 database (https://www.grnpedia.org/trrust/) in upregulated genes after IDH2 inhibition. Histograms depict negative log of P values ($-\log_{10} > 1.5$ and $P < 0.05$). **i**, Significantly enriched transcription factors in more accessible chromatin regions that correlated with increased gene expression after IDH2 blockade. Transcription factors were found in the TRRUST 2019 database (https://www.grnpedia.org/trrust/) using Enrichr software. Histograms depict negative log of P values ($-\log_{10} > 1.5$ and $P < 0.05$).

IDH2i shapes chromatin for a memory phenotype

To investigate changes induced by IDH2i in the gene transcriptional landscape, we performed bulk RNA-seq. A total of 476 genes were significantly differentially expressed after inhibition of IDH2. Gene set analysis using Enrichr[23] showed that IDH2i upregulated pathways associated with T_N cell-surface expression markers and STAT signalling (Fig. 3a). More specifically, gene set enrichment analysis (GSEA) on gene sets from effector versus memory CD8$^+$ T cells confirmed the enrichment of a memory CD8$^+$ T cell gene signature after inhibition of IDH2 (Fig. 3b).

The expression of genes that drive the differentiation and function of memory CD8$^+$ T cells is dictated by a permissive chromatin state[10]. We therefore performed an assay for transposase-accessible chromatin with sequencing (ATAC-seq) to compare the epigenetic landscape of IDH2i- versus DMSO-conditioned CD8$^+$ T cells. In general, we observed a total of 8,000 differentially open regions, with a ratio of approximately 50/50%, suggesting that global chromatin accessibility is similar between the two groups (Extended Data Fig. 7m). However, regions that were more accessible after IDH2 inhibition were located at memory genes such as *Sell*, *Tcf7* and *Ccr7*, thus correlating with increased gene transcription (Fig. 3c and Extended Data Fig. 7n) and enrichment of a memory CD8$^+$ T cell gene signature identified by GSEA (Fig. 3d). Integration of both ATAC-seq and RNA-seq data confirmed that, among several other genes, *Sell*, *Tcf7* and *Ccr7* were more accessible in their transcription start site or enhancer regions and were upregulated at the transcriptional level (Fig. 3e). Accordingly, GSEA for this set of genes with increased chromatin accessibility and transcription showed an enrichment for memory CD8$^+$ T cell signatures after IDH2 inhibition (Fig. 3f). Finally, the most enriched transcription factor motifs in more accessible genomic loci after IDH2 inhibition were important transcription factors for memory CD8$^+$ T cell identity and function, such as FOXO1, LEF1 and TCF1 (Fig. 3g). Binding motifs for FOXO1 and STAT1 were also some of the most upregulated genes after IDH2 inhibition (Fig. 3h), and were consistently enriched in those upregulated genes that exhibited more accessible chromatin after integration of ATAC-seq and RNA-seq data (Fig. 3i). Altogether, these results show that increased transcription of memory genes after the inhibition of IDH2 in activated T cells is strongly correlated with profound alterations in chromatin accessibility.

IDH2i induces metabolic compensation

T cell metabolism is tightly linked with phenotypic differentiation. To elucidate the mechanism by which IDH2 interference induces the differentiation of T_M cells, we examined the potential functions of IDH2. Reductive IDH1 and oxidative IDH2 can coordinate to generate mitochondrial NADPH to buffer mitochondrial reactive oxygen species (ROS)[15], an key signalling molecule for the activation of T cells[3]. However, basal mitochondrial ROS levels were unchanged, and when exposing the cells to increasing doses of H_2O_2, oxidative stress was

buffered equally in DMSO- versus IDH2i-treated cells (Extended Data Fig. 8a). We then investigated whether there could be a link between the suppression of RC after IDH2 inhibition and the differentiation of T_M cells. We made use of T cells that lack mitochondrial transcription factor A (TFAM), which have mitochondrial defects and, in analogy to keratinocytes, might have high rates of RC[24]. We activated TFAM KO splenocytes and observed an overt lower viability compared to wild-type T cells, which was further reduced by treatment with IDH2i (Extended Data Fig. 8b). Notably, in the viable TFAM KO cells, IDH2 inhibition was able to boost the expression of CD62L expression to the same level as that in wild-type cells. Furthermore, DMSO-treated TFAM KO T cells showed lower expression of CD62L than did DMSO-treated wild-type T cells (Extended Data Fig. 8c). These data suggest that RC, which is likely to be an important metabolic activity in TFAM KO T cells, locks T cells in an effector differentiation state. Nevertheless, the observed differentiation of T_M cells could still be an artefact of general disruption of the TCA cycle, because both IDH2 and TFAM are key regulators of mitochondrial metabolism and homeostasis. However, genetic disruption of other major TCA-cycle enzymes, such as α-KG dehydrogenase (OGDH) and succinate dehydrogenase (SDHB), could not recapitulate the induction of T_M cell differentiation that was observed after deletion of *IDH2* (Extended Data Fig. 8d,e), indicating that IDH2i-orchestrated T_M cell differentiation does not result from general disruption of the TCA cycle.

We then investigated how inhibition of IDH2 affects mitochondrial metabolism. Metabolomics analyses revealed overall alterations in the levels of TCA-cycle intermediates after IDH2 inhibition, including higher levels of succinate, fumarate, malate and 2-HG, but equal levels of citrate, acetyl-CoA and α-KG (Fig. 4a,b). The maintenance of cellular citrate and acetyl-CoA pools after the inhibition of RC is notable, and suggests that compensatory metabolic fluxes are activated. We therefore performed an extensive analysis of how inhibition of IDH2 affects the metabolism of three major mitochondrial fuels previously characterized in T cells: glucose, glutamine and fatty acids. [U-^{13}C]-glutamine labelling confirmed a major drop in RC-derived citrate and acetyl-CoA, from 20% and 30%, respectively, to almost 0% after IDH2 inhibition, whereas oxidative m + 4 labelling in metabolites was maintained (Fig. 4c and Extended Data Fig. 8f–i). We then measured [U-^{13}C]-glucose and [U-^{13}C]-palmitate labelling into citrate and acetyl-CoA, and detected a significant increase in the incorporation of palmitate, but not glucose, after IDH2 inhibition, suggesting that fatty acid oxidation (FAO) provides a major compensatory flow to maintain the levels of acetyl-CoA (Fig. 4c and Extended Data Fig. 8j–l). After inhibition of IDH2, T cells indeed become much more oxidative, as measured by Seahorse assay (Fig. 4d and Extended Data Fig. 8m–o). Treatment with etomoxir (an inhibitor of carnitine palmitoyltransferase 1A (CPT1A)) led to a stronger reduction in both maximal respiration and the basal oxygen consumption rate (OCR) in IDH2i-treated T cells (Fig. 4d,e). To support increased fatty acid oxidation and maintain citrate levels after inhibition of RC, an anaplerotic substrate needs to be provided. In rapidly proliferating T cells and cancer cells, glutamine is a major anaplerotic carbon source, driving oxidative phosphorylation[1,25,26]. Glutamine consumption was increased (Fig. 4f), and the basal OCR was more affected by glutaminase inhibition with BPTES, in IDH2i-treated T_E cells (Fig. 4e), suggesting increased glutamine oxidation. In IDH2i-treated cells, either interfering with the oxidative metabolism of glutamine downstream of α-KG through α-KGDH deletion, or inhibiting FAO with etomoxir, significantly suppressed the enhanced differentiation of T_M cells (Extended Data Fig. 8p,q). Of note, inhibition of mitochondrial pyruvate oxidation by UK5099 did not differentially reduce the basal OCR, and glucose consumption remained unaltered as well (Fig. 4e and Extended Data Fig. 8r), suggesting no compensatory increase in glucose metabolism after IDH2 inhibition. However, we cannot exclude the possibility that other substrates contribute to anaplerosis and compensation after the inhibition of RC. Branched-chain amino acids can also provide TCA-cycle intermediates as either acetyl-CoA or succinyl-CoA (ref. 27). Indeed, we found that the levels of many amino acids, as well as the expression of the branched-chain amino-acid transporter CD98, were significantly increased in IDH2i-treated T cells (Extended Data Fig. 8s–u). In conclusion, fatty acid and glutamine oxidation compensate for the loss of RC after inhibition of IDH2 and are required for the enhanced differentiation of T_M cells. The accompanying higher oxygen consumption rate, which has been shown to correlate with larger pools of TCA metabolites in T cells[28] as well as in cancer cells[29], could explain the increase in metabolite abundance.

TCA metabolites dictate epigenetic memory

The epigenetic induction of T_M cell differentiation after inhibition of IDH2 suggests changes in the post-translational modifications of histones. We observed that both permissive- and repressive-specific histone modifications were altered after IDH2 inhibition (Extended Data Fig. 9a–c). Among the altered permissive histone marks, the trimethylation of lysine residue 4 on histone H3 (H3K4me3) was previously shown to be involved in the regulation of T_M cell differentiation[10] (Fig. 4g). By mining previously published H3K4me3 chromatin immunoprecipitation followed by sequencing (ChIP–seq) data, we found that key pro-memory genes with enhanced chromatin accessibility after IDH2 inhibition were associated with H3K4me3 in T_N cells, and that this association was maintained in T_{CM} cells, but lost in T_E cells[30,31] (Extended Data Fig. 9d,e). Of note, higher levels of H3K4me3 were also conserved in human MILs from five patients with multiple myeloma, after culturing the MILs with IDH2i (Extended Data Fig. 9f).

The TCA-derived metabolites succinate, fumarate, 2-HG and malate can compete with the cofactor α-KG for binding to certain histone demethylases, and can inhibit the function of these enzymes[32,33]. To restore the metabolite balance, we supplemented IDH2i-conditioned T cells with a cell-permeable α-KG analogue, dimethyl oxoglutarate, at concentrations that maintained the intracellular levels of α-KG within physiological range (Extended Data Fig. 9g). Increasing intracellular α-KG reverted the IDH2i-mediated increase in H3K4me3, and this was accompanied by a concomitant decrease in CD62L expression (Fig. 4h,i and Extended Data Fig. 9h), suggesting that an imbalance of metabolites after IDH2 inhibition epigenetically drives the expression of T_M cell genes. Indeed, an altered metabolite balance alone is sufficient to drive the differentiation of T_M cells, as supplementation of $CD8^+$ T cells with cell-permeable fumarate (100 μM) or *S*-2-HG (250 μM)—but not succinate (0.5, 1 or 2 mM)—increased the levels of trimethylation at H3K4 and the expression of CD62L, which could be reverted by resupplying cells with the α-KG analogue (Fig. 4j,k and Extended Data Fig. 9i–k). Methylation on the suppressive mark H3K27 was not affected (Fig. 4j), which suggests that metabolite imbalance does not lead to a random global increase in histone methylation.

The KDM5 family of histone demethylases are α-KG-dependent and specific for H3K4 (ref. 34). As both the Michaelis constant (K_m) value of α-KG and the IC_{50} values of inhibitory TCA metabolites towards KDM5B activity have been reported before[33], we estimated the intracellular concentration of these metabolites, on the basis of the absolute quantifications in Fig. 4a, to calculate a ratio that could indicate the propensity of T cells to exhibit KDM5 inhibition. This ratio was strongly and significantly shifted towards inhibition after IDH2 inhibition (Extended Data Fig. 10a). Indeed, the activity of KDM5 was significantly reduced in IDH2i-treated T cells, which could be restored by increasing intracellular α-KG (Fig. 4l). Furthermore, KDM5 inhibition increased the levels of H3K4me3 and the expression of CD62L in DMSO-conditioned cells (Fig. 4m,n and Extended Data Fig. 10b). Notably, in IDH2-inhibited T cells, inhibition of KDM5 did not further increase the levels of H3K4me3 and CD62L, but it abrogated the suppression of H3K4me3 and CD62L after concomitant supplementation with the α-KG analogue (Fig. 4m,n and Extended Data Fig. 10b), suggesting that the metabolite imbalance induced by

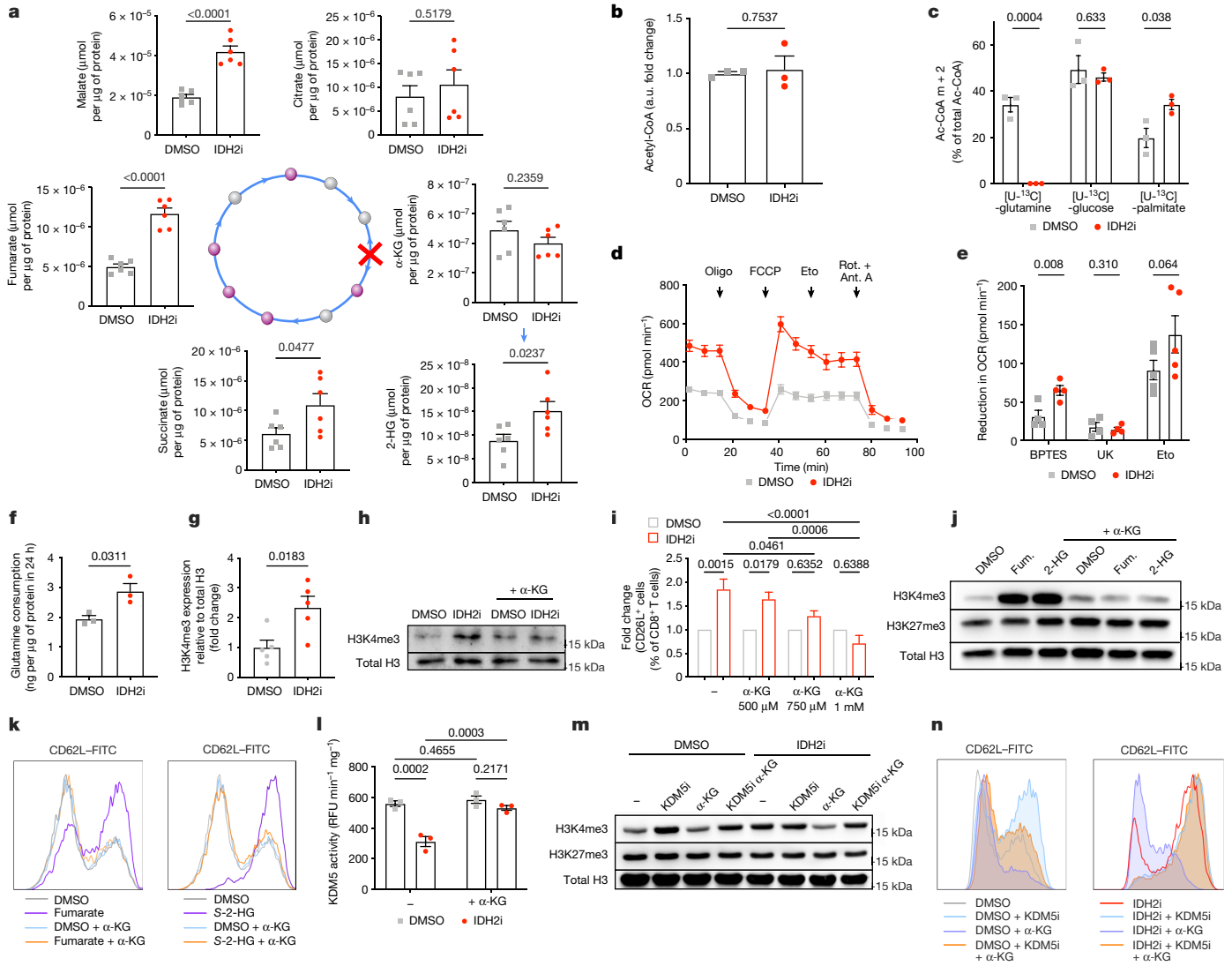

Fig. 4 | IDH2 inhibition alters the balance of metabolites, which dictates epigenetic memory. a, Quantification of metabolites in T_E cells. The TCA cycle is depicted in blue, with purple circles representing quantified metabolites and grey circles representing metabolites that were not quantified. IDH2 inhibition is represented by a red cross. ($n = 6$ biological replicates; pooled data from two independent experiments). **b**, Acetyl-CoA abundance ($n = 3$ biological replicates). a.u., arbitrary units. **c**, Percentages of acetyl-CoA m + 2 labelled by [U-^{13}C]-glutamine, [U-^{13}C]-glucose or [U-^{13}C]-palmitate ($n = 3$ biological replicates). **d**, OCR by Seahorse ($n = 4$ biological replicates; pooled data from two independent experiments). **e**, Reduction in basal OCR after addition of BPTES, UK5099 or etomoxir ($n = 4$ (UK and BPTES) and $n = 5$ (Eto) biological replicates; pooled data from two independent experiments). **f**, Glutamine consumption in T_E cells ($n = 3$ biological replicates). **g**, Immunoblot quantification of H3K4me3 ($n = 5$ biological replicates; pooled data from five independent experiments). **h**, Immunoblot of H3K4me3 in T cells supplemented or not with dimethyl 2-oxoglutarate (an analogue of α-KG). Representative of four independent experiments with four biological replicates. **i**, CD62L expression in T cells supplemented with α-KG ($n = 3$ biological replicates; pooled data from three independent experiments). **j**, Immunoblot of histone marks after supplementation with cell-permeable metabolites. Representative blot from three independent experiments with three biological replicates. **k**, CD62L expression in T cells with the indicated treatments. Representative histograms from three independent experiments with three biological replicates. **l**, KDM5 activity after treatment with DMSO or IDH2i, with α-KG supplementation. RFU, relative fluorescence units ($n = 3$ biological replicates). **m**,**n**, Immunoblot of histone marks (**m**) and CD62L expression (**n**). KDM5i, KDM5 inhibitor. Representative of two (**m**) or three (**n**) independent experiments with two (**m**) or 3 (**n**) biological replicates). Data are mean ± s.e.m. and were analysed by unpaired two-tailed Student's *t*-test (**b**,**c**,**e**–**g**), multiple unpaired two-tailed *t*-tests using the Benjamini and Hochberg method (**a**), one-way ANOVA using Tukey's multiple comparison test (**i**) or two-way ANOVA using the original FDR test of Benjamini and Hochberg (**l**). For gel source data, see Supplementary Fig. 1.

IDH2 inhibition favours the differentiation of T_M cells by inhibiting the KDM5-dependent demethylation of H3K4.

H3K4me3 was shown to promote histone acetylation by recruiting histone acetyltransferases (HATs)[35], and in line with this, we observed strong increases in the acetylation of histone lysine residues (Extended Data Fig. 9a–c), which has been shown to drive pluripotency in T_M cells[9]. Because FAO is involved in the enhanced differentiation of T_M cells after IDH2 inhibition, and is compensating for the loss of RC-derived acetyl-CoA, we wondered to what extent FAO contributes to the enhanced histone acetylation. Treatment with etomoxir partially reduced acetylation on H3K27 and H3K14 in IDH2i-treated cells, and this effect was reverted by acetate supplementation (Extended Data Fig. 10c,d). The inhibition of ATP citrate lyase (ACLY), which is essential to form cytosolic acetyl-CoA from mitochondrial-generated citrate to fuel histone acetylation[36], partially reverted histone acetylation on H3K27 and H3K14 and CD62L expression in IDH2i-treated T cells (Extended Data Fig. 10e,f). These results indicate that FAO- and citrate-derived acetyl-CoA have a partial role in supporting the

phenotype observed after IDH2 inhibition. Preventing histone acetylation by inhibition of the HAT p300 with the inhibitor C646 abrogated the increase in H3K27ac and CD62L expression after IDH2 inhibition (Extended Data Fig. 10g–i). Notably, the improved antitumour effect of IDH2i conditioning was lost when p300 was inhibited simultaneously, indicating that the increased histone acetylation essentially contributes to the induction of memory-like T cells with increased antitumour properties (Extended Data Fig. 10j). Together, these observations reveal the crucial role of RC in epigenetically locking T cells in a terminal effector differentiation state (Extended Data Fig. 10k).

It was previously suggested that, similarly to cancer cells[12], clonally expanding T cells rely on RC to sustain their proliferation; however, scientific evidence was lacking[37]. In this study, we show that IDH2-mediated RC is a unique metabolic characteristic of T_E cells, but that it is dispensable for proliferation and effector function. Inactivation of IDH2 epigenetically enabled T cells to express genes that are associated with a memory phenotype. The post-translational modification of histones is a key mechanism that determines gene expression and phenotypic differentiation in $CD8^+$ T cells. T_E cells lose the association of the permissive mark H3K4me3 on naive and memory genes after priming by influenza infection, as compared to T_N and T_M cells. This suggests that H3K4me3 determines the pluripotency potential of $CD8^+$ T cells. We have shown that H3K4 trimethylation is regulated by KDM5 in $CD8^+$ T cells. To allow the activity of KDM5, a specific ratio of metabolites is required, which is established when RC by IDH2 can take place. Therefore, we hypothesize that when naive $CD8^+$ T cells are activated, the induction of RC permits KDM5 activity—which is required for the demethylation of H3K4 at naive and memory genes—and thereby locks the T cells into a terminal effector differentiation program. Inhibition of IDH2-mediated RC alters the levels of metabolites and inhibits KDM5, thus maintaining high levels of H3K4me3 at naive and memory genes. This does not diminish effector function—as evidenced by potent antiviral activity—but instead maintains pluripotency, which favours the differentiation of T_M cells after antigen clearance.

Finally, we identify IDH2 inhibition as a promising solution to boost the differentiation of memory cells during the in vitro expansion of T cell products for ACT, which could result in markedly improved antitumour efficacy. Numerous genetic approaches have been reported to induce the formation of T_M cells or to enhance the persistence and efficacy of CAR T cells after ACT[38,39]. The method that we propose —the addition of a small-molecule IDH2 inhibitor to maintain pluripotency during the ex vivo manufacturing of CAR T cells—could complement these next-generation CAR T cell constructs.

Online content

Any methods, additional references, Nature Portfolio reporting summaries, source data, extended data, supplementary information, acknowledgements, peer review information; details of author contributions and competing interests; and statements of data and code availability are available at https://doi.org/10.1038/s41586-023-06546-y.

1. Wang, R. et al. The transcription factor Myc controls metabolic reprogramming upon T lymphocyte activation. *Immunity* **35**, 871–882 (2011).
2. Ma, E. H. et al. Metabolic profiling using stable isotope tracing reveals distinct patterns of glucose utilization by physiologically activated $CD8^+$ T cells. *Immunity* **51**, 856–870 (2019).
3. Sena, L. A. et al. Mitochondria are required for antigen-specific T cell activation through reactive oxygen species signaling. *Immunity* **38**, 225–236 (2013).
4. Joshi, N. S. et al. Inflammation directs memory precursor and short-lived effector $CD8^+$ T cell fates via the graded expression of T-bet transcription factor. *Immunity* **27**, 281–295 (2007).
5. Klebanoff, C. A. et al. Central memory self/tumor-reactive $CD8^+$ T cells confer superior antitumor immunity compared with effector memory T cells. *Proc. Natl Acad. Sci. USA* **102**, 9571–9576 (2005).
6. Chen, G. M. et al. Integrative bulk and single-cell profiling of premanufacture T-cell populations reveals factors mediating long-term persistence of CAR T-cell therapy. *Cancer Discov.* **11**, 2186–2199 (2021).
7. Schluns, K. S. et al. Cutting edge: requirement for IL-15 in the generation of primary and memory antigen-specific CD8 T cells. *J. Immunol.* **168**, 4827–4831 (2002).
8. Dominguez, C. X. et al. The transcription factors ZEB2 and T-bet cooperate to program cytotoxic T cell terminal differentiation in response to LCMV viral infection. *J. Exp. Med.* **212**, 2041–2056 (2015).
9. Gray, S. M. et al. Polycomb repressive complex 2-mediated chromatin repression guides effector $CD8^+$ T cell terminal differentiation and loss of multipotency. *Immunity* **46**, 596–608 (2017).
10. Araki, Y. et al. Genome-wide analysis of histone methylation reveals chromatin state-based regulation of gene transcription and function of memory $CD8^+$ T cells. *Immunity* **30**, 912–925 (2009).
11. Pietrocola, F. et al. Acetyl coenzyme A: a central metabolite and second messenger. *Cell Metab.* **21**, 805–821 (2015).
12. Mullen, A. R. et al. Reductive carboxylation supports growth in tumour cells with defective mitochondria. *Nature* **481**, 385–388 (2012).
13. Metallo, C. M. et al. Reductive glutamine metabolism by IDH1 mediates lipogenesis under hypoxia. *Nature* **481**, 380–384 (2012).
14. Reitman, Z. J. & Yan, H. Isocitrate dehydrogenase 1 and 2 mutations in cancer: alterations at a crossroads of cellular metabolism. *J. Natl Cancer Inst.* **102**, 932–941 (2010).
15. Jiang, L. et al. Reductive carboxylation supports redox homeostasis during anchorage-independent growth. *Nature* **532**, 255–258 (2016).
16. Akondy, R. S. et al. Origin and differentiation of human memory CD8 T cells after vaccination. *Nature* **552**, 362–367 (2017).
17. Pollizzi, K. N. & Powell, J. D. Integrating canonical and metabolic signalling programmes in the regulation of T cell responses. *Nat. Rev. Immunol.* **14**, 435–446 (2014).
18. Finlay, D. K. et al. PDK1 regulation of mTOR and hypoxia-inducible factor 1 integrate metabolism and migration of $CD8^+$ T cells. *J. Exp. Med.* **209**, 2441–2453 (2012).
19. Fendt, S. M. et al. Reductive glutamine metabolism is a function of the a-ketoglutarate to citrate ratio in cells. *Nat. Commun.* **4**, 2236 (2013).
20. Menk, A. V. et al. Early TCR signaling induces rapid aerobic glycolysis enabling distinct acute T cell effector functions. *Cell Rep.* **22**, 1509–1521 (2018).
21. Rajagopalan, K. N. et al. Metabolic plasticity maintains proliferation in pyruvate dehydrogenase deficient cells. *Cancer Metab.* **3**, 7 (2015).
22. Noonan, K. A. et al. Adoptive transfer of activated marrow-infiltrating lymphocytes induces measurable antitumor immunity in the bone marrow in multiple myeloma. *Sci. Transl. Med.* **7**, 288ra278 (2015).
23. Kuleshov, M. V. et al. Enrichr: a comprehensive gene set enrichment analysis web server 2016 update. *Nucleic Acids Res.* **44**, W90–W97 (2016).
24. Hamanaka, R. B. et al. Mitochondrial reactive oxygen species promote epidermal differentiation and hair follicle development. *Sci. Signal.* **6**, ra8 (2013).
25. DeBerardinis, R. J. et al. Beyond aerobic glycolysis: transformed cells can engage in glutamine metabolism that exceeds the requirement for protein and nucleotide synthesis. *Proc. Natl Acad. Sci. USA* **104**, 19345–19350 (2007).
26. Fan, J. et al. Glutamine-driven oxidative phosphorylation is a major ATP source in transformed mammalian cells in both normoxia and hypoxia. *Mol. Syst. Biol.* **9**, 712 (2013).
27. Neinast, M. D. et al. Quantitative analysis of the whole-body metabolic fate of branched-chain amino acids. *Cell Metab.* **29**, 417–429 (2019).
28. Vardhana, S. A. et al. Impaired mitochondrial oxidative phosphorylation limits the self-renewal of T cells exposed to persistent antigen. *Nat. Immunol.* **21**, 1022–1033 (2020).
29. Griss, T. et al. Metformin antagonizes cancer cell proliferation by suppressing mitochondrial-dependent biosynthesis. *PLoS Biol.* **16**, e1002309 (2015).
30. Tyrakis, P. A. et al. S-2-hydroxyglutarate regulates $CD8^+$ T-lymphocyte fate. *Nature* **540**, 236–241 (2016).
31. Russ, B. E. et al. Distinct epigenetic signatures delineate transcriptional programs during virus-specific $CD8^+$ T cell differentiation. *Immunity* **41**, 853–865 (2014).
32. Xiao, M. et al. Inhibition of α-KG-dependent histone and DNA demethylases by fumarate and succinate that are accumulated in mutations of FH and SDH tumor suppressors. *Genes Dev.* **26**, 1326–1338 (2012).
33. Tarhonskaya, H. et al. Studies on the interaction of the histone demethylase KDM5B with tricarboxylic acid cycle intermediates. *J. Mol. Biol.* **429**, 2895–2906 (2017).
34. Klose, R. J., Kallin, E. M. & Zhang, Y. JmjC-domain-containing proteins and histone demethylation. *Nat. Rev. Genet.* **7**, 715–727 (2006).
35. Zhang, T., Cooper, S. & Brockdorff, N. The interplay of histone modifications—writers that read. *EMBO Rep.* **16**, 1467–1481 (2015).
36. Wellen, K. E. et al. ATP-citrate lyase links cellular metabolism to histone acetylation. *Science* **324**, 1076–1080 (2009).
37. Pearce, E. L., Poffenberger, M. C., Chang, C. H. & Jones, R. G. Fueling immunity: insights into metabolism and lymphocyte function. *Science* **342**, 1242454 (2013).
38. Ye, L. et al. A genome-scale gain-of-function CRISPR screen in CD8 T cells identifies proline metabolism as a means to enhance CAR-T therapy. *Cell Metab.* **34**, 595–614 (2022).
39. Corria-Osorio, J. et al. Orthogonal cytokine engineering enables novel synthetic effector states escaping canonical exhaustion in tumor-rejecting $CD8^+$ T cells. *Nat. Immunol.* **24**, 869–883 (2023).

Methods

Mice and cell lines

C57BL/6 (B6) (CD45.2) mice were purchased from Charles River (France). *Cd4-Cre* (B6.Cg-Tg(Cd4-cre)1Cwi/BfluJ), whole-body Cas9 (B6J.129(Cg)-*Gt(ROSA)26Sor*$^{tm1.1(CAG\text{-}cas9^{*},\text{-}EGFP)}$*Fezh*/J) and conditional Cas9 or Rosa26-LSL-Cas9 knock-in (B6;129-*Gt(ROSA)26Sor*$^{tm1(CAG\text{-}cas9^{*},\text{-}EGFP)Fezh}$/J) mice were bought from the Jackson Laboratory and bred in-house. OT1 TCR transgenic mice, expressing a TCR specific for the chicken egg OVA SIINFEKL epitope in the context of $H2K^{b}$, and CRISPR–Cas9 knock-in OT1 TCR transgenic mice were obtained by crossing Rosa26-LSL-Cas9 knock-in mice with *Cd4-Cre* mice on an OT1 background. Female NOD-scid-$\gamma c^{-/-}$ (NSG) mice (6 to 8 weeks old) were purchased from the Jackson Laboratory and were bred and maintained at the animal facility of the University of Lausanne. Mice were kept in the SPF animal facility of the University of Lausanne. Males and females between 6 and 10 weeks old were used for experiments and were age and sex matched for ACT experiments. Sample size was chosen based on previous experience. Researchers were not blinded to the different treatment groups. Mice were kept in the SPF animal facility of the University of Lausanne in individually ventilated cages, at 19–23 °C with 45–65% humidity and a 12-h dark–light cycle. Experimentation was performed in respect of protocols approved by the veterinary authorities of the Canton de Vaud (VD2688.2, VD3763b, VD3390x1 and VD3309x1e).

Yumm1.7, B16-F10 melanoma cells, Phoenix-Eco and 293T cells were obtained from the American Type Culture Collection and were not further authenticated. Yumm1.7 and B16 cells were cultured in Dulbecco's modified Eagle's medium (DMEM), containing 10% fetal bovine serum (FBS), 1% penicillin–streptomycin (P/S; Gibco, 15070-063), and 1% L-glutamine (Q; Gibco, 25030-081). Phoenix-Eco cells were cultured in Iscove's modified Dulbecco's medium (IMDM), containing 10% FBS and 1% P/S. The 293T cells were maintained in DMEM (Gibco, 21885025) supplemented with 10% FBS. PCR testing was systematically done to confirm that cell lines were mycoplasma-free. NCI-H929 cells were purchased from the German Cell Culture Collection (DSMZ) and cultured in RPMI 1640 with 20% FBS, 1% sodium pyruvate (Gibco, 11360070) and 50 μM β2-mercaptoethanol (Gibco, 31350010). $CD4Cre^{+/wt}$*Tfam*$^{fl/fl}$ mouse splenocytes were gifted by the laboratory of M. Mittelbrunn and *IDH2* whole-body-knockout mouse splenocytes by the laboratory of S.-S. Im.

Culture of mouse T cells

Mouse spleens were processed on a 70-μm cell strainer, followed by centrifugation to obtain a single-cell suspension. Red blood cell lysis was done using Qiagen Red Blood Cell Lysis Buffer. Splenocytes were seeded at 10^{6} cells per ml in RPMI (Gibco, 61870-01) supplemented with 10% FBS (Gibco, 10270-106), 10 mM HEPES (Gibco, 15630-080), 1 mM sodium pyruvate (Gibco, 11360-039), 1% P/S (Gibco, 15070-063), 1× non-essential amino acids (Gibco, 11140-035), 1% L-glutamine (Gibco, 25030-081) and 50 μM β-mercaptoethanol. Recombinant human (rh) IL-2 100 IU ml^{-1} (in-house) and OVA peptide (SIINFEKL) 1 μg ml^{-1}, an IDH2 inhibitor (IDH2i: AG-221 (ref. 40), Cayman Chemical, 21277; AGI-6780 (ref. 41), Sigma-Aldrich, SML0895; AG-120, Cayman Chemical, 19894-5; all at 5 μM) or the control solvent DMSO (Sigma-Aldrich, 20-139) were also added to the cells.

For phenotypic analyses, immunoblotting and ACT, cells were washed at day 3 and cultured for another four days with rhIL-2 (100 IU ml^{-1}), hIL-7 (10 ng ml^{-1}, Peprotech 200-07), IDH2i or DMSO.

Culture of human T cells

Culture of PBMCs. Buffy coats from de-identified healthy human volunteer blood donors were obtained from the Center of Interregional Blood Transfusion SRK Bern.

PBMCs were isolated by density gradient centrifugation (Lymphoprep). Cells were seeded at 10^{6} cells per ml in round-bottomed 96-well plates in RPMI 1640 (Gibco, 61870-010) supplemented with 8% human AB serum (Blutspendedienst SRK Bern, 92041), kanamycin 1× (Gibco, 11360-039), 1% L-glutamine (Gibco, 25030-024), 1% sodium pyruvate (Gibco, 11360-039), 0.1% 2-mercaptoethanol (5×10^{-2} stock, Sigma-Aldrich, M-7522), 1% non-essential amino acids (Gibco, 11140-035), 150 IU ml^{-1} rhIL-2 (Peprotech, 200-02) and AG-221 or DMSO. PBMCs were activated with Dynabeads Human T-Activator CD3/CD28 (1:1 cell:bead ratio, Thermo Fisher Scientific, 11161D). Beads were removed five days after activation and cell phenotype was analysed by flow cytometry nine days after activation.

Culture of MILs. Bone marrow aspirates were obtained from patients with multiple myeloma at the Lausanne University Hospital under a research protocol approved by the cantonal ethical commission for human research (CER-VD), and after obtaining informed consent. Malignant plasma cells were separated from whole bone marrow by performing a CD138 positive selection with beads (EasySep, 17877). The positive fraction containing $CD138^{+}$ cells and the negative fraction containing MILs and other cells were frozen using 40% RPMI 1640 (Gibco, 61870-010), 50% FBS (Gibco, 10270-106; lot: 2166446) and 10% DMSO (Sigma-Aldrich, 41639) and stored in liquid nitrogen until use. The negative fraction was used in these experiments. Cells of the negative fraction were seeded at 10^{6} cells per ml in round-bottomed 96-well plates in RPMI 1640 (Gibco, 61870-010) supplemented with 8% AB serum, kanamycin 1× (Gibco, 11360-039), 1% L-glutamine (Gibco, 25030-024), 1% sodium pyruvate (Gibco, 11360-039), 0.1% 2-mercaptoethanol (5×10^{-2} stock, Sigma-Aldrich, M-7522), 1% non-essential amino acids (Gibco, 11140-035), 150 IU ml^{-1} rhIL-2 (Peprotech, 200-02) and AG-221 or DMSO, and were activated with Dynabeads Human T-Activator CD3/CD28 (1:1 cell:bead ratio, Thermo Fisher Scientific, 11161D). Beads were removed five days after activation and cell phenotype was analysed by flow cytometry nine days after activation.

Genetic deletion by CRISPR–Cas9

Design of small guide RNA (gRNA) for mouse IDH2 (gRNA 1: GGGCCACCCAGAAGTACAGTG; gRNA 2: GAGAGCCCTAACGGAACGATC), SDHB (gRNA: TCGAATGCAGACGTACGAGG), ACO2 (gRNA: GGTATCCTCACGGTGAAAGG), and α-KGDH (gRNA: GGACTTGTGCTGCTAAGTTA) was done using a publicly available gRNA design tool to improve on-target activity and reduce off-target activity[42]. Cloning of gRNAs in a self-inactivating version of the MSCV retroviral vector was done under the control of the pU6 promoter. Co-infection of Phoenix-Eco cells with gRNA retroviral plasmids and pCL-ECO allowed for the generation of retroviral particles, which were concentrated by ultracentrifugation. Two different gRNAs were pooled, aliquoted and stored at −80 °C until use.

Mouse $CD8^{+}$ T cells were isolated from conditional Cas9.Cd4-Cre P14 or OT1 mice splenocytes using the EasySep Mouse $CD8^{+}$ T Cell Isolation Kit (STEMCELL Technologies) following the manufacturer's protocol. Purified $CD8^{+}$ T cells were plated at 0.5×10^{6} cells per ml in RPMI 1640 supplemented as described above, containing rhIL-2 at 50 IU ml^{-1} and IDH2i or DMSO. Cells were activated using Activator CD3/CD28 Dynabeads (Gibco, 2 beads:1 cell ratio). Retroviral transduction was performed for 24 h in wells previously coated with recombinant human fibronectin (Takara Clontech) for 12 h at 4 °C and blocked with 2% BSA in phosphate-buffered saline (PBS) for 30 min at room temperature. Concentrated retroviruses were added to the fibronectin-coated wells and centrifuged for 90 min at 2,000*g* at 32 °C. Twenty-four-hour-activated $CD8^{+}$ T cells were placed in the fibronectin-coated wells containing retroviruses, and centrifuged for 10 min at 400*g* at 32 °C. Three days after transduction, the medium was changed for fresh medium containing rhIL-2 (10 IU ml), rhIL-7 (10 ng ml^{-1}), rhIL-15 (10 ng ml^{-1}).

Forty-eight hours after transduction, cells were expanded in completed RPMI containing 50 IU ml^{-1} rhIL-2. Five days later, activation beads were removed and $Thy1.1^{+}$ transduced cells were purified (STEMCELLl Technologies).

Preparation of mouse CAR T cells

Cloning of HER2-CAR and control BFP in the MSGV retroviral transfer vector was done[43] under the control of the 5′ LTR promoter[44]. The template plasmid pIG6-4D5, which contains the scFv fragment derived from the human-specific anti-HER2 mouse antibody 4D5, was used for the HER2-CAR (ref. 45; a gift from A. Pluckthun). Fusion of the single-chain antibody fragment to the CD8α hinge and transmembrane domains was followed by fusion to the mouse intracellular 4-1BB and CD3ζ signalling endodomains.

Calcium phosphate transfection of Phoenix-Eco cells with HER2-CAR or BFP plasmid and pCL-Eco-packaging plasmid was done and supernatant containing the produced virus was collected at 48 h and 72 h after transfection and ultracentrifuged.

Mouse $CD8^+$ T cells were isolated from the spleen of C56BL/6 mice, using the the EasySep Mouse $CD8^+$ T Cell Isolation Kit (STEMCELL Technologies) following the manufacturer's protocol. Purified $CD8^+$ T cells were plated at 0.5×10^6 cells per ml in RPMI 1640 supplemented as described above, containing rhIL-2 at 50 IU ml^{-1} (Peprotech, 200-02), and IDH2i or DMSO. Cells were activated using Activator CD3/CD28 Dynabeads (Gibco, 2 beads:1 cell ratio). Retroviral transduction was performed as described above in the 'Genetic deletion by CRISPR–Cas9' section.

Preparation of human CAR T cells

Anti-CD19 CAR T cells. The hCD19-28z CAR was constructed by ligating the hCD19 scFv (FMC63) into the CAR backbone sequences of a third-generation viral vector pTRPE-28z. Third-generation lentiviral vectors were produced as previously described[46]. In brief, 95% confluent HEK293T cells were transfected with the pTRPE, psPAX2 encoding gag-pol and pMD2.G encoding the VSV-G envelope, using Lipofectamine 2000 (Invitrogen). Viral supernatant was collected 24 h and 48 h after transfection, filtered, concentrated by ultracentrifugation and frozen. For the generation of CAR T cells, human T cells were enriched from peripheral blood by RosetteSep (STEMCELL Technologies). T cells were activated with human anti-CD3/CD28 Dynabeads (Gibco, 11131D) and cultured in RPMI supplemented with 10% FBS, 1 mM HEPES, 1% P/S and 1% non-essential amino acids (all Gibco). Twenty-four hours later, T cells were transduced with the lentiviral vector encoding anti-human CD19scFv fused to CAR backbones containing human CD28 and CD3ζ (CD247) signalling domains and expanded ex vivo for 12 days. Transduced T cells were maintained at a concentration of 0.75×10^6 cells per ml throughout the culture period by cell enumeration every two to three days. T cells were exposed to 5 μM AG-221 or DMSO over the entire culture period.

Anti-BCMA CAR T cells. The m11D5-3BBζ CAR construct was previously generated[47]. In brief, the 11D5-3 scFv was linked to the human CD8α hinge and transmembrane domains followed by the human 4-1BB and CD3ζ endodomains, and the CAR construct was ligated into the SFG retroviral vector backbone with a ΔCD271 selectable marker. Retroviral supernatant was produced by transiently co-transfecting 50% confluent 293T cells with (1) RDF plasmid encoding the RD114 envelope or a plasmid encoding the VSV-G envelope; (2) the Peg-Pam plasmid encoding MoMLV gag-pol or a plasmid encoding gag-pol; and (3) the SFG retroviral plasmid of interest or WGXIP retroviral plasmid, using GeneJuice transfection reagent (Merck, 70967-3). Retroviral supernatant was collected at 48 h and 72 h after transfection, filtered, snap-frozen and stored at −80 °C until use, or used fresh. For the generation of CAR T cells, PBMCs were isolated from buffy coats by density gradient centrifugation (Lymphoprep, STEMCELL Technologies, 07851) and were activated with human anti-CD3/CD28 Dynabeads (Gibco, 11131D). T cells were transduced with the retroviral vector and expanded ex vivo for 10 days in the presence of rhIL-2 at 150 IU ml^{-1} and either AG-221 5 μM or DMSO.

Mouse xenograft models

B-ALL xenograft model. Male NSG mice (8–10 weeks old) were inoculated with 10^6 Nalm6 cells in the tail vein. Fifteen days after NALM6 infusion, human CAR T cells were thawed and washed, and 2×10^6 CAR^+ cells were adoptively transferred into the tail vein. The body weight was frequently measured and the health of mice was monitored. When the physical and behavioural health of mice declined below the levels established by the Swiss cantonal authorities or when mouse body weight dropped by more than 15%, mice were euthanized. The numbers of NALM6 cells in the blood were measured by anti-human CD19 flow cytometry analysis.

Multiple myeloma xenograft model. To establish an in vivo stress test using the NCI-H929 myeloma xenograft model, the dose of BCMA CAR T cells was titrated down to a dose at which standard CAR T cells were only minimally effective. Female NSG mice (6–8 weeks old) were injected with 3×10^6 NCI-H929-GFP-FFluc myeloma cells intravenously in the tail vein at day 0 (ref. 47). Tumour burden was monitored by bioluminescence imaging (BLI) (photons per second per cm^2 per steradian) using the Xenogen in vivo imaging system (IVIS) (Caliper Life Sciences) using Living Image software (v.4.7.3, 64 bit). Mice were randomized on the basis of BLI intensity. One dose of 0.5×10^6 T cells was administered intravenously at day 10 after tumour engraftment, and tumour growth was monitored by BLI. The survival of mice was determined according to humane end-points as defined in the score sheet of the approved animal protocol.

LCMV infection model

Whole-body Cas9 mice were infected with 200,000 PFU of LCMV-Armstrong by intraperitoneal injections. The same day, P14 Cas9. Cd4-Cre $CD8^+$ T cells were isolated and activated for transduction as described above. Twenty-four hours later, activated T cells were transduced with *Idh2* gRNA as explained above and injected into infected recipients six hours after transduction. Tail-vein blood sampling was performed at different time points. Thirty-five days after infection, transduced $CD8^+$ T cells were sorted by fluorescence-activated cell sorting (FACS) on the basis of their Thy1.1 expression, and transferred into *Rag1*-knockout recipients, which were infected with LCMV-Armstrong (200,000 PFU, intraperitoneal) the following day.

Plaque assay

Vero cells were grown in DMEM containing 10% FBS and 1% P/S, to a loose confluence, resuspended in medium, counted and diluted to 8×10^5 cells per ml. Mouse kidneys were collected and directly frozen at −80 °C. Kidneys were then smashed in MEM-5 and solution was used for serial dilutions, which were then plated in 24-well plates. Vero cells were added to the serial dilutions of kidney preparations and the mixture was incubated for 3 h at 37 °C. Wells were gently coated with 2× DMEM methylcellulose (1:1 ratio; FLUKA 64620) and incubated for 60–72 h at 37 °C.

Staining was performed as follows. The supernatant was aspired and cells were fixed with 4% PFA for 30 min at room temperature. Cells were washed and incubated with Triton X-100 (FLUKA 93418) for 20 min at room temperature. After the removal of Triton, cells were incubated with 5% FBS in PBS for 20 min at room temperature. Cells were washed and incubated with 2% FBS in PBS containing VLA-4 antibody (BioXcell) for 60 min at room temperature. Cells were washed twice with PBS and incubated with secondary antibody Peroxidase AffiniPure Goat Anti-Rat IgG (Jackson ImmunoResearch Laboratories) in 2% FBS in PBS for 60 min at room temperature. Cells were washed twice in PBS and incubated with freshly prepared ortho-phenylenediamine (Sigma-Aldrich, P3888) and 30% H_2O_2 perhydrol (Sigma-Aldrich, 216763) for 15 min, until a brown colour appeared. Cells were washed twice with PBS, plaques were counted and PFU calculated using the formula: PFU per ml = number of counts × dilution steps.

Listeria infection model

For IDH2 pharmacological inhibition, splenocytes from OT1 mice were activated and cultured in vitro for seven days with DMSO or AG-221 (IDH2i) as described above, collected and purified on a Ficoll gradient, allowing dead and live T cells to be separated. For genetic deletion of *IDH2*, OT1 Cas9.Cd4-Cre $CD8^+$ T cells were transduced with *Idh2* gRNA as described above, and transduced T cells were isolated after eight days on the basis of their Thy1.1 expression (STEMCELL Technologies). A total of 100,0000 DMSO- or IDH2i-conditioned T cells were injected into the tail vein of C57BL/6 mice, and 10,000 Thy1.1-positive Scr- or *Idh2* gRNA-transduced T cells were injected into whole-body Cas9 mice.

Recombinant *L. monocytogenes* deficient for actA and expressing the OVA peptide SIINFEKL were grown and titrated. Bacterial concentration was calculated using spectrophotometer-measured optical density, and 2,000 colony-forming units (CFU) were injected in the tail of each mouse 4 h after T cell transfer. Tail-vein blood sampling was performed at different time points.

Tumour models

Engraftment of either 10^6 OVA-expressing Yumm1.7, 10^5 OVA-expressing B16-F10 or 4×10^5 HER2-expressing B16-F10 tumour cells was performed in recipient C57BL/6 mice. Mice were lymphodepleted six days after tumour engraftment, either by whole-body irradiation with 5 Gy (RS2000, Rad Source, for B16-OVA and Yumm1.7-OVA) or by intraperitoneal injection of 100 mg kg^{-1} cyclophosphamide (Sigma-Aldrich, C7397, for B16-HER2). Randomization was performed according to tumour volume and 10^5 IDH2i- or DMSO-conditioned T cells (for Yumm1.7-OVA and B16-OVA) and 5×10^6 BFP or HER2-CAR T cells were adoptively transferred intravenously. B16-OVA and Yumm1.7-OVA tumour-bearing mice were administered a vaccine consisting of CpG-ODN oligonucleotide (Microsynth, 45355) and OVA peptide (Sigma-Aldrich) at the time of T cell transfer. Tumours were measured with a caliper every two days and volumes were calculated using the formula: $V = \pi \times (d^2 \times D)/6$, in which d is the minor tumour axis and D is the major tumour axis. Mice bearing tumours larger than 1 g were euthanized. Tumours were dissected and single-cell suspensions were obtained using the Mouse Tumour Dissociation Kit (Miltenyi, 130–096-730) following the manufacturer's protocol. Draining lymph nodes and spleens were smashed on a 70-µm cell strainer. Antibody staining was done on single-cell suspensions for flow cytometry analysis.

Flow cytometry

Fluorochrome-conjugated antibodies were all from BioLegend or Thermo Fisher Scientific and non-conjugated antibodies were from Cell Signaling. Staining for flow cytometry was done in PBS with 2% FBS and 2 mM EDTA, at 4 °C in the dark. The LIVE/Dead Fixable Blue Cell Stain Kit (Thermo Fisher Scientific) was used to mark dead cells. The FOXP3 staining kit (Thermo Fisher Scientific) was used for intracellular staining, following the manufacturer's instructions. HER2-CAR T cells were stained with recombinant human Fc-tagged Her2/ErbB2 protein (Sino Biological) and anti-human-Fc Alexa Fluor 488 conjugate (Thermo Fisher Scientific).

Acquisition was done on LSR II, Fortessa and Cytek Aurora flow cytometers with FACSDiva Software.

The flow cytometry gating strategy is provided in Supplementary Fig. 2.

Seahorse assay

The extracellular flux assay was performed with a Seahorse XF96 Extracellular Flux Analyzer, following the manufacturer's protocol. In brief, T lymphocytes were plated in a cell-TAK (Corning, 354241) coated Seahorse plate with a density of 200,000 cells per well. Cells were treated successively with oligomycin (2 µM), FCCP (2 µM), rotenone (0,5 µM), antimycin A (0,5 µM), etomoxir (50 µM), BPTES (5 µM) and UK5099 (10 µM). The OCR was measured by the analyzer.

Colorimetric and fluorometric assays

The histone multiplex assay was done using the EpiQuik Histone H3 Modification Multiplex Assay Kit (BioCat, P-3100-96-EP), and the KDM5 activity assay was done using the KDM5/JARID Activity Quantification Assay Kit Fluorometric (Abcam, ab113464), according to the manufacturer's protocol, using 100 ng of extracted histones (for the EpiQuik Histone H3 Modification Multiplex Assay) and 10 µg of nuclear extract (for the KDM5 activity assay) as starting material. The α-KG assay was done using the colorimetric α-KG Assay Kit (Abcam, ab83431) and the 2-HG assay was done using the D 2 Hydroxyglutarate Assay Kit (Abcam, ab211070) according to the manufacturer's protocol, using 10 million cells as starting material. Glutamine and glucose were detected in the cell culture supernatant using the Glutamine Assay Kit (Sigma-Aldrich, mak438) and the Glucose Assay Kit (Sigma-Aldrich, mak263), respectively, according to the manufacturer's protocol. OT1 cells were activated in the presence of DMSO or IDH2i as described above. The medium was replaced at day 2 and the supernatant was collected at day 3 after activation to measure glucose and glutamine consumption over 24 h. Glutamine consumption was also measured in T_E and T_M cells at day 3 and day 7 after activation, respectively. The culture medium was replaced at day 2 (T_E cells) and day 6 (T_M cells) and the supernatant was collected at day 3 (T_E cells) and day 7 (T_M cells) after activation. Glutamine and glucose consumption were then normalized with cellular protein content.

RNA extraction and qPCR

For analysing upstream regulation of IDH gene expression, mouse $CD8^+$ T cells were isolated from the spleen from OT1 mice using the EasySep Mouse $CD8^+$ T Cell Isolation Kit (STEMCELL Technologies) following the manufacturer's protocol. Purified $CD8^+$ T cells were plated at 10^6 cells per ml in RPMI 1640 supplemented as described above, containing rhIL-2 at 100 IU ml^{-1}, and cells were activated using Activator CD3/CD28 Dynabeads (Gibco, 2 beads:1 cell ratio). Twenty-four hours after activation, cells were treated with an mTOR inhibitor (Torin 2, Sigma-Aldrich, SML1224, 500 nM), a HIF-1α inhibitor (Echinomycin, Abcam, ab144247-1, 100 nM) or a MYC inhibitor (10058-F4, c-Myc-Max dimerization inhibitor, Abcam, ab145065, 100 µM). Cells were lysed at day 3 after activation.

For the analysis of $CD8^+$ T cell subsets over the course of a bacterial infection, mouse $CD45.1^+$ $CD8^+$ T cells were isolated from the spleen of OT1 mice using the EasySep Mouse $CD8^+$ T Cell Isolation Kit (STEMCELL Technologies) and adoptively transferred into recipient C57BL/6 (B6) $CD45.2^+$ mice, which were subsequently infected with LM-OVA (2,000 CFU). $CD45.1^+$ $CD8^+$ T cells were then sorted by FACS for RNA extraction at different time points after infection.

RNA was extracted using the Qiagen RNA isolation kit (Qiagen). cDNA was converted from mRNA using SuperScript III Reverse Transcriptase (Thermo Fisher Scientific). Quantitative PCR (qPCR) was done with a LightCycler 480 Instrument II (Roche Life Science) using KAPA SYBR FAST qPCR Kit Master Mix (KAPA Biosystems) according to the manufacturer's instructions. Relative expression was normalized by the expression of β2-microglobulin (β2M forward: AGA CTGATACATACGCCTGCAG; reverse: GCAGGTTCAAATGAATC TTCAG; PDK1 forward: 5′-GGGCCAGGTGGACTTCTATG; reverse: 5′-TGGATATACCAACTTTGCACC; GLUT1 forward: TGGCAGGCTGTG CTGTGCTCATGAC; reverse: AAGCCAGCCACAGCAATAGCAGCA; IDH1 forward: AGTCCAGAGTGAAGAGGGTT; reverse: ACTTGACGCCC ACGTTGTAT; IDH2 forward: GTACAACACCGACGAGTCCAT; reverse: AGCCTCAGCCTCAATTGTCT; IDH3A forward: AGGGAAGTTGCGGAG AACTG; reverse: GGGCTGTTCCATGAACCGAT).

Western blotting

Whole-cell lysis was done in RIPA lysis buffer (50 mM Tris-HCl pH 8, 150 mM NaCl, 1% Triton X-100, 0.5% sodium deoxycholate and 0.1%

SDS) to which 500 μM of fresh protease inhibitors (4-(2-aAminoethyl) benzenesulfonyl fluoride hydrochloride; Sigma-Aldrich) and phosphatase inhibitors (Phosstop; Sigma-Aldrich) were added. For histone analyses, nuclei were isolated and washed in Triton extraction buffer (PBS containing 0.5% Triton X-100) containing 5 mM sodium butyrate and 500 μM protease inhibitor, and histones were acid-extracted with 0.2 M HCl, followed by precipitation with trichloroacetic acid. Histones were then resuspended in 50 mM Tris-HCl.

Whole-cell-lysate proteins were quantified with a BCA protein assay kit (Thermo Fisher Scientific) and histone extracts were quantified with Bradford reagent (Sigma-Aldrich). Equal amounts of proteins were denatured for 5 min at 95 °C in SDS loading dye containing 5% β-mercaptoethanol, followed by separation on 12.5% polyacrylamide gradient gels and transferring onto 0.2 μM nitrocellulose membranes (Bio-Rad). After transfer, blocking of unspecific binding sites was done in 5% milk and incubation with primary antibodies (Cell Signaling, GeneTex, Santa Cruz Biotechnology) was done overnight at 4 °C. The next day, membranes were incubated with HRP-conjugated secondary anti-rabbit and anti-mouse antibodies (Santa Cruz Biotechnology). Chemiluminescence imaging was performed with ECL and Femto reagents (Super Signal West, Thermo Fisher Scientific).

Uncropped blots are available in Supplementary Fig. 1.

^{13}C-glutamine, ^{13}C-glucose and ^{13}C-palmitate labelling and liquid chromatography–high-resolution mass spectrometry metabolomics

To detect glutamine, glucose and fatty acid metabolism in T_E versus T_M cells and after pharmacological inhibition of IDH2, splenocytes from OT1 were activated as described above. For IDH2 inhibition experiments, cells were either activated and cultured in 21% O_2 and 5% CO_2, or placed in a hypoxic hood set at 2% O_2 and 5% CO_2. At day 3 after activation, cells were washed with PBS and cultured for 2 h with [U-^{13}C]-glutamine (for the IDH2i experiment; in either 21% O_2 or 2% O_2 conditions), with [1-^{13}C]-glutamine (for the T_E versus T_M in vitro differentiation experiment), with [U-^{13}C]-glucose or with [U-^{13}C]-palmitate. To detect RC after genetic deletion of *IDH2*, OT1 OT1 Cas9.Cd4-Cre CD8$^+$ T cells were activated, transduced and cultured as described above. At day 7 after activation, transduced cells were isolated on the basis of their Thy1.1 expression and were rested for 24 h. Next, cells were restimulated for 70 h with Activator CD3/CD28 Dynabeads (Gibco, 2 beads:1 cell ratio) and then labelled for 2 h with [1-^{13}C]-glutamine. Cells were all labelled in glucose- and glutamine-free RPMI (Biological Industries) containing 10% dialysed FBS (Thermo Fisher Scientific), 1% HEPES, 1% P/S, 50 μM β-mercaptoethanol, 1× non-essential amino acids, 11 mM glucose (Sigma-Aldrich, G7021) or 11 mM [U-^{13}C]-glucose, 4 mM [U-^{13}C]-glutamine or 4 mM [1-^{13}C]-glutamine (Cambridge Isotope Laboratories) or 4 mM L-glutamine (Gibco, 25030-081), and DMSO or IDH2i when applicable. For the palmitate labelling experiment, cells were labelled for 6 h in glucose- and glutamine-free RPMI (Biological Industries) containing 10% dialysed FBS (Thermo Fisher Scientific), 1% HEPES, 1% P/S, 11 mM glucose (Sigma-Aldrich, G7021), 4 mM L-glutamine (Gibco 25030-081), DMSO or AG-221 and [U-^{13}C]-palmitate dissolved in ethanol at 0.2% of the final volume. Cells were then washed once with PBS, and pellets were snap-frozen in liquid nitrogen and stored at −80 °C. Metabolites were extracted by resuspending frozen pellets in 80% methanol containing 2 μM d27 myristic acid. Samples were centrifuged at 20,000*g* for 15 min at 4 °C, supernatant containing metabolites was analysed as described below and protein pellets were resuspended in NaOH, heated at 95 °C for 20 min, cooled down, spun for 10 min at 5,000 rpm and used for BCA analyses.

Absolute quantification of 2-hydroxyglutaric acid, citric acid, fumaric acid, malic acid and succinic acid was performed using a strategy described previously[48]. In brief, 50 μl of each sample was transferred to a new tube, while a pool consisting of aliquots from all samples was composed in a separate tube. The samples and a standard mix of the target compounds with known concentrations were then derivatized with ^{12}C dimethylaminophenacyl bromide (DmPA), and the pool sample with ^{13}C DmPA. Each derivatized sample and the standard mix was mixed with an equal amount of derivatized pool sample and transferred to MS vials. The absolute concentrations of the ^{12}C derivatized target compounds were calculated on the basis of the abundances of the ^{13}C derivatized target compounds from the pool sample spiked in each sample and standard. Samples were analysed using a platform consisting of a Vanquish UHPLC (Thermo Fisher Scientific) equipped with a C-18 column (Aquity UPCL BEH 1.7 μm 2.1 × 150 mm) coupled to a Q Exactive Orbitrap Focus mass spectrometer (Thermo Fisher Scientific) operating in positive-ion mode. The samples were analysed in sequential order and a derivatized standard was analysed before and after the samples. A step gradient was carried out using solvent A (formic acid 0.1% in mQ) and solvent B (acetonitrile in 0.1% formic acid). Samples (10 μl) were loaded at 0.2% of solvent B and from 1 to 25 min a ramp to 99.8% solvent B was carried out. From minute 25 to 27.5 the gradient was kept constant (99.8% B). The gradient returned to initial conditions (99.8% A) and was kept constant for 4.5 min. The flow rate was held constant at 250 μl per min. The mass spectrometer operated in full-scan (range 120–1200) and positive mode using a spray voltage of 3.2 kV, capillary temperature of 320 °C, sheath gas at 15.0 and auxiliary gas at 2.0. The AGC target was set at 1e6 using a resolution of 70,000.

A different platform was used for the absolute quantification of α-KG, by running an external calibration using an α-KG standard series (0, 0.5, 1, 2, 5 and 25 μM), and for the relative quantification of all other metabolites. Ten microlitres of each sample supernatant was loaded into a Dionex UltiMate 3000 LC System (Thermo Fisher Scientific) equipped with a C-18 column (Acquity UPLC -HSS T3 1. 8 μm; 2.1 × 150 mm, Waters) coupled to a Q Exactive Orbitrap mass spectrometer (Thermo Fisher Scientific) operating in negative-ion mode. A step gradient was carried out using solvent A (10 mM TBA and 15 mM acetic acid) and solvent B (100% methanol). The gradient started with 5% of solvent B and 95% solvent A and remained at 5% B until 2 min after injection. A linear gradient to 37% B was used until 7 min and increased to 41% until 14 min. Between 14 and 26 min the gradient increased to 95% of B and remained at 95% B for 4 min. At 30 min the gradient returned to 5% B. The chromatography was stopped at 40 min. The flow was kept constant at 0.25 ml per min at the column was placed at 40 °C throughout the analysis. The mass spectrometer operated in full-scan mode (*m*/*z* range: (70.0000–1050.0000]) using a spray voltage of 4.80 kV, capillary temperature of 300 °C, sheath gas at 40.0 and auxiliary gas at 10.0. The AGC target was set at 3e6 using a resolution of 140,000, with a maximum IT fill time of 512 ms.

Data from both platforms was collected using Xcalibur software, and analysed using El-Maven and Polly (Elucidata).

For the estimation of the intracellular concentration of TCA metabolites, we have first estimated the volume of an activated T cell. We measured the average diameter (11 μm) of the T cells using the CountessII (Invitrogen). We then calculated the volume assuming that T cells are spherical: 696.9 μm^3, which we used to derive the volume of 1 cell: 0.6969 pl. Because the absolute quantification of the TCA metabolites was normalized per μg of protein, we calculated that 1 million activated T cells represent on average 75 μg of protein. This allowed us to estimate the intracellular concentration of the TCA metabolites.

Pathway enrichment analysis

Pathway analysis was performed with the online publicly available software Enrichr[23]. Genes assigned to sets of differentially accessible regions were compared to gene sets from the TRRUST 2019 database (https://www.grnpedia.org/trrust/) (for ATAC-seq data as well as combined ATAC-seq and RNA-seq data) and genes that were upregulated after IDH2 inhibition were compared to gene sets from the Elsevier Pathway Collection.

Expression level of IDH genes in yellow-fever-specific CD8 T cells

Normalized raw counts data from RNA-seq of human yellow-fever-specific T cells were retrieved from GSE100745, imported into R (v.3.5.3) and converted to $\log_2$(normalized counts + 1) (ref. 16). To determine the fold change of genes among T_N, T_E and T_M cells, we fitted a linear model to each gene using the lmFit function of the limma[49] package (v.3.38.3), followed by moderated *t*-statistic computation with the eBayes function. We also converted gene-expression levels to RPKM by obtaining the length of human transcripts using biomaRt (v.2.38.0)[50]. The RPKM was calculated at the gene level by using the length of the longest transcript and the rpkm function of the edgeR (v.3.24.3) package[51].

HIF-1α- and MYC-binding motifs in the promoter of *IDH2*

The promoter region of *IDH2* for both the human genome and the mouse genome was obtained from the Eukaryotic Promoter Database (EPDnew)[52]. For the analysis of the human genome, the location of HIF-1α- and MYC-binding sites compiled from ChIP–seq data ('meta clusters') was obtained from the Gene Transcription Regulation Database (GTRD)[53]. We verified whether or not HIF-1α- and MYC-binding sites overlapped with the *IDH2* promoter using the Integrative Genomics Viewer (IGV v.2.8.0; *Homo sapiens* hg38).

For the analysis of the mouse genome, we obtained the motif of the HIF-1α and MYC transcription factors from the Jaspar2022 database (https://jaspar.genereg.net/). The best match for these motifs was searched within a region extending ±2 kb from the promoter region of *Idh2* using the FIMO tool of the online MEME Suite (v 5.3.2; https://meme-suite.org/meme/meme_5.3.2/). The location of the HIF-1α and MYC motifs within the extended Idh2 promoter region was visualized with IGV (*Mus musculus* mm10).

RNA-seq analysis

Splenocytes from OT1 mice were activated and cultured as described above, in the presence of either AG-221 5 μM or DMSO. Seven days after activation, cells were gently washed with PBS and RNA was collected and extracted using the Qiagen RNA isolation kit (Qiagen), according to the manufacturer's instructions. RNA quality was assessed on a Fragment Analyzer (Agilent Technologies). All RNAs had an RQN between 9.4 and 10. RNA-seq libraries were prepared from 500 ng of total RNA with the Illumina TruSeq Stranded mRNA reagents (Illumina) using a unique dual indexing strategy, and following the official protocol automated on a Sciclone liquid handling robot (Perkin Elmer). Libraries were quantified by a fluorometric method (QubIT, Life Technologies) and their quality was assessed on a Fragment Analyzer (Agilent Technologies).

Cluster generation was performed with 2 nM of an equimolar pool from the resulting libraries using the Illumina HiSeq 3000/4000 SR Cluster Kit reagents, followed by sequencing on the Illumina HiSeq 4000 using HiSeq 3000/4000 SBS Kit reagents for 150 cycles (single read). Sequencing data were demultiplexed using the bcl2fastq2 Conversion Software (v.2.20, Illumina).

Sequencing reads were pre-processed and aligned to the mouse genome using the RNA-seq method of the bcbio-nextgen pipeline (v.20.11). The reads were first trimmed for quality and adapter using Atropos (v.1.1.28)[54]. Trimmed reads were aligned to the *Mus musculus* genome (mm10) using hisat2 (v.2.2.1)[55]. Numbers of reads were summarized at the gene level per sample using htseq-count function of HTSeq (v.0.9.1)[56]. Raw counts were imported into R (v.3.5.3). Genes were filtered to only retain the ones expressed at one count per million in at least one sample. The raw counts were then pre-processed using the voomWithQualityWeights function of the limma package (v.3.38.3), using the mouse ID of each sample as a covariate in the design matrix. Next, a linear model was fitted for every gene with the lmFit function, and moderated *t*-statistics were computed using the eBayes function for the Idh2i versus the DMSO contrast. Genes with $P < 0.05$ after Benjamini–Hochberg adjustment were considered as significantly differentially expressed between IDH2i- and DMSO-conditioned cells.

GSEA[57] for genes linked to the memory phenotype was performed using the clusterProfiler package (v.4.0.5) for R (v.4.1.0)[58]. A set of memory-related gene sets was obtained from the Molecular Signature Database (MSigDB), and subjected to GSEA using the GSEA function, with parameters eps = 1e-60, pvalueCutoff = 1, seed = T and a seed = 1234.

ATAC-seq analysis

Splenocytes from OT1 mice were activated and cultured in the presence of AG-221 or DMSO for seven days, following the above protocol, and a previously described ATAC-seq protocol was followed[59]. In brief, at day 7 after activation, 5×10^4 T cells were washed with ice-cold 1 × PBS and resuspended in 50 μl of ice-cold lysis buffer (10 mM Tris-Cl (pH 7.4), 10 mM NaCl, 3 mM $MgCl_2$ and 0.1% (v/v) NP-40). Cells were centrifuged, and pellets containing nuclei were resuspended in 50 μl of transposase reaction mix (25 μl 2× TDbuffer, 2.5 μl Tn5 transposase (Illumina) and 22.5 μl of nuclease-free water), and incubated for 30 min at 37 °C. The Qiagen MinElute PCR Purification kit was used to clean tagmented DNA and library preparation was done with custom Nextera PCR primers previously described[60] and NEBNext High-Fidelity 2X PCR Master Mix (M0541), with the program: 5 min 72 °C, 30 s 98 °C; 10 cycles: 10 s 98 °C, 30 s 63 °C, 1 min 72 °C. Agencourt AMPure XP magnetic beads (A63880, Beckman) were used to clean libraries, which were then quantified using a Fragment Analyzer and sequenced on an Illumina HiSeq 4000 with paired-end 75 nucleotides at the Gene Expression Core Facility at the Ecole Polytechnique Fédérale de Lausanne. Filtration of low-quality reads and trimming were done with AdapterRemoval (v.2.1.7)[61].

Sequencing reads were pre-processed and aligned to the mouse genome using the bcbio-nextgen pipeline (v.19.03). Reads were first trimmed for quality and adapter using Atropos (v.1.1.21), and aligned to the *Mus musculus* genome (mm10) using bwa (v.0.7.17-r1188)[62]. Reads were shifted to correct for the transposon event. Peak calling was performed using MACS2 (v.2.1.1.20160309), using the --broad option, generating one broad peak list for IDH2i-conditioned samples, and one for the DMSO-conditioned samples. Differential chromatin accessibility analyses were next performed within R (v.3.5.3) using the DiffBind (v.2.10.0) package[63]. Counts per genomic region were computed using the dba.count function, with the parameter Score=DBA_SCORE_TMM_READS_FULL. Differential accessibility analysis was performed with the edgeR implementation within the dba.analyze function. All peaks were annotated to nearest genes using the annotatePeakInBatch function of the ChIPpeakAnno package (v.3.16.1)[64] and the mouse transcription start site annotation (GRCm38.p1), with parameters output = "overlapping", bindingType = "fullRange", PeakLocForDistance = "middle" and bindingRegion = c(-15000,15000). A peak that was located further upstream of *Tcf7* but fell within a known enhancer region was manually annotated to *Tcf7* (ref. 65). Enrichment of transcription-factor-binding motifs within the chromatin regions that were more accessible after IDH2 inhibition was performed using Homer (v.4.11.1). For GSEA of memory-related gene signatures, only one peak per gene was used by retaining the one that had the highest absolute $\log_2$-transformed fold-change value. The $\log_2$-transformed fold-change values were provided to the GSEA function of the clusterProfiler package with parameters eps = 1e-50, pvalueCutoff = 1, seed = T and a seed = 1234.

Finally, for genes that were both significantly differentially expressed at the mRNA level and had associated more accessible chromatin regions (that is, 52 genes), we performed an over-representation analysis of memory-related gene signatures using the enricher function of the clusterProfiler package.

Raw sequencing and pre-processed RNA-seq (GSE192395) and ATAC-seq (GSE192394) data were deposited in the NCBI's Gene Expression Omnibus (GEO) with the SuperSeries accession number GSE192396.

Quantification and statistical analysis

FlowJo v.10 was used to analyse flow cytometry data. ImageJ software was used for the quantification of western blots. Prism v.9 software (GraphPad) was used for statistical analyses. Results are represented as mean ± s.e.m. Information on each statistical test used is provided in the figure legends, with the sample size and number of independent repeats. Two group comparisons were tested by unpaired two-tailed Student's *t*-tests. Comparisons of more than two groups were done with one-way ANOVA and Tukey's multiple comparison correction. Grouped data comparisons were calculated using two-way ANOVA with the original FDR method of Benjamini and Hochberg. Sample sizes were based on previous experience. Graft rejection or death led to the exclusion of some mice from analyses. Samples were excluded from flow cytometric analyses when the number of events recorded was lower than 20 in the population of interest, preventing accurate analyses.

Reporting summary

Further information on research design is available in the Nature Portfolio Reporting Summary linked to this article.

Data availability

The data supporting the findings of this study are available within the paper and its Supplementary Information. RNA-seq data are available in the NCBI's GEO database under the accession code GSE192395. ATAC-seq data are available in the NCBI's GEO database under the accession code GSE192394. Source data are provided with this paper.

40. Yen, K. et al. AG-221, a first-in-class therapy targeting acute myeloid leukemia harboring oncogenic *IDH2* mutations. *Cancer Discov.* **7**, 478–493 (2017).
41. Wang, F. et al. Targeted inhibition of mutant IDH2 in leukemia cells induces cellular differentiation. *Science* **340**, 622–626 (2013).
42. Doench, J. G. et al. Optimized sgRNA design to maximize activity and minimize off-target effects of CRISPR–Cas9. *Nat. Biotechnol.* **34**, 184–191 (2016).
43. Coren, L. V., Jain, S., Trivett, M. T., Ohlen, C. & Ott, D. E. Production of retroviral constructs for effective transfer and expression of T-cell receptor genes using Golden Gate cloning. *Biotechniques* **58**, 135–139 (2015).
44. Tschumi, B. O. et al. CART cells are prone to Fas- and DR5-mediated cell death. *J. Immunother. Cancer* **6**, 71 (2018).
45. Worn, A. & Pluckthun, A. An intrinsically stable antibody scFv fragment can tolerate the loss of both disulfide bonds and fold correctly. *FEBS Lett.* **427**, 357–361 (1998).
46. Tatari, N. et al. Preclinical testing of CAR T cells in a patient-derived xenograft model of glioblastoma. *STAR Protoc.* **1**, 100174 (2020).
47. Camviel, N. et al. Both APRIL and antibody-fragment-based CAR T cells for myeloma induce BCMA downmodulation by trogocytosis and internalization. *J. Immunother. Cancer* **10**, e005091 (2022).
48. Guo, K. & Li, L. Differential ^{12}C-/^{13}C-isotope dansylation labeling and fast liquid chromatography/mass spectrometry for absolute and relative quantification of the metabolome. *Anal. Chem.* **81**, 3919–3932 (2009).
49. Ritchie, M. E. et al. limma powers differential expression analyses for RNA-sequencing and microarray studies. *Nucleic Acids Res.* **43**, e47 (2015).
50. Durinck, S., Spellman, P. T., Birney, E. & Huber, W. Mapping identifiers for the integration of genomic datasets with the R/Bioconductor package biomaRt. *Nat. Protoc.* **4**, 1184–1191 (2009).
51. Robinson, M. D., McCarthy, D. J. & Smyth, G. K. edgeR: a Bioconductor package for differential expression analysis of digital gene expression data. *Bioinformatics* **26**, 139–140 (2010).
52. Dreos, R., Ambrosini, G., Groux, R., Cavin Perier, R. & Bucher, P. The eukaryotic promoter database in its 30th year: focus on non-vertebrate organisms. *Nucleic Acids Res.* **45**, D51–D55 (2017).
53. Kolmykov, S. et al. GTRD: an integrated view of transcription regulation. *Nucleic Acids Res.* **49**, D104–D111 (2021).
54. Didion, J. P., Martin, M. & Collins, F. S. Atropos: specific, sensitive, and speedy trimming of sequencing reads. *PeerJ* **5**, e3720 (2017).
55. Kim, D., Paggi, J. M., Park, C., Bennett, C. & Salzberg, S. L. Graph-based genome alignment and genotyping with HISAT2 and HISAT-genotype. *Nat. Biotechnol.* **37**, 907–915 (2019).
56. Anders, S., Pyl, P. T. & Huber, W. HTSeq—a Python framework to work with high-throughput sequencing data. *Bioinformatics* **31**, 166–169 (2015).
57. Subramanian, A. et al. Gene set enrichment analysis: a knowledge-based approach for interpreting genome-wide expression profiles. *Proc. Natl Acad. Sci. USA* **102**, 15545–15550 (2005).
58. Yu, G., Wang, L. G., Han, Y. & He, Q. Y. clusterProfiler: an R package for comparing biological themes among gene clusters. *OMICS* **16**, 284–287 (2012).
59. Buenrostro, J. D., Wu, B., Chang, H. Y. & Greenleaf, W. J. ATAC-seq: a method for assaying chromatin accessibility genome-wide. *Curr. Protoc. Mol. Biol.* **109**, 21.29.1–21.29.9 (2015).
60. Buenrostro, J. D., Giresi, P. G., Zaba, L. C., Chang, H. Y. & Greenleaf, W. J. Transposition of native chromatin for fast and sensitive epigenomic profiling of open chromatin, DNA-binding proteins and nucleosome position. *Nat. Methods* **10**, 1213–1218 (2013).
61. Schubert, M., Lindgreen, S. & Orlando, L. AdapterRemoval v2: rapid adapter trimming, identification, and read merging. *BMC Res. Notes* **9**, 88 (2016).
62. Li, H. & Durbin, R. Fast and accurate short read alignment with Burrows–Wheeler transform. *Bioinformatics* **25**, 1754–1760 (2009).
63. Ross-Innes, C. S. et al. Differential oestrogen receptor binding is associated with clinical outcome in breast cancer. *Nature* **481**, 389–393 (2012).
64. Zhu, L. J. et al. ChIPpeakAnno: a Bioconductor package to annotate ChIP–seq and ChIP–chip data. *BMC Bioinformatics* **11**, 237 (2010).
65. He, B. et al. $CD8^+$ T cells utilize highly dynamic enhancer repertoires and regulatory circuitry in response to infections. *Immunity* **45**, 1341–1354 (2016).

Acknowledgements We thank C. Vuillefroy de Silly for technical assistance; G. Gyülvészi for scientific discussion; and M. Mittelbrunn and S.-S. Im for providing TFAM and IDH2 KO splenocytes. Metabolomic analysis was performed at the VIB Metabolomics Core at the University of Leuven; RNA library preparation and RNA-seq were performed at the Lausanne Genomic Technologies Facility, University of Lausanne; and ATAC-seq was performed at the Gene Expression Core Facility at the Ecole Polytechnique Fédérale de Lausanne. D.M. is supported by the ISREC Foundation, PHRT Foundation, Ligue Genevoise Contre le Cancer, Fondation Dr Henri Dubois-Ferrière Dinu Lipatti and the Swiss Innovation Agency (Innosuisse). M.W., P.-C.H. and P.R. were supported in part by a grant from Roche. P.R. was supported in part by the SNSF grant 310030_182735 and Oncosuisse KFS-4404-02-2018. P.-C.H. is funded in part by a European Research Council Starting Grant (802773-MitoGuide), a European Molecular Biology Organization (EMBO) Young Investigator award, SNSF project grants (31003A_182470), the Cancer Research Institute (Lloyd J. Old STAR award) and a Melanoma Research Alliance Established Investigator award. N.M.-P. was funded by the EMBO and the European Federation of Immunological Societies (EFIS). C.A. receives funding from Swiss Cancer Research KFS-4542-08-2018-R, Stiftung für Krebsbekämpfung, Fondation Leenaards, Helmut Horten Stiftung and Fondation Muschamp. J.A.R. was a recipient of a Swiss Government Excellence Scholarship.

Author contributions A.J. conceived, designed and performed most experiments, analysed data and wrote the manuscript. T.W. performed bioinformatics analyses. N.M.-P., A.L., N.C. and C.V.G. performed experiments on human T cells. J.A.R. contributed to BCMA CAR T cell experiments and analysis. A.B. provided assistance with Seahorse experiments. J.-J.P., F.F. and K.-C.K. helped with cloning. B.G. supervised metabolomics experiments. C.A., D.M. and F.M. designed and supervised human CAR T cell experiments and provided scientific input. C.A. edited the manuscript. P.R. and P.-C.H. provided scientific input, supervised the project and edited the manuscript. M.W. conceived the study, designed experiments, analysed data, supervised the project and wrote the manuscript.

Competing interests P.R. and M.W. are inventors on a patent application filed by the University of Lausanne related to memory induction by IHD2 inhibition and its application in cellular therapies. The remaining authors declare no competing interests.

Additional information

Supplementary information The online version contains supplementary material available at https://doi.org/10.1038/s41586-023-06546-y.

Correspondence and requests for materials should be addressed to Pedro Romero, Ping-Chih Ho or Mathias Wenes.

Peer review information *Nature* thanks Stephen Gottschalk and the other, anonymous, reviewers for their contribution to the peer review of this work.

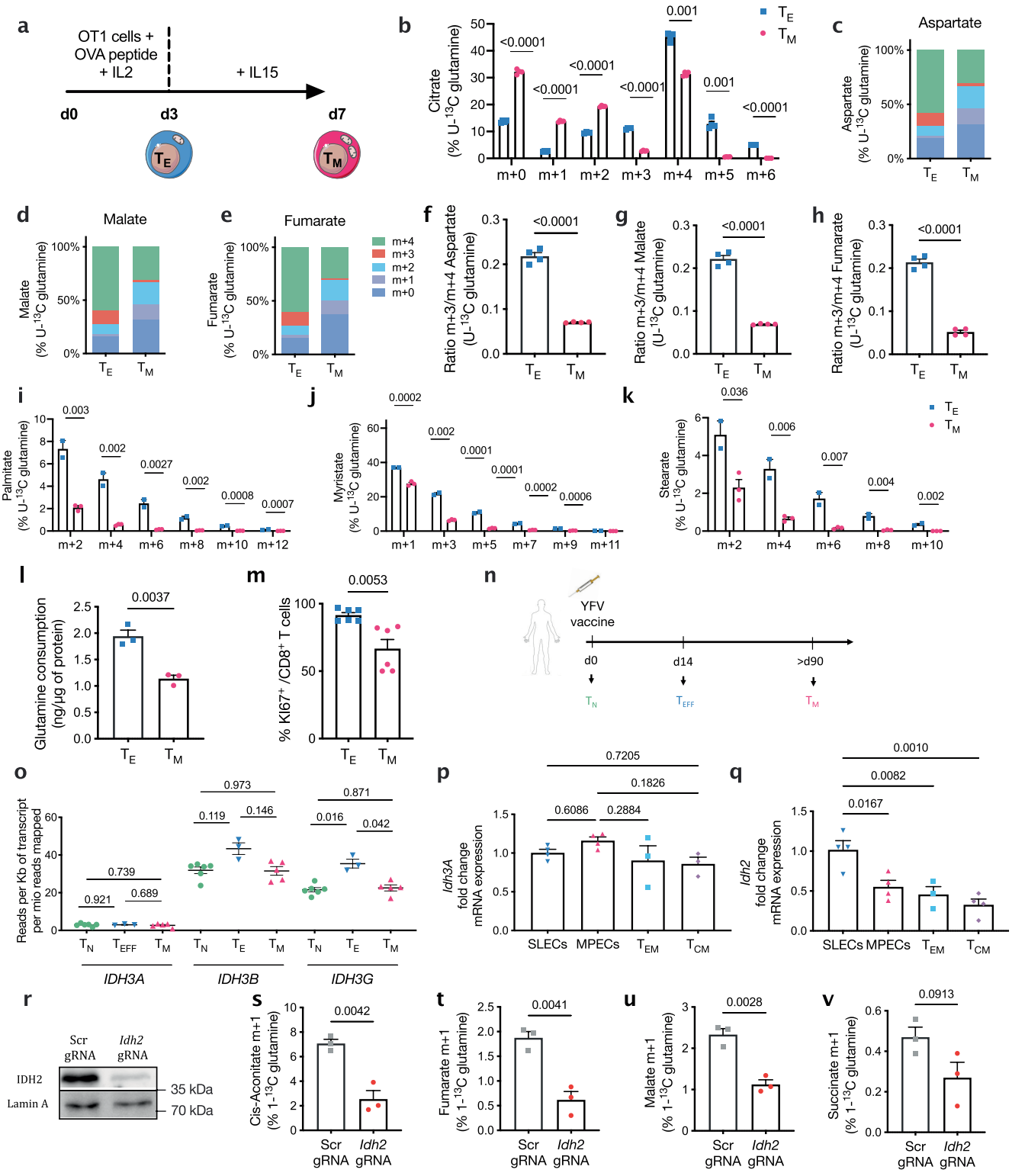

Extended Data Fig. 1 | See next page for caption.

Extended Data Fig. 1 | RC is a unique metabolic feature of rapidly proliferating T_E cells. a, Experimental set-up of expanding effector (T_E, blue) and resting memory (T_M, red) T cell differentiation. OVA-specific $CD8^+$ T cells from OT1 mice were activated with SIINFEKL (OVA) peptide and cultured with IL-2 for 3 days and with IL-15 for 4 additional days. T_E cells were collected at day 3 and T_M cells were collected at day 7 post-activation. Before collection, cells were cultured with [U-^{13}C]-glutamine for 2 h and labelling patterns were analysed by mass spectrometry. **b**, Bar graphs representing the percentages of citrate isotopologues m + 0, m + 1, m + 2, m + 3, m + 4, m + 5 and m + 6 detected by [U-^{13}C]-glutamine labelling in T_E or T_M cells. (n = 4 biological replicates per group). **c**–**e**, Percentages of aspartate (**c**), malate (**d**) and fumarate (**e**) isotopologues m + 0, m + 1, m + 2, m + 3 and m + 4 detected by [U-^{13}C]-glutamine labelling in T_E or T_M cells. **f**–**h**, Ratios of m + 3 over m + 4 isotopologues of aspartate (**f**), malate (**g**) and fumarate (**h**) detected by [U-^{13}C]-glutamine labelling in T_E and T_M cells. (n = 4 biological replicates per group). **i**–**k**, Percentage of isotopologues of palmitate (**i**), myristate (**j**) and stearate (**k**) labelling from [U-^{13}C]-glutamine in T_E or T_M cells. (n = 3 biological replicates per group (T_M cells) and n = 2 biological replicates per group (T_E cells)). **l**, Glutamine consumption in mouse $CD8^+$ T_E and T_M cells over 24 h at day 3 and day 7 post-activation respectively. (n = 3 biological replicates per group). **m**, Percentages of $KI67^+$ out of $CD8^+$ T cells in T_E and T_M cells. (n = 6 biological replicates per group, pooled data from 2 independent experiments). **n**, Experimental set-up of yellow fever vaccine administration to healthy volunteers, from which yellow fever tetramer$^+$ $CD8^+$ T cells were isolated from the blood at indicated time points. **o**, Gene expression in $CD8^+$ T cells from healthy human volunteers vaccinated with yellow fever vaccine. Shown here are *IDH3A*, *B* and *G* reads per kilobase of transcript per million reads mapped in indicated cell subsets isolated from peripheral blood. (n = 3 (T_E), n = 5 (T_M) and n = 6 (T_N) biological replicates). **p**, mRNA expression of *Idh3a* in indicated T cell subsets isolated from mouse spleens at day 7 or day 28 post-LM-OVA infection. Data are represented as fold change as compared to SLECs, normalized to β2-microglobulin expression. (n = 3 biological replicates). **q**, mRNA expression of *Idh2* in indicated T cell subsets isolated from spleens of mice at day 7 or day 28 post-LM-OVA infection. Data are represented as fold change as compared to SLECs, normalized to β2-microglobulin expression. (n = 4 biological replicates). **r**, Representative immunoblot for IDH2 in control Scr or IDH2 deleted cells. **s**–**v**, Percentage of m + 1 *cis*-aconitate (**s**), fumarate (**t**), malate (**u**) and succinate (**v**) labelling from [1-^{13}C]-glutamine in Scr or IDH2 deleted $CD8^+$ T cells. (n = 3 biological replicates per group). Data represent mean ± s.e.m. and were analysed by unpaired, two-tailed Student's *t*-test (**c**–**h**,**l**,**m**,**s**–**v**), multiple unpaired, two-tailed *t*-test (**b**,**i**–**k**) or one-way ANOVA using Tukey's multiple comparison test (**o**–**q**). Only relevant statistical comparisons are shown. For gel source data, see Supplementary Fig. 1.

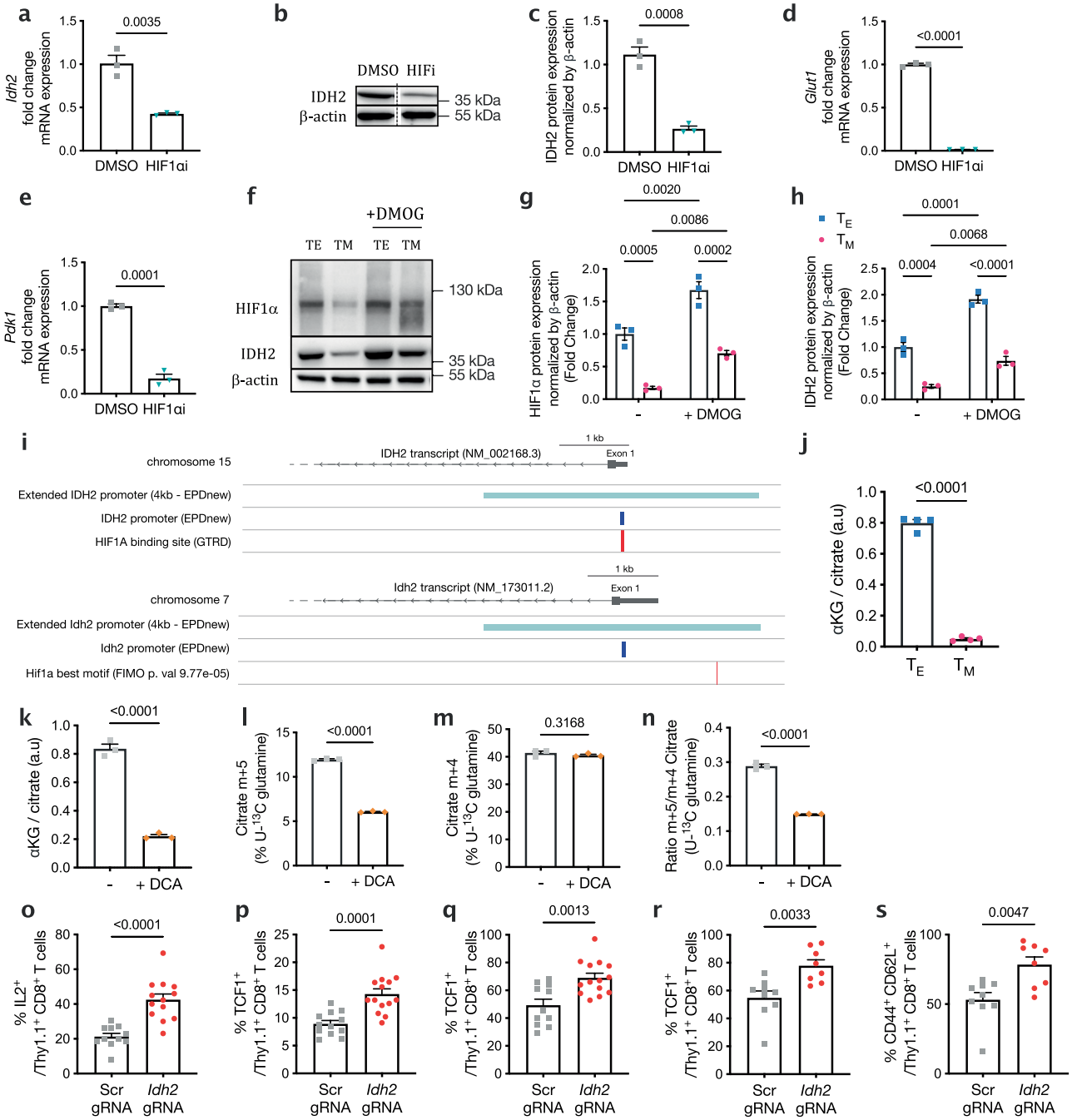

Extended Data Fig. 2 | See next page for caption.

Extended Data Fig. 2 | HIF1 drives IDH2 expression and RC in CD8$^+$ T cells. **a**, mRNA expression of *Idh2* in mouse CD8$^+$ T_E cells upon treatment with DMSO and HIF-1α inhibitor (HIF-1αi). Data are represented as fold change as compared to DMSO-treated, normalized to β2-microglobulin expression. (n = 3 biological replicates per group). **b**,**c**, Representative immunoblot (**b**) and quantification (**c**) of IDH2 in mouse CD8$^+$ T cells upon treatment with DMSO and HIF-1αi. A dashed line indicates where the immunoblot membrane was cropped (**b**) (n = 3 biological replicates per group). **d**,**e**, mRNA expression of *Glut1* (**d**) and *Pdk1* (**e**) in mouse T_E cells treated with HIF-1αi. Data are represented as fold change as compared to DMSO-treated, normalized to β2-microglobulin expression. (n = 3 biological replicates per group). **f**–**h**, Representative immunoblot (**f**) and quantification of HIF-1α (**g**) and IDH2 (**h**) in T_E or T_M cells upon treatment with control or DMOG. (n = 3 biological replicates per group). **i**, Representation of human and mouse *Idh2* transcripts, promoters and extended promoters with HIF-1α- recognized sequences highlighted in red. **j**, Ratio of α-KG over citrate in T_E or T_M cells at day 3 and day 7 post-activation respectively. (n = 4 biological replicates). **k**, Ratio of α-KG over citrate in mouse CD8$^+$ T_E cells treated with either 5 mM sodium dichloroacetate (DCA) or an equimolar sodium chloride control solution (-). (n = 3 biological replicates per group). **l**,**m**, Percentages of citrate m + 5 (**l**) and m + 4 (**m**) detected by 4 h [U-^{13}C]-glutamine labelling in mouse CD8$^+$ T_E cells treated with either 5 mM sodium dichloroacetate (DCA) or an equimolar sodium chloride control solution (-). (n = 3 biological replicates per group). **n**, Ratio of m + 5 over m + 4 isotopologues of citrate detected by [U-^{13}C]-glutamine labelling in mouse CD8$^+$ T_E cells treated with either 5 mM sodium dichloroacetate (DCA) or an equimolar sodium chloride control solution (-). (n = 3 biological replicates per group). **o**, Percentage of IL-2$^+$ cells out of transferred Thy1.1$^+$ CD8$^+$ T cells upon ex vivo restimulation at day 28 post-primary infection. **p**,**q**, Percentage of TCF1$^+$ cells out of transferred Thy1.1$^+$ CD8$^+$ T cells in the blood at day 8 (**p**) and day 28 (**q**) post-primary infection. **r**, Percentage of TCF1$^+$ cells out of transferred Thy1.1$^+$ CD8$^+$ T cells in the spleen at day 7 post-secondary challenge. **s**, Percentage of CD44$^+$CD62L$^+$ cells out of transferred Thy1.1$^+$ CD8$^+$ T cells in the spleen at day 7 post-secondary challenge. (**o**–**q**, n = 11 (Scr gRNA) and n = 13 (*Idh2* gRNA) biological replicates per group, pooled data from 3 independent experiments. **r**,**s**, n = 9 (Scr gRNA) and n = 8 (*Idh2* gRNA) biological replicates per group, pooled data from 2 independent experiments.). Data represent mean ± s.e.m. and were analysed by unpaired, two-tailed Student's *t*-test (**a**,**c**–**e**,**j**–**s**) or two-way ANOVA using the original FDR test of Benjamini and Hochberg (**h**,**i**). Only relevant statistical comparisons are shown. For gel source data, see Supplementary Fig. 1.

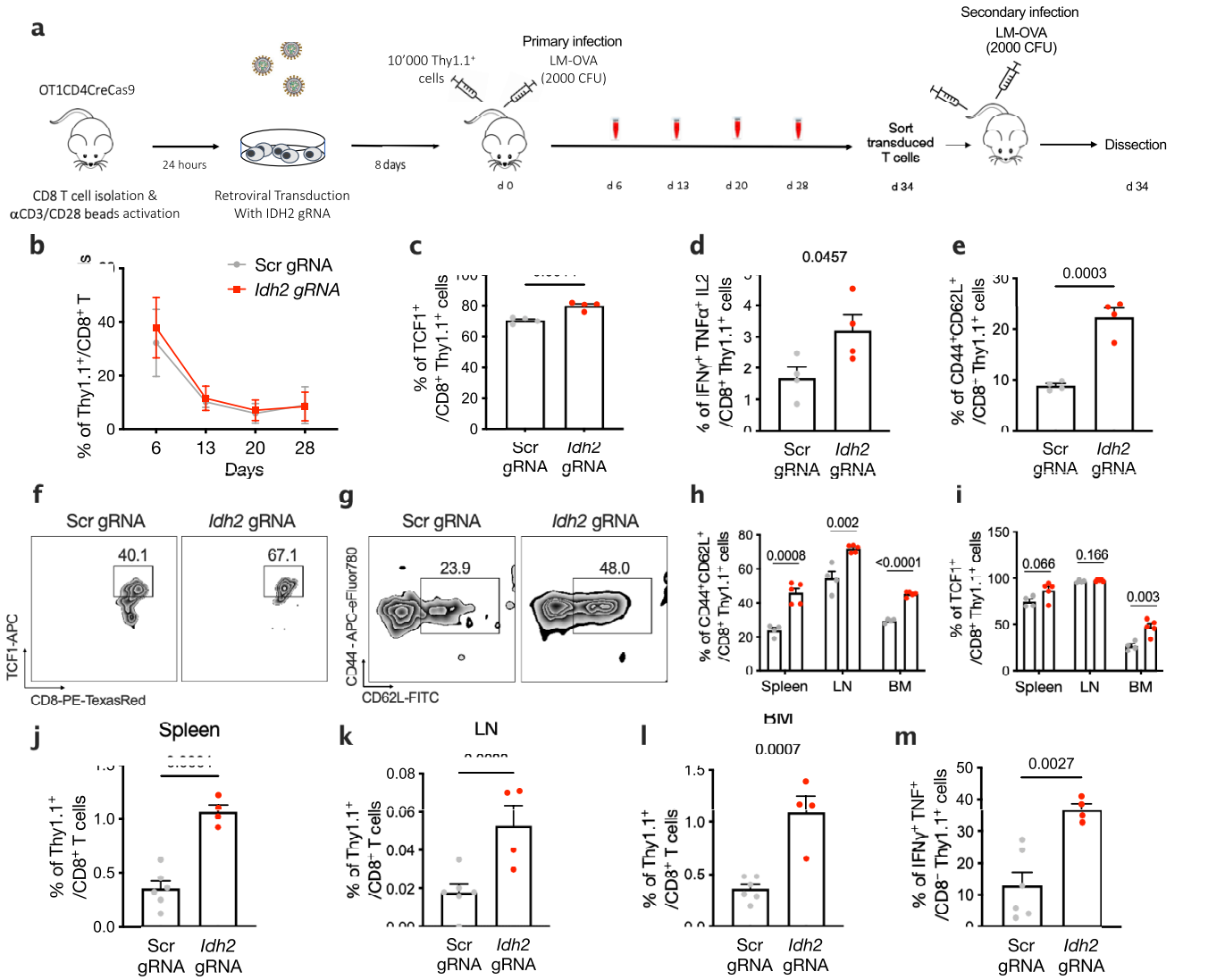

Extended Data Fig. 3 | Genetic deletion of *IDH2* promotes the differentiation of memory CD8⁺ T cells. a, Experimental set-up of OT1CD4CreCas9 CD8⁺ T cell retroviral transduction with *Idh2* gRNA or control scramble (Scr) gRNA, followed by ACT into mice that are subsequently infected with LM-OVA. 34 days post-primary infection, Thy1.1-positive cells were isolated and transferred in new hosts followed by LM-OVA infection (= secondary infection). **b**, Percentage of Thy1.1⁺ CD8⁺ out of live cells over the course of the primary infection. **c**–**e**, Percentage of TCF1⁺ (**c**), IFNγ⁺ TNF⁺ IL-2⁺ (**d**) and CD44⁺CD62L⁺ (**e**) cells out of transferred Thy1.1⁺ CD8⁺ T cells in the blood at day 28 post-primary infection. (**b**–**e**, n = 4 biological replicates per group). **f**, Representative flow cytometry graphs showing the percentage of TCF1⁺ cells out of transferred Thy1.1⁺ CD8⁺ T cells in the spleen at day 28 post-primary infection. **g**, Graphs representing the percentage of CD44⁺CD62L⁺ cells out of transferred Thy1.1⁺ CD8⁺ T cells in the spleen at day 34 post-primary infection. **h**,**i**, Percentage of CD44⁺ CD62L⁺ (**h**) and TCF1⁺ (**i**) cells out of transferred Thy1.1⁺ CD8⁺ T cells in the spleen, lymph nodes (LN) and bone marrow (BM) at day 34 post-primary infection. (**h**,**i**, n = 5 biological replicates per group). **j**–**l**, Percentage of Thy1.1⁺ cells out of CD8⁺ T cells in the spleen (**j**), lymph nodes (**k**) and bone marrow (**l**) at day 34 post-secondary infection with LM-OVA. **m**, Percentage of IFNγ⁺TNF⁺ cells out of transferred Thy1.1⁺ CD8⁺ T cells in the spleen at day 34 post-secondary infection with LM-OVA. (**j**–**m**, n = 4 (*Idh2* gRNA) and n = 6 (Scr gRNA) biological replicates per group). Data represent mean ± s.e.m. and were analysed by unpaired, two-tailed Student's *t*-test.

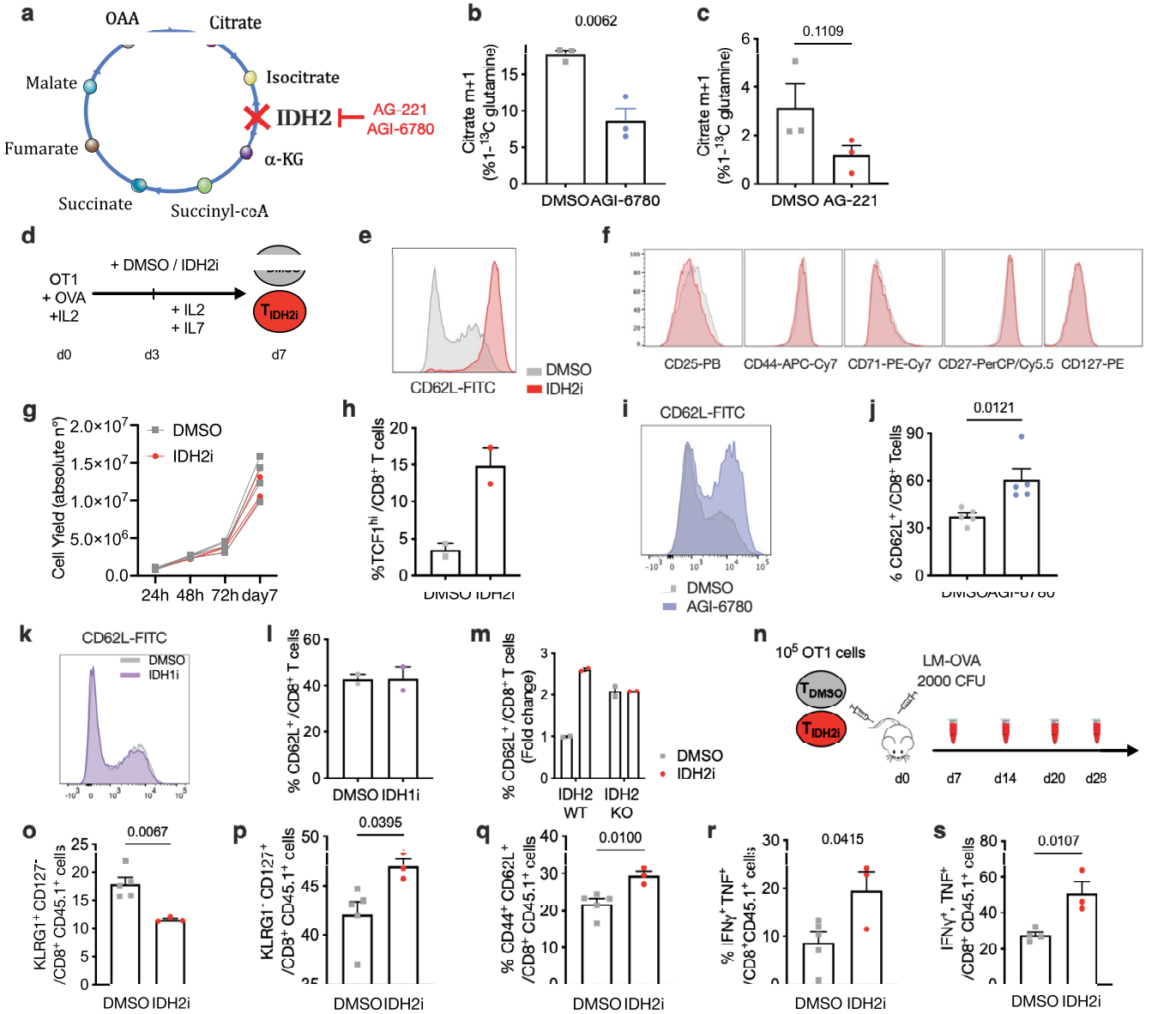

Extended Data Fig. 4 | Pharmacological inhibition of IDH2 boosts the formation of memory-like CD8⁺ T cells. a, TCA-cycle schematic with indication of two different IDH2 inhibitors. **b**,**c**, Bar graphs representing the percentage of m + 1 citrate labelling from [1-^{13}C]-glutamine in DMSO, AGI-6780-conditioned CD8⁺ T cells (**b**) or AG-221-conditioned cells (**c**). (n = 3 biological replicates per group). **d**, Experimental set-up of in vitro T cell culture. OVA-specific CD8⁺ T cells from the spleen of OT1 mice were activated with OVA and IL-2 and cultured in the presence of DMSO or IDH2i for 7 days, with IL-7 supplementation from day 3. **e**,**f**, Representative flow cytometry histograms indicating the relative expression of CD62L (**e**) and of the indicated cell-surface proteins (**f**) on the surface of CD8⁺ T cells at day 7 post-activation upon inhibition of IDH2 using AG-221 (IDH2i) or control (DMSO) treatment. **g**, Cell count at 24 h, 48 h, 72 h and 7 days post-activation of DMSO- or IDH2i-conditioned CD8⁺ T cells. (n = 4 biological replicates, data pooled from 2 independent experiments). **h**, Percentages of TCF1⁺ CD8⁺ T cells at day 7 post-activation upon DMSO or IDH2i conditioning. (n = 2 biological replicates). **i**,**j**, Representative histogram indicating the relative expression of CD62L (**i**) and bar graph showing the percentage of CD62L⁺ CD8⁺ T cells (**j**) treated with AGI-6780 at day 7 post-activation. (n = 5 biological replicates, data pooled from 4 independent experiments). **k**,**l**, Representative histogram indicating the relative expression of CD62L (**k**) and bar graph showing the percentage of CD62L⁺ CD8⁺ T cells (**l**) treated with an IDH1 inhibitor (AG-120) at day 7 post-activation. (n = 2 biological replicates, data pooled from 2 independent experiments). **m**, Percentages of CD62L⁺ CD8⁺ T cells 7 days post-activation of splenocytes from IDH2 wild-type or knockout mice cultured with or without IDH2i (n = 2 biological replicates, data pooled from 2 independent experiments). **n**, Experimental set-up of DMSO- or IDH2i-conditioned T cells transferred into mice that are subsequently infected with LM-OVA. **o**,**p**, Graphs representing the percentage of SLECs (KLRG1⁺CD127⁻) (**o**) and MPECs (KLRG1⁻CD127⁺) (**p**) out of transferred CD8⁺ T cells in the spleen at day 14 post-infection. **q**, Percentage of T_{CM} (CD44⁺CD62L⁺) cells out of transferred CD8⁺ T cells in the spleen at day 28 post-infection. **r**, Percentage of IFNγ⁺TNF⁺ cells out of transferred CD8⁺ T cells upon ex vivo restimulation at day 28 post-infection. **s**, Percentage of IFNγ⁺TNF⁺ cells out of transferred CD8⁺ T cells upon ex vivo restimulation over one year post-infection. (**n**–**q**, n = 3(IDH2i) and n = 5 (DMSO) biological replicates per group). Data represents mean ± s.e.m. and were analysed by unpaired, two-tailed Student's *t*-test (**b**,**c**,**g**,**h**,**j**,**l**,**o**–**s**) or two-way ANOVA using the original FDR test of Benjamini and Hochberg (**m**). Only relevant statistical comparisons are shown.

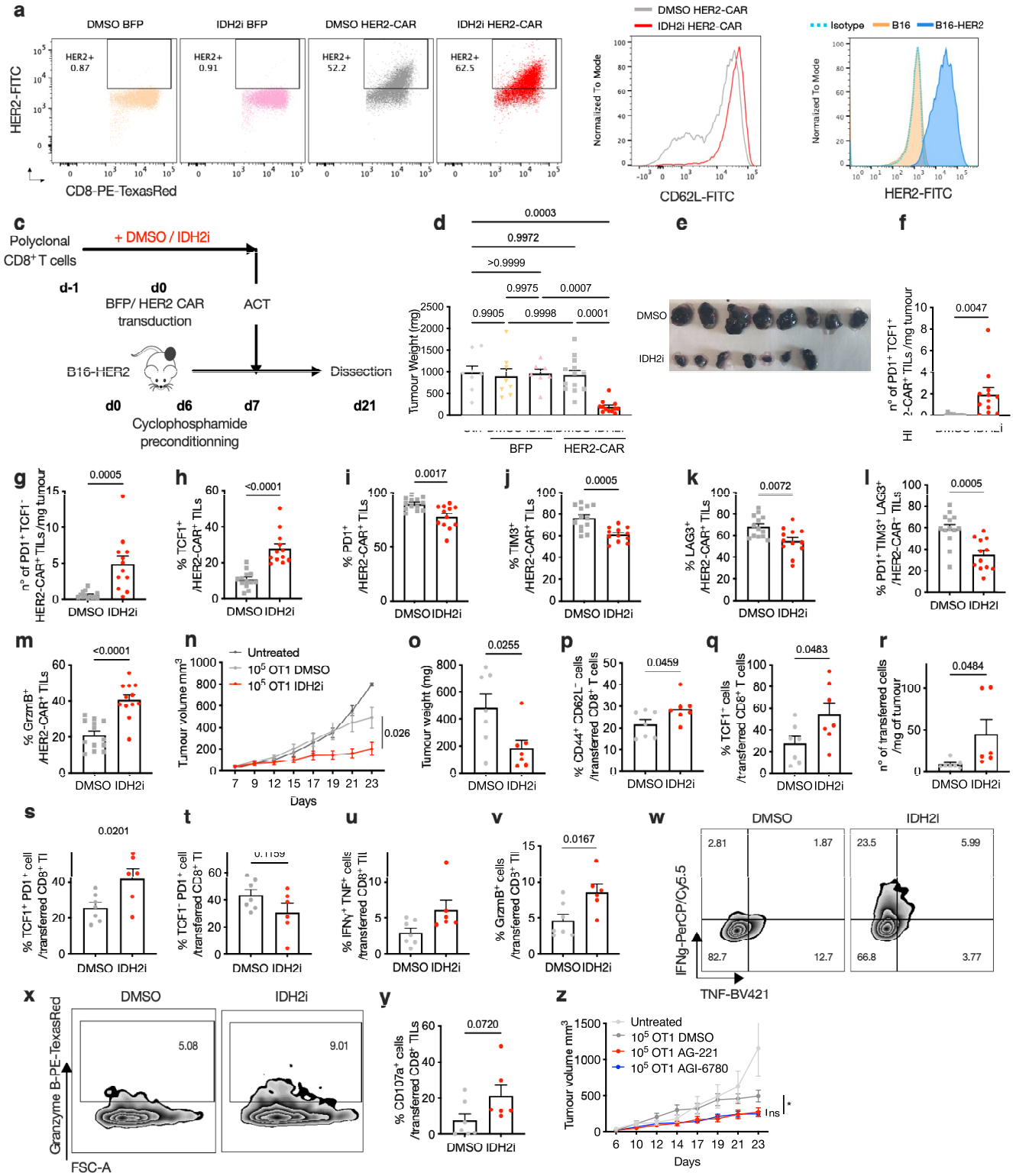

Extended Data Fig. 5 | See next page for caption.

Extended Data Fig. 5 | Pharmacological inhibition of IDH2 boosts the antitumour function of adoptively transferred cells in B16 melanoma tumor models. a, Representative dot plots of anti-HER2-CAR expression on BFP- or anti-HER2-CAR- transduced $CD8^+$ T cells and representative histogram of CD62L protein expression on the cell surface of HER2-CAR $CD8^+$ T cells treated with DMSO or IDH2i, analysed by flow cytometry at day 7 post-activation. **b**, Representative histogram of HER2 protein expression and isotype control on the cell surface of B16-HER2 tumour cells compared to B16 tumour cells, analysed by flow cytometry. **c**, Experimental set-up of B16-HER2 tumour experiment. Polyclonal $CD8^+$ T cells were transduced with blue fluorescent protein (BFP)-expressing vector or anti-HER2-CAR, expanded during 7 days in the presence of DMSO or IDH2i and subsequently transferred into B16-HER2 tumour-bearing mice. **d**,**e**, Weight (**d**) and photo (**e**) of B16-HER2 tumours from mice transferred with either DMSO or IDH2i-conditioned anti-HER2-CAR T cells. **f**,**g**, Number of transferred PD-1^+TCF1^+ cells (**f**) and PD-1^+TCF1^- cells (**g**) DMSO- or IDH2i-conditioned $CD8^+$ HER2-CAR TILs, analysed by flow cytometry 21 days post-tumour engraftment. **h**–**k**, Percentages of TCF1^+ (**h**), PD-1^+ (**i**), TIM3^+ (**j**) and LAG3^+ (**k**) cells out of transferred HER2-CAR TILs. **l**, Percentages of PD-1^+TIM3^+LAG3^+ cells out of transferred HER2-CAR TILs. **m**, Percentage of granzyme B^+ HER2-CAR^+ $CD8^+$ TILs upon ex vivo restimulation with PMA-ionomycin. (**d**–**m**, n = 13 (DMSO HER2-CAR), n = 12 (IDH2i HER2-CAR) and n = 8 (control, DMSO BFP and IDH2i BFP) biological replicates per group, pooled data from 2 independent experiments). **n**,**o**, Tumour growth curve (**n**) and weight (**o**) of B16-OVA tumour-bearing mice transferred with T cells conditioned with DMSO or IDH2i (AG-221). **p**, Percentages of $CD44^+$$CD62L^+$ cells out of transferred $CD8^+$ T cells in the spleen 23 days post-tumour engraftment. **q**, Percentages of TCF1^+ cells out of transferred $CD8^+$ T cells in the spleen 23 days post-B16-OVA tumour engraftment. **r**, Number of transferred DMSO- or IDH2i-conditioned $CD8^+$ TILs per milligram of tumour, analysed by flow cytometry 23 days post-B16-OVA tumour engraftment. **s**,**t**, Percentages of PD-1^+TCF1^+ cells (**s**) and PD-1^+TCF1^- cells (**t**) out of transferred $CD8^+$ TILs. **u**–**y**, Percentage of IFNγ and TNF (**u**), granzyme B (**v**), and CD107a (**y**) production and representative FACS plots of IFNγ and TNF (**w**) and granzyme B (**x**) production by transferred TILs upon ex vivo restimulation with OVA peptide. (**n**–**y**, n = 7 biological replicates per group). **z**, Tumour growth curve of B16-OVA tumour-bearing mice transferred with OT1 cells conditioned with DMSO, AG-221 or AGI-6780. (n = 7 biological replicates per group). Data represent mean ± s.e.m. and were analysed by unpaired, two-tailed Student's *t*-test (**f**–**v**,**y**,**z**) and one-way ANOVA using Tukey's multiple comparison test (**d**). Only relevant statistical comparisons are shown.

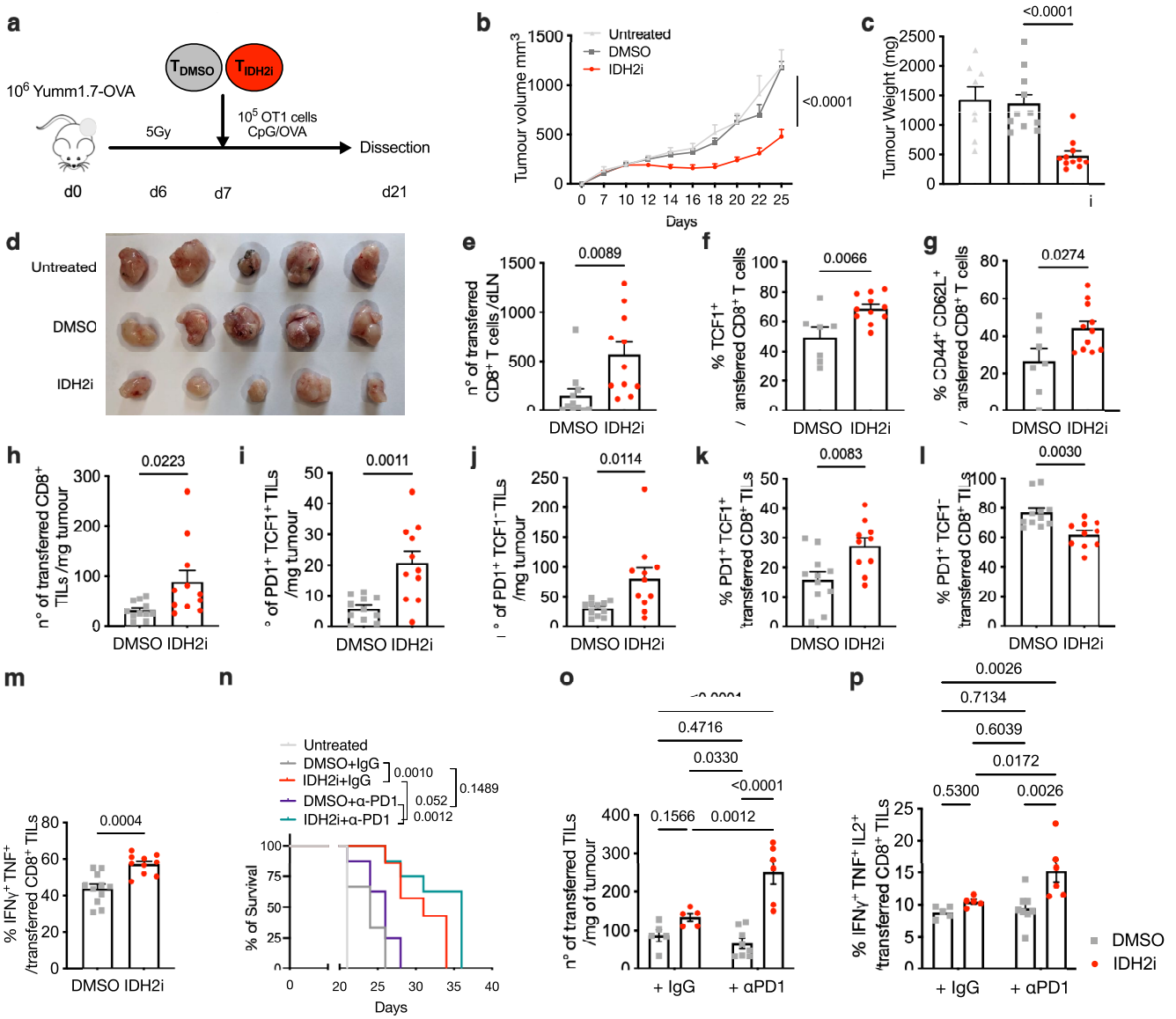

Extended Data Fig. 6 | Pharmacological inhibition of IDH2 boosts the antitumour function of adoptively transferred cells in a Yumm1.7 melanoma model. a, Experimental set-up of in vivo Yumm1.7-OVA tumour model. **b**–**d**, Tumour growth curve (**b**), weight (**c**) and representative photo (**d**) of B16-OVA tumour-bearing mice either left untreated (unt.) or transferred with T cells conditioned with DMSO or IDH2i (AG-221). **e**, Number of transferred DMSO- or IDH2i-conditioned $CD8^+$ T cells per tumour-draining lymph node, analysed by flow cytometry 25 days post-Yumm1.7-OVA tumour engraftment. **f**, Percentages of $TCF1^+$ cells out of transferred $CD8^+$ T cells in tumour-draining lymph node 25 days post-Yumm1.7-OVA tumour engraftment. **g**, Percentages of $CD44^+CD62L^+$ cells out of transferred $CD8^+$ T cells in the spleen 25 days post-tumour engraftment. **h**, Number of transferred DMSO- or IDH2i-conditioned $CD8^+$ TILs per milligram of tumour, analysed by flow cytometry 25 days post-Yumm1.7-OVA tumour engraftment. **i**,**j**, Number of transferred $PD\text{-}1^+$ $TCF1^+$ cells (**i**) and $PD\text{-}1^+TCF1^-$ cells (**j**) DMSO- or IDH2i-conditioned $CD8^+$ TILs, analysed by flow cytometry 25 days post-tumour engraftment. **k**,**l**, Percentages of $PD\text{-}1^+TCF1^+$ cells (**k**) and $PD\text{-}1^+TCF1^-$ cells (**l**) out of transferred $CD8^+$ TILs. **m**, Bar plots representing the percentage of IFNγ and TNF production by transferred TILs upon ex vivo restimulation with OVA peptide. (**b**–**m**, n = 8 (unt.), n = 11 (DMSO) and n = 10 (IDH2i) biological replicates per group, pooled data from 2 independent experiments). **n**, Survival curve of mice treated with OVA-specific $CD8^+$ T cells conditioned with DMSO or IDH2i, with α-PD-1 or IgG control combination treatment. (n = 8 biological replicates per group). **o**, Number of transferred DMSO- or IDH2i-conditioned TILs with α-PD-1 or IgG control combination treatment per milligram of tumour, analysed by flow cytometry 25 days post-Yumm1.7-OVA tumour engraftment. **p**, Percentage of $IFN\gamma^+TNF^+IL\text{-}2^+$ $CD8^+$ TILs upon ex vivo restimulation with OVA peptide. (**o**–**q**, n = 5 (DMSO+IgG and IDH2i+IgG), n = 6 (IDH2i + α-PD-1) and n = 8 (DMSO + α-PD-1) biological replicates per group). Data represent mean ± s.e.m. and were analysed by unpaired, two-tailed Student's *t*-test (**b**,**e**–**m**), one-way ANOVA using Tukey's multiple comparison test (**c**), two-way ANOVA corrected for multiple testing by the original FDR of Benjamini and Hochberg (**o**,**p**) or log-rank test (**n**). Only relevant statistical comparisons are shown.

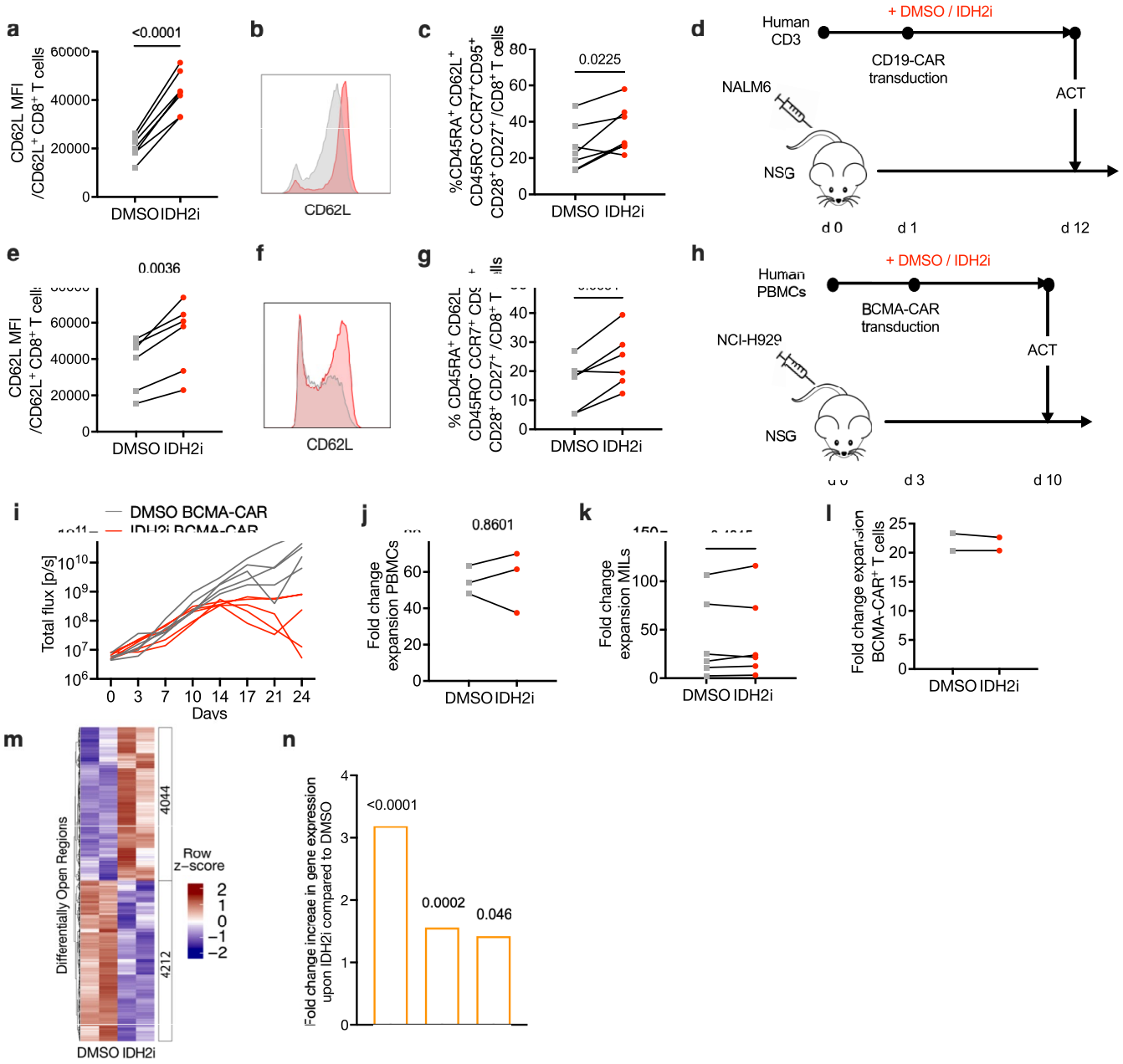

Extended Data Fig. 7 | Inhibition of IDH2 induces memory features in human T cells. a,**b**, MFI of CD62L (**a**) and representative histogram (**b**) at day 9 post-activation on the surface of human CD8$^+$ T cells isolated from healthy volunteer PBMCs, measured by flow cytometry. PBMCs from healthy donors were activated with anti-CD3/CD28 beads for 5 days and cultured 4 additional days prior phenotypic analyses. The cells were cultured in the presence of DMSO or IDH2i during the entire experiment (**a**–**c**). (n = 7 donors, pooled data from 2 independent experiments). **c**, Percentages of human CD8$^+$ T_{SCM}-like cells, characterized as CD45RA$^+$, CD62L$^+$, CD45RO$^-$, CCR7$^+$, CD95$^+$, CD28$^+$, CD27$^+$. (n = 7 donors, pooled data from 2 independent experiments). **d**, Experimental set-up of NAML6 tumour experiment. Human T cells were transduced with anti-CD19 CAR T cells, expanded during 12 days in the presence of DMSO or IDH2i and subsequently transferred into tumour-bearing NSG mice. **e**–**g**, Human MILs from patients with multiple myeloma were activated with anti-CD3/CD28 beads for 5 days and cultured 4 additional days prior phenotypic analyses. The cells were cultured in the presence of DMSO or IDH2i during the entire experiment. Shown here is MFI of CD62L (**e**) and representative histogram (**f**), and percentage of T_{SCM} (**g**) at day 9 post-activation in human CD8$^+$ MILs. (n = 6 donors, pooled data from 2 independent experiments). **h**, Experimental set-up of NCI-H929 tumour experiment. Human T cells were transduced with anti-BCMA CAR T cells, expanded during 10 days in the presence of DMSO or IDH2i and subsequently transferred into tumour-bearing NSG mice. **i**, BLI quantification of total flux (p/s) (representative of 2 independent experiments). **j**–**l**, Fold-change expansion at day 9 post-activation of human PBMCs (**j**), human MILs (**k**) and human CAR T cells (**l**) cultured with DMSO or IDH2i. (n = 3 (j), n = 6 (**k**) and n = 2 donors (**l**), pooled data from 2 independent experiments (**k**). **m**, Representation (row z-scores) of differentially accessible regions in mouse CD8$^+$ T cells after DMSO or IDH2i conditioning (ATAC-seq). **n**, Bar plots representing $\log_2$ fold change in mRNA expression of *Sell*, *Tcf7* and *Ccr7* upon IDH2i-compared to DMSO-conditioned CD8$^+$ T cells (RNA-seq). Data represent mean ± s.e.m. and were analysed by paired two-tailed Student's *t*-test (**a**,**c**,**e**,**g**,**j**–**m**).

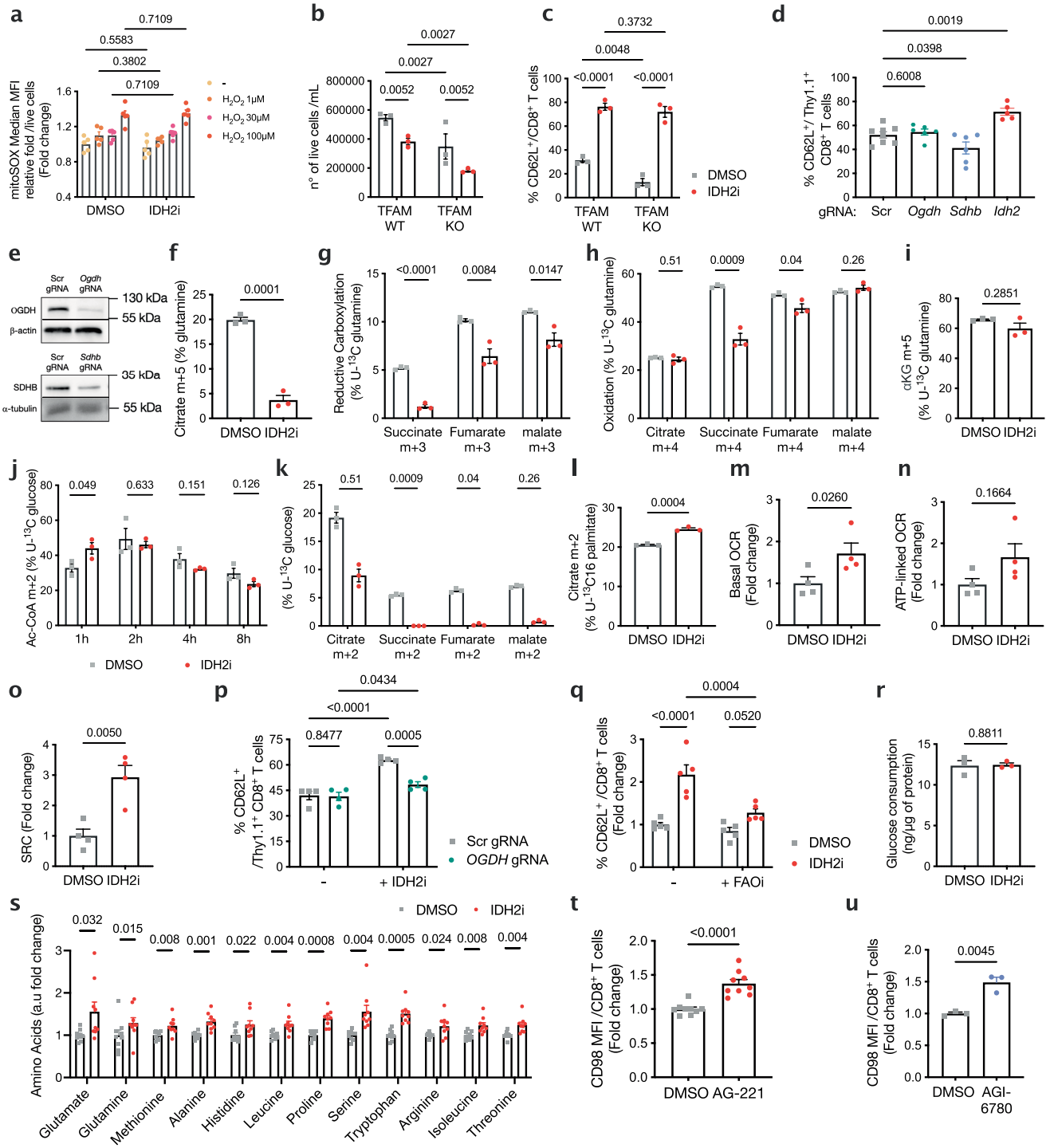

Extended Data Fig. 8 | See next page for caption.

Extended Data Fig. 8 | Inhibition of IDH2 induces metabolic compensation. **a**, MitoSOX MFI in DMSO- or IDH2i-treated cells upon addition of H_2O_2 at indicated concentrations, measured by flow cytometry. (n = 5 biological replicates, pooled data from 2 independent experiments). **b**, Number of live TFAM WT and TFAM KO T cells per millilitre upon DMSO or IDH2i treatment. (n = 3 biological replicates, pooled data from 2 independent experiments). **c**, Percentage of $CD62L^+$ out of $CD8^+$ TFAM WT and KO T cells upon DMSO or IDH2i treatment. (n = 3 biological replicates, pooled data from 2 independent experiments). **d**, Percentage of $CD62L^+$ out of $Thy1.1^+$ $CD8^+$ T cells at day 7 post-activation upon deletion of indicated genes. (n = 6 (Scr, *Ogdh* and *Sdhb*) and n = 5 (*Idh2*) biological replicates per group, pooled data from 3 independent experiments). **e**, Immunoblots for OGDH and SDHB in control Scr and OGDH- or SDHB-deleted cells. (Representative of 2 independent experiments). **f**, Percentages of citrate m + 5 detected by [U-^{13}C]-glutamine labelling in DMSO or IDH2i-treated T cells. (n = 3 biological replicates per group). **g**, Percentages of m + 3 succinate, fumarate and malate detected by 2 h [U-^{13}C]-glutamine labelling in DMSO or IDH2i-treated T cells. (n = 3 biological replicates per group). **h**, Percentages of m + 4 succinate, fumarate and malate detected by 2 h [U-^{13}C]-glutamine labelling in DMSO or IDH2i-treated T cells. (n = 3 biological replicates per group). **i**, Percentages of m + 5 α-KG detected by 2 h [U-^{13}C]-glutamine labelling in DMSO or IDH2i-treated T cells. (n = 3 biological replicates per group). **j**, Percentages of m + 2 acetyl-CoA, detected by [U-^{13}C]-glucose labelling for indicated time in DMSO or IDH2i-treated T cells. (n = 3 biological replicates per group). **k**, Percentages of m + 2 citrate, succinate, fumarate and malate detected by 2 h [U-^{13}C]-glucose labelling in DMSO or IDH2i-treated T cells. (n = 3 biological replicates per group). **l**, Percentages of citrate m + 2 detected by [U-$^{13}C_{16}$]-palmitate labelling in mouse $CD8^+$ T cells treated with DMSO or the IDH2 inhibitor (IDH2i). (n = 3 biological replicates per group). **m**–**o**, Quantification of basal OCR (**m**), ATP-linked OCR (**n**) and spare respiratory capacity (SRC; **o**) from data presented in Fig. 4d. (n = 4 biological replicates, pooled data from 2 independent experiments). **p**, Percentage of $CD62L^+$ T cells in control Scr or OGDH-deleted $CD8^+$ T cells, treated with IDH2i. (n = 4 biological replicates, pooled data from 2 independent experiments). **q**, Percentage of $CD62L^+$ T cells in DMSO or IDH2i-conditioned $CD8^+$ T cells, treated with etomoxir (FAOi). (n = 5 biological replicates, pooled data from 2 independent experiments). **r**, Glucose consumption in DMSO- or IDH2i-treated mouse $CD8^+$ T cells over 24 h, at day 3 post-activation. (n = 3 biological replicates per group). **s**, Intracellular abundances of indicated amino acids (arbitrary units, a.u) measured by mass spectrometry upon DMSO or IDH2i treatment. (n = 9 biological replicates, pooled data from 3 independent experiments). **t**,**u**, CD98 MFI in DMSO- or AG-221- (**t**) or AGI-6780- (**u**) treated $CD8^+$ T cells, measured by flow cytometry at day 3 post-activation. (n = 9 (AG-221) and n = 3 (AGI-6780) biological replicates, pooled data from 4 (AG-221) and 2 (AGI-6780) independent experiments). Data represent mean ± s.e.m. and were analysed by unpaired two-tailed Student's *t*-test (**f**,**i**,**l**–**o**,**r**,**t**,**u**), multiple unpaired, two-tailed *t*-tests using Benjamini and Hochberg method (**g**,**h**,**j**,**k**,**s**), one-way ANOVA using Tukey's multiple comparison test (**d**) or two-way ANOVA using the original FDR test of Benjamini and Hochberg (**a**–**c**,**p**,**q**). Only relevant statistical comparisons are shown. For gel source data, see Supplementary Fig. 1.

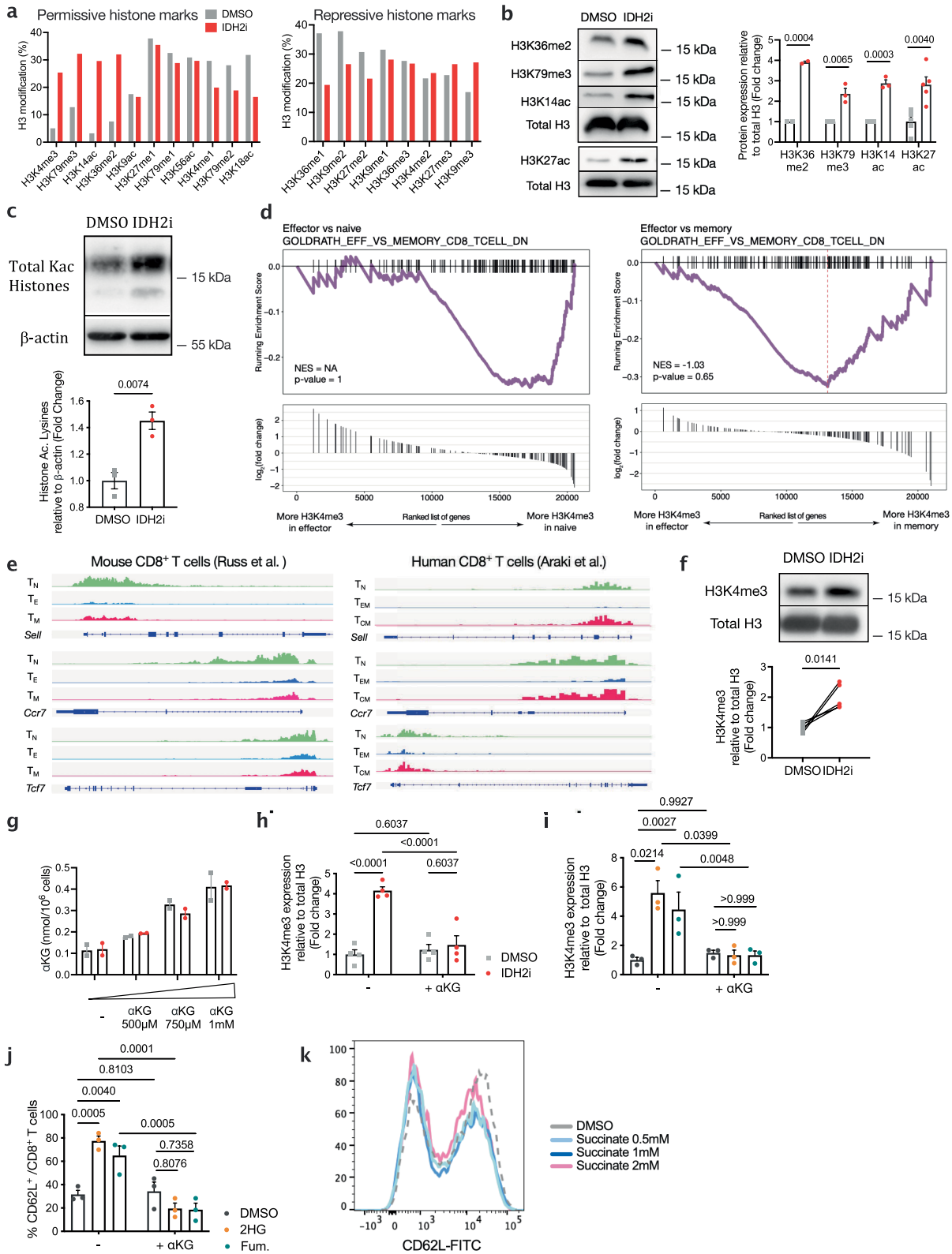

Extended Data Fig. 9 | See next page for caption.

Extended Data Fig. 9 | Inhibition of IDH2 leaves an epigenetic imprint. a, Bar graphs representing permissive and repressive histone marks in DMSO or IDH2i-conditioned CD8$^+$ T cells. **b**, Immunoblot and quantification of indicated histone marks in DMSO or IDH2i-conditioned CD8$^+$ T cells. (n = 2 (H3K36me2), pooled from 2 independent experiments, n = 3 (H3K79me3, H3K14ac) and n = 5 (H3K27ac) biological replicates, pooled data from 3 independent experiments). **c**, Immunoblot and quantification of total acetylated lysines in DMSO or IDH2i-conditioned CD8$^+$ T cells. (n = 3 biological replicates, data representing 2 independent experiments). **d**, Barcode plots representing gene set enrichment analysis of a memory signature on H3K4me3-enriched regions in OT1 cells. NES, normalized enrichment score; Running ES, running enrichment score. **e**, H3K4me3 ChIP–seq tracks at *Sell*, *Ccr7* and *Tcf7* loci from mouse naive (T_N, green), effector (T_E, blue) and memory (T_M, pink) OT1 cells and from human naive (T_N, green), effector memory (T_{EM}, blue) and central memory (T_{CM}, pink) CD8$^+$ T cells from the peripheral blood of healthy adults. **f**, Immunoblot and quantification of H3K4me3 histone mark in DMSO- or IDH2i-conditioned MILs. (n = 5 biological replicates, pooled data from 2 independent experiments). **g**, Intracellular abundance of α-KG in DMSO or IDH2i-conditioned CD8$^+$ T cells, supplemented with indicated doses of cell-permeable α-KG (n = 2 biological replicates). **h**, Immunoblot quantification of H3K4me3 in DMSO or IDH2i-conditioned CD8$^+$ T cells, supplemented with α-KG. (n = 4 biological replicates, pooled data from 4 independent experiments). **i**, Immunoblot quantification of H3K4me3 in T cells treated with DMSO, fumarate or 2-HG. **j**, Percentage of CD62L$^+$ T cells upon DMSO, fumarate or *S*-2-HG treatment and α-KG supplementation. (**i**,**j**, 3 biological replicates, pooled data from 3 independent experiments). **k**, Representative histogram indicating the relative expression of CD62L on the surface of CD8$^+$ T cells treated with 0.5, 1 or 2 mM succinate (dimethyl succinate, Sigma-Aldrich) at day 7 post-activation. Data represent mean ± s.e.m. and were analysed by unpaired (**c**,**i**,**j**) or paired (**d**) two-tailed Student's *t*-test or two-way ANOVA using the original FDR test of Benjamini and Hochberg (**e**–**h**,**k**). Only relevant statistical comparisons are shown. For gel source data, see Supplementary Fig. 1.

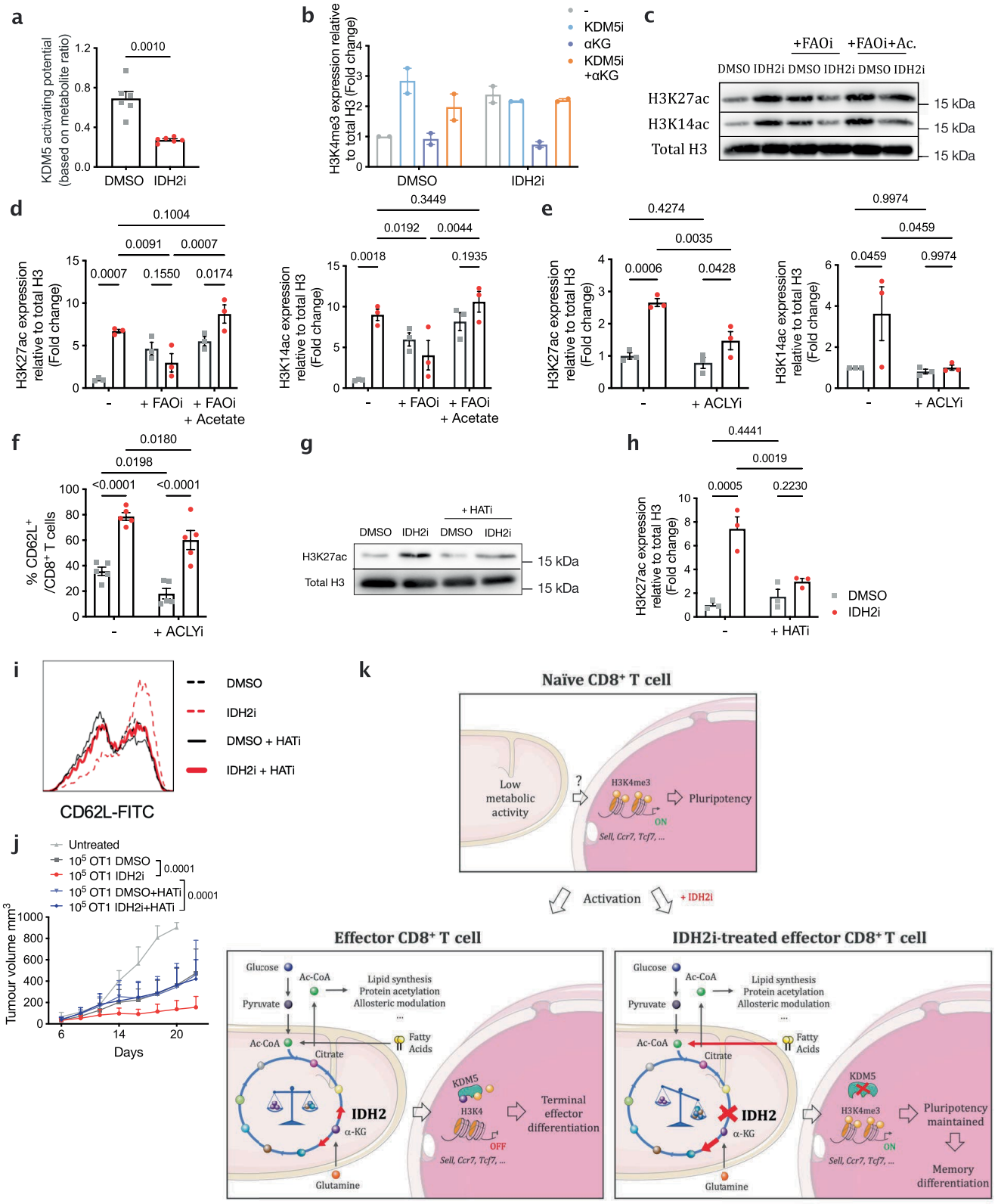

Extended Data Fig. 10 | See next page for caption.

Extended Data Fig. 10 | Compensatory metabolism upon IDH2 inhibition influences histone modification and memory T cell differentiation. a, KDM5 activating potential represented by the ratio of fold increase in K_m value for α-KG versus the sum of fold increased IC_{50} concentrations of inhibitory metabolites (2-HG, succinate, fumarate and malate), calculated as: (concentration α-KG/K_m α-KG)/((concentration 2-HG/IC_{50} 2-HG) + (concentration succinate/IC_{50} succinate) + (concentration fumarate/IC_{50} fumarate) + (concentration malate/IC_{50} malate)). Ratio based on cellular metabolite concentrations calculated from absolute metabolite quantifications. (n = 6 biological replicates, pooled data from 2 independent experiments). **b**, Immunoblot quantification of H3K4me3 in DMSO- and IDH2i-treated $CD8^+$ T cells, supplemented with α-KG and/or KDM5 inhibitor. (n = 2 biological replicates, pooled data from 2 independent experiments). **c**,**d**, Immunoblot (**c**) and quantifications (**d**) of H3K27ac and H3K14ac in DMSO or IDH2i-conditioned $CD8^+$ T cells, treated with etomoxir (FAOi) and supplemented with acetate. (n = 3 biological replicates). **e**, Immunoblot quantification of H3K27ac and H3K14ac in DMSO or IDH2i-conditioned $CD8^+$ T cells, treated with ACLYi. (n = 3 biological replicates). **f**, Percentage of $CD62L^+$ T cells in DMSO or IDH2i-conditioned $CD8^+$ T cells, treated with ACLYi. (n = 5 biological replicates, pooled data from 2 independent experiments). **g**,**h**, Immunoblot (**g**) and quantification (**h**) of H3K27ac in DMSO, IDH2i-, DMSO+HATi-and IDH2i+HATi-conditioned $CD8^+$ T cells. (n = 3 biological replicates, pooled data from 3 independent experiments). **i**, CD62L expression in DMSO, IDH2i-, DMSO+HATi- and IDH2i+HATi-conditioned cells. (HATi = histone acetyltranferase p300/CBP inhibitor, 8 μM C646). (Representative blot and histogram from 3 independent experiments with 3 biological replicates). **j**, Tumour growth curve of B16-OVA tumours from mice treated with either DMSO, IDH2i-, DMSO+HATi- or IDH2i+HATi-conditioned OVA-specific $CD8^+$ T cells. (n = 13 (IDH2i), n = 14 (DMSO+HATi, IDH2i+HATi) and n = 15 (DMSO) biological replicates per group, pooled data from 2 independent experiments). **k**, Pluripotent naive $CD8^+$ T cells are characterized by low metabolic activity and permissive H3K4me3 deposition at pro-memory genes, including *Sell*, *Ccr7* and *Tcf7*. After activation, T_E cells increase glutamine metabolism along both the oxidative and reductive pathways (represented by two red arrows on the left panel of the figure). RC generates citrate and acetyl-CoA, which is a key metabolite supporting cell growth and function. This specific T_E cell metabolism creates a unique metabolite composition (represented by balanced levels of α-KG on one side and succinate, fumarate, malate and 2-HG on the other side) enabling the activity of the α-KG-dependent histone demethylase KDM5. KDM5-mediated demethylation of H3K4me3 in activated T cells induces a repressive chromatin state at pro-memory genes, which prevents the maintenance of pluripotency and facilitates terminal effector differentiation. Blocking RC through inhibition of IDH2 does not hinder T cell proliferation and function, as compensatory fatty acid oxidation can refuel acetyl-CoA pools, with the support of glutamine anaplerosis, which is now redirected entirely in the oxidative branch of the TCA cycle (represented by the larger red arrow on the right panel of the figure), altogether enhancing cellular OCR. This leads to a perturbation of the metabolite balance by increasing the levels of the TCA intermediates succinate, fumarate, malate and 2-HG (represented by a shift in the balance upon IDH2 inhibition). The accumulation of these inhibitory metabolites impairs KDM5 demethylase activity, and elevated H3K4me3 is likely to foster a permissive chromatin state at pro-memory genes, allowing for the maintenance of pluripotency and memory differentiation. Data represent mean ± s.e.m. and were analysed by unpaired two-tailed Students *t*-test (**a**,**j**) or two-way ANOVA using the original FDR test of Benjamini and Hochberg (**b**,**d**–**f**,**h**). Only relevant statistical comparisons are shown. For gel source data, see Supplementary Fig. 1.

nature portfolio

Corresponding author(s): Mathias Wenes, Pedro Romero, Ping-Chih Ho

Last updated by author(s): Jul 17, 2023

Reporting Summary

Nature Portfolio wishes to improve the reproducibility of the work that we publish. This form provides structure for consistency and transparency in reporting. For further information on Nature Portfolio policies, see our Editorial Policies and the Editorial Policy Checklist.

Statistics

For all statistical analyses, confirm that the following items are present in the figure legend, table legend, main text, or Methods section.

n/a	Confirmed
☐	☒ The exact sample size (*n*) for each experimental group/condition, given as a discrete number and unit of measurement
☐	☒ A statement on whether measurements were taken from distinct samples or whether the same sample was measured repeatedly
☐	☒ The statistical test(s) used AND whether they are one- or two-sided *Only common tests should be described solely by name; describe more complex techniques in the Methods section.*
☒	☐ A description of all covariates tested
☐	☒ A description of any assumptions or corrections, such as tests of normality and adjustment for multiple comparisons
☐	☒ A full description of the statistical parameters including central tendency (e.g. means) or other basic estimates (e.g. regression coefficient) AND variation (e.g. standard deviation) or associated estimates of uncertainty (e.g. confidence intervals)
☐	☒ For null hypothesis testing, the test statistic (e.g. *F*, *t*, *r*) with confidence intervals, effect sizes, degrees of freedom and *P* value noted *Give P values as exact values whenever suitable.*
☒	☐ For Bayesian analysis, information on the choice of priors and Markov chain Monte Carlo settings
☒	☐ For hierarchical and complex designs, identification of the appropriate level for tests and full reporting of outcomes
☒	☐ Estimates of effect sizes (e.g. Cohen's *d*, Pearson's *r*), indicating how they were calculated

Our web collection on statistics for biologists contains articles on many of the points above.

Software and code

Policy information about availability of computer code

Data collection	BD FACSDiva software (version 8.0.1) Xcalibur software for metabolomics data
Data analysis	GraphPad Prism 9.0 for graphs and statistical analyses Flowjo v10.8.1 for flow cytometry analyses ImageJ 2.1.0/1.53c for immunoblot analyses R (v.3.5.3) For metabolomics: El-Maven and Polly (Elucidata) For published RNA seq data: limma package (v. 3.38.3) biomaRt (v. 2.38.0) edgeR package (v. 3.24.3) For Binding motif analyses: Integrative Genomics Viewer (IGV v. 2.8.0; Homo sapiens hg38) MEME Suite (v 5.3.2) IGV (Mus musculus mm10) For RNA seq data: bcl2fastq2 Conversion Software (version 2.20, Illumina) bcbio-nextgen pipeline (v. 20.11)

Atropos (v. 1.1.28)
hisat2 (v. 2.2.1)
HTSeq (v. 0.9.1)
limma package (v. 3.38.3)
clusterProfiler package (v. 4.0.5) for R (v.4.1.0)
Enrichr software

For ATAC seq data:
AdapterRemoval (v. 2.1.7)
bcbio-nextgen pipeline (v. 19.03)
Atropos (v. 1.1.21)
bwa (v. 0.7.17-r1188)
MACS2 (v. 2.1.1.20160309)
DiffBind package (v. 2.10.0)
ChIPpeakAnno package (v. 3.16.1)
Homer (v. 4.11.1)

For bioluminescence imaging and analysis:
Xenogen in vivo imaging system (IVIS) (Caliper Life Sciences)
Living Image software (version 4.7.3, 64bit)

For manuscripts utilizing custom algorithms or software that are central to the research but not yet described in published literature, software must be made available to editors and reviewers. We strongly encourage code deposition in a community repository (e.g. GitHub). See the Nature Portfolio guidelines for submitting code & software for further information.

Data

Policy information about availability of data

All manuscripts must include a data availability statement. This statement should provide the following information, where applicable:

- Accession codes, unique identifiers, or web links for publicly available datasets
- A description of any restrictions on data availability
- For clinical datasets or third party data, please ensure that the statement adheres to our policy

RNA-seq data is available in the Gene Expression Omnibus database under the accession code (GSE192395). ATAC-seq data is available in the Gene Expression Omnibus database under the accession code (GSE192394).

Field-specific reporting

Please select the one below that is the best fit for your research. If you are not sure, read the appropriate sections before making your selection.

☒ Life sciences ☐ Behavioural & social sciences ☐ Ecological, evolutionary & environmental sciences

For a reference copy of the document with all sections, see nature.com/documents/nr-reporting-summary-flat.pdf

Life sciences study design

All studies must disclose on these points even when the disclosure is negative.

Sample size	Previous experience allowed to estimate sample size (Wenes et al, Cell Metabolism 2022 (PMID: 35452600).
Data exclusions	Graft rejection or death led to the exclusion of some mice from analyses. Samples were excluded from flow cytometric analyses when the number of events recorded was lower than 20 in the population of interest, preventing accurate analyses.
Replication	In general, the experiments have been performed independently two to three times and have been pooled and attempts at replication were successful.
Randomization	Animals and in vitro experimental groups were randomly assigned to different treatment groups.
Blinding	For in vivo experiments, following randomization, treatment groups were known. For all studies, blinding was not relevant because of objective read-outs.

Reporting for specific materials, systems and methods

We require information from authors about some types of materials, experimental systems and methods used in many studies. Here, indicate whether each material, system or method listed is relevant to your study. If you are not sure if a list item applies to your research, read the appropriate section before selecting a response.

Materials & experimental systems

n/a	Involved in the study
☐	☒ Antibodies
☐	☒ Eukaryotic cell lines
☒	☐ Palaeontology and archaeology
☐	☒ Animals and other organisms
☐	☒ Human research participants
☒	☐ Clinical data
☒	☐ Dual use research of concern

Methods

n/a	Involved in the study
☒	☐ ChIP-seq
☐	☒ Flow cytometry
☒	☐ MRI-based neuroimaging

Antibodies

Antibodies used

The following antibodies were used in western blotting analysis:
Recombinant Anti-IDH2 antibody [EPR7577] Rabbit mAb, Abcam ab131263, 1:500
IDH2 antibody [GT673] mouse mAb, GeneTex GTX628487, 1:500
Tri-Methyl-Histone H3 (Lys4) (C42D8) Rabbit mAb, Cell Signaling 9751, 1:2000
Tri-Methyl-Histone H3 (Lys27) (C36B11) Rabbit mAb, Cell Signaling 9733, 1:2000
Acetyl-Histone H3 (Lys27) Rabbit mAb, Cell Signaling 8173, 1:2000
Tri-Methyl-Histone H3 (Lys79) Antibody, Cell Signaling 4260, 1:2000
Di-Methyl-Histone H3 (Lys36) (C75H12) Rabbit mAb, Cell Signaling 2901, 1:2000
Acetyl-Histone H3 (Lys14) (D4B9) Rabbit mAb, Cell Signaling 7627, 1:500
Histone H3 Antibody, Cell Signaling 9715, 1:5000
Lamin A + C antibody, GeneTex GTX101126, 1:1000
HIF-1α (C-Term) Polyclonal Antibody, 10006421, Cayman Chemical, 1:200
Acetylated lysine antibody 9441S Cell Signaling, 1:1000
Recombinant Anti-Aconitase 2 antibody [EPR8282(B)] ab129069 Abcam, 1:1000
Anti-SDHB antibody (G-10), sc-271548 Santa Cruz, 1:1000
Anti-OGDH Antibody GTX33374 Genetex, 1:1000

The following antibodies were used in flow cytometry analysis:
recombinant human Fc-tagged Her2/ErbB2 protein, Sino Biological, 1:200
anti-human-Fc Alexa Fluor 488 conjugate, Thermo Fisher Scientific, 1:500
anti-mouse CD62L FITC, MEL-14, Thermo Fisher Scientific, 1:1000
anti-mouse CD127 PE, SB/199, Biolegend, 1:200
anti-mouse CD44 APC-eFluor 780, IM7, Thermo Fisher Scientific, 1:200
anti-mouse KLRG1 PE/Cyanine7, MAFA, Biolegend, 1:200
anti-mouse TCF7, C63D9, Cell Signaling, 1:200
anti-mouse Thy1.1 (CD90.1) PE, OX-7, Biolegend, 1:500
anti-mouse IL2 BV711, JES6-5H4, Biolegend, 1:200
anti-mouse IFNg PerCP/Cyanine5.5, XMG1.2, Biolegend, 1:200
anti-mouse TNFa Brilliant Violet 421, MP6-XT22, Biolegend, 1:200
anti-mouse PD1 (CD279) PerCP/Cyanine5.5, RMP1-30, Biolegend, 1:300
anti-mouse TIM3 (CD366) Brilliant Violet 421, RMT3-23, Biolegend, 1:200
anti-mouse LAG3 PE, C9B7W, Biolegend, 1:200
anti-mouse CD45.1 PerCP/Cyanine5.5, A20, Biolegend, 1:200
anti-mouse CD45.2 FITC, 104, Biolegend, 1:200
anti-human CD107a (LAMP-1) PE, H4A3, BD, 1:100
anti-granzyme B, PE-texas red, GB11, Invitrogen, 1:200
anti-mouse CD71, PE-Cy7, RI7217, Biolegend, 1:200
anti-mouse CD25, Pacific blue, PC61, Biolegend, 1:200
anti-mouse CD27, PerCP/Cyanine5.5, LG.3A10, 1:200
anti-human CD3 BV711, UCHT1, Biolegend, 1:200
anti-human CD8 BV421, SK1, Biolegend, 1:200
anti-human CD45RA BUV395, HI100, BD, 1:200
anti-human CD45RO BUV805, UCHL1, BD, 1:200
anti-human CD62L PerCP/Cyanine5.5, DREG-56, Biolegend, 1:200
anti-human CCR7 (CD197) Pacific Blue, G043H7, Biolegend, 1:100
anti-human CD95 PE, DX2, BD, Thermo Fisher Scientific, 1:200
anti-human CD27 BV605, LG.3A10, Biolegend, 1:200
anti-human CD28 PE/Cyanine7, S20013B, Biolegend, 1:100
anti-human CD271 APC, ME20.4, Biolegend, 1:200
anti-human HER2 (CD340) Brilliant Violet 421, 24D2, Biolegend, 1:500
Live/dead fixable Aqua Dead cell stain kit, Lifetechnologies, 1:1000
MitoSOX Red Mitochondrial Superoxide Indicator M36008 Invitrogen, 1:1000
BODIPY 493/503 (4,4-Difluoro-1,3,5,7,8-Pentamethyl-4-Bora-3a,4a-Diaza-s-Indacene, D3922 Thermofisher, 1:5000
Filipin III, SAE0087 Sigma-Aldrich, 1:100

Validation:
Recombinant Anti-IDH2 antibody [EPR7577] Rabbit mAb, Abcam ab131263, 1:500
https://www.abcam.com/products/primary-antibodies/idh2-antibody-epr7577-ab131263.html

IDH2 antibody [GT673] mouse mAb, GeneTex GTX628487, 1:500
https://www.genetex.com/Product/Detail/IDH2-antibody-GT673/GTX628487
Tri-Methyl-Histone H3 (Lys4) (C42D8) Rabbit mAb, Cell Signaling 9751, 1:2000
https://www.cellsignal.com/products/primary-antibodies/tri-methyl-histone-h3-lys4-c42d8-rabbit-mab/9751
Tri-Methyl-Histone H3 (Lys27) (C36B11) Rabbit mAb, Cell Signaling 9733, 1:2000
https://www.cellsignal.com/products/primary-antibodies/tri-methyl-histone-h3-lys27-c36b11-rabbit-mab/9733
Acetyl-Histone H3 (Lys27) Rabbit mAb, Cell Signaling 8173, 1:2000
https://www.cellsignal.com/products/primary-antibodies/acetyl-histone-h3-lys27-d5e4-xp-rabbit-mab/8173
Tri-Methyl-Histone H3 (Lys79) Antibody, Cell Signaling 4260, 1:2000
https://www.cellsignal.com/products/primary-antibodies/tri-methyl-histone-h3-lys79-antibody/4260#:~:text=Tri%2DMethyl%2DHistone%20H3%20(Lys79)%20Antibody%20recognizes%20endogenous,%2C%2027%2C%20or%2036).
Di-Methyl-Histone H3 (Lys36) (C75H12) Rabbit mAb, Cell Signaling 2901, 1:2000
https://www.cellsignal.com/products/primary-antibodies/di-methyl-histone-h3-lys36-c75h12-rabbit-mab/2901
Acetyl-Histone H3 (Lys14) (D4B9) Rabbit mAb, Cell Signaling 7627, 1:500
https://www.cellsignal.com/products/primary-antibodies/acetyl-histone-h3-lys14-d4b9-rabbit-mab/7627
Histone H3 Antibody, Cell Signaling 9715, 1:5000
https://www.cellsignal.com/products/primary-antibodies/histone-h3-antibody/9715#:~:text=Histone%20H3%20Antibody%20detects%20endogenous,cross%2Dreact%20with%20other%20histones.
Lamin A + C antibody, GeneTex GTX101126, 1:1000
https://www.genetex.com/Product/Detail/Lamin-A-C-antibody/GTX101126
HIF-1α (C-Term) Polyclonal Antibody, 10006421, Cayman Chemical, 1:200
https://www.caymanchem.com/product/10006421
Acetylated lysine antibody 9441S Cell Signaling, 1:1000
https://www.cellsignal.com/products/primary-antibodies/acetylated-lysine-antibody/9441
Recombinant Anti-Aconitase 2 antibody [EPR8282(B)] ab129069 Abcam, 1:1000
https://www.abcam.com/products/primary-antibodies/aconitase-2-antibody-epr8282b-bsa-and-azide-free-ab248277.html
Anti-SDHB antibody (G-10), sc-271548 Santa Cruz, 1:1000
https://www.scbt.com/fr/p/sdhb-antibody-g-10
Anti-OGDH Antibody GTX33374 Genetex, 1:1000
https://www.genetex.com/Product/Detail/OGDH-antibody/GTX33374

recombinant human Fc-tagged Her2/ErbB2 protein, Sino Biological, 1:200
https://www.sinobiological.com/recombinant-proteins/human-her2-erbb2-10004-h05h
anti-human-Fc Alexa Fluor 488 conjugate, Thermo Fisher Scientific, 1:500
https://www.thermofisher.com/antibody/product/Goat-anti-Human-IgG-Fc-Secondary-Antibody-clone-3H8L9-Recombinant-Monoclonal/A55747
anti-mouse CD62L FITC, MEL-14, Thermo Fisher Scientific, 1:1000
https://www.thermofisher.com/antibody/product/CD62L-L-Selectin-Antibody-clone-MEL-14-Monoclonal/11-0621-82
anti-mouse CD127 PE, SB/199, Biolegend, 1:200
https://www.biolegend.com/nl-be/products/pe-anti-mouse-cd127-il-7ralpha-antibody-3265
anti-mouse CD44 APC-eFluor 780, IM7, Thermo Fisher Scientific, 1:200
https://www.thermofisher.com/antibody/product/CD44-Antibody-clone-IM7-Monoclonal/47-0441-82
anti-mouse KLRG1 PE/Cyanine7, MAFA, Biolegend, 1:200
https://www.biolegend.com/fr-lu/products/pe-cyanine7-anti-mouse-human-klrg1-mafa-antibody-8312
anti-mouse TCF7, C63D9, Cell Signaling, 1:200
https://www.cellsignal.com/products/primary-antibodies/tcf1-tcf7-c63d9-rabbit-mab/2203
anti-mouse Thy1.1 (CD90.1) PE, OX-7, Biolegend, 1:500
https://www.biolegend.com/nl-be/products/pe-anti-rat-cd90-mouse-cd90-1-thy-1-1-antibody-5620
anti-mouse IL2 BV711, JES6-5H4, Biolegend, 1:200
https://www.biolegend.com/fr-ch/products/brilliant-violet-711-anti-mouse-il-2-antibody-10339
anti-mouse IFNg PerCP/Cyanine5.5, XMG1.2, Biolegend, 1:200
https://www.biolegend.com/de-de/products/percp-cyanine5-5-anti-mouse-ifn-gamma-antibody-4433
anti-mouse TNFa Brilliant violet 421, MP6-XT22, Biolegend, 1:200
https://www.biolegend.com/fr-lu/products/brilliant-violet-421-anti-mouse-tnf-alpha-antibody-7336
anti-mouse PD1 (CD279) PerCP/Cyanine5.5, RMP1-30, Biolegend, 1:300
https://www.biolegend.com/fr-ch/products/percp-cyanine5-5-anti-mouse-cd279-pd-1-antibody-12530
anti-mouse TIM3 (CD366) Brilliant Violet 421, RMT3-23, Biolegend, 1:200
https://www.biolegend.com/en-us/products/brilliant-violet-421-anti-mouse-cd366-tim-3-antibody-13392?GroupID=BLG10656
anti-mouse LAG3 PE, C9B7W, Biolegend, 1:200
https://www.biolegend.com/en-us/search-results/pe-anti-mouse-cd223-lag-3-antibody-4486?GroupID=BLG7194
anti-mouse CD45.1 PerCP/Cyanine5.5, A20, Biolegend, 1:200
https://www.biolegend.com/en-us/products/percp-cyanine5-5-anti-mouse-cd45-1-antibody-4269?GroupID=BLG1933
anti-mouse CD45.2 FITC, 104, Biolegend, 1:200
https://www.biolegend.com/en-us/products/fitc-anti-mouse-cd45-2-antibody-6?GroupID=BLG7007
anti-human CD107a (LAMP-1) PE, H4A3, BD, 1:100
https://www.bdbiosciences.com/en-us/products/reagents/flow-cytometry-reagents/research-reagents/single-color-antibodies-ruo/pe-mouse-anti-human-cd107a.560948
anti-granzyme B, PE-texas red, GB11, Invitrogen, 1:200
https://www.thermofisher.com/antibody/product/Granzyme-B-Antibody-clone-GB11-Monoclonal/GRB17
anti-mouse CD71, PE-Cy7, RI7217, Biolegend, 1:200
https://www.biolegend.com/en-us/products/pe-cyanine7-anti-mouse-cd71-antibody-6185?GroupID=BLG4775
anti-mouse CD25, Pacific blue, PC61, Biolegend, 1:200
https://www.biolegend.com/en-us/products/pacific-blue-anti-mouse-cd25-antibody-3315?GroupID=BLG10428
anti-mouse CD27, PerCP/Cyanine5.5, LG.3A10, 1:200
https://www.biolegend.com/nl-be/products/percp-cyanine55-anti-mouse-rat-human-cd27-antibody-4396
anti-human CD3 BV711, UCHT1, Biolegend, 1:200

https://www.biolegend.com/en-ie/products/brilliant-violet-711-anti-human-cd3-antibody-12047
anti-human CD8 BV421, SK1, Biolegend, 1:200
https://www.biolegend.com/nl-be/products/brilliant-violet-421-anti-human-cd8-antibody-13512
anti-human CD45RA BUV395, HI100, BD, 1:200
https://www.bdbiosciences.com/en-us/products/reagents/flow-cytometry-reagents/research-reagents/single-color-antibodies-ruo/buv395-mouse-anti-human-cd45ra.740298#:~:text=The%20CD45RA%20antigen%20is%20expressed,%E2%84%A2%20Ultraviolet%20family%20of%20dyes.
anti-human CD45RO BUV805, UCHL1, BD, 1:200
https://www.bdbiosciences.com/en-at/products/reagents/flow-cytometry-reagents/research-reagents/single-color-antibodies-ruo/buv805-mouse-anti-human-cd45ro.748367
anti-human CD62L PerCP/Cyanine5.5, DREG-56, Biolegend, 1:200
https://www.biolegend.com/en-us/products/percp-cyanine5-5-anti-human-cd62l-antibody-4243?GroupID=BLG10270
anti-human CCR7 (CD197) Pacific Blue, G043H7, Biolegend, 1:100
https://www.biolegend.com/en-us/products/pacific-blue-anti-human-cd197-ccr7-antibody-7526?GroupID=BLG9613
anti-human CD95 PE, DX2, BD, Thermo Fisher Scientific, 1:200
https://www.fishersci.fr/shop/products/anti-cd95-pe-clone-dx2-bd/15838768/en
anti-human CD27 BV605, LG.3A10, Biolegend, 1:200
https://www.biolegend.com/fr-lu/search-results/brilliant-violet-605-anti-mouserathuman-cd27-antibody-19163
anti-human CD28 PE/Cyanine7, S20013B, Biolegend, 1:100
https://www.biolegend.com/en-us/products/pe-cyanine7-anti-human-cd28-antibody-22709
anti-human CD271 APC, ME20.4, Biolegend, 1:200
https://www.biolegend.com/fr-ch/products/apc-anti-human-cd271-ngfr-antibody-6877#:~:text=CD271%2C%20also%20known%20as%20p75NTR,follicular%20dendritic%20cells%20and%20melanocytes.
anti-human HER2 (CD340) Brilliant Violet 421, 24D2, Biolegend, 1:500
https://www.biolegend.com/en-us/products/brilliant-violet-421-anti-human-cd340-erbb2-her-2-antibody-9879?GroupID=BLG5136
Live/dead fixable Aqua Dead cell stain kit, Lifetechnologies, 1:1000
https://www.thermofisher.com/order/catalog/product/L34957?s_kwcid=AL!3652!3!606658601477!p!!g!!live%20dead%20fixable%20aqua&ef_id=Cj0KCQjw756lBhDMARIsAEI0Agm3HqyizAf84ODsH7k3vpqP6oEUnb-b6FACC_JosbLoH5UcNaWrGyEaAogqEALw_wcB:G:s&s_kwcid=AL!3652!3!606658601477!p!!g!!live%20dead%20fixable%20aqua!381166034!75094255831&cid=bid_pca_frg_r01_co_cp1359_pjt0000_bid00000_0se_gaw_bt_pur_con&gclid=Cj0KCQjw756lBhDMARIsAEI0Agm3HqyizAf84ODsH7k3vpqP6oEUnb-b6FACC_JosbLoH5UcNaWrGyEaAogqEALw_wcB
MitoSOX Red Mitochondrial Superoxide Indicator M36008 Invitrogen
https://www.thermofisher.com/order/catalog/product/M36008
BODIPY 493/503 (4,4-Difluoro-1,3,5,7,8-Pentamethyl-4-Bora-3a,4a-Diaza-s-Indacene, D3922 Thermofisher, 1:5000
https://www.thermofisher.com/order/catalog/product/D3922?ef_id=Cj0KCQjw756lBhDMARIsAEI0Agka9Tl_HAOHMJSj9vyvETMCNL4UjLNJ4nw0M1BwwBNdd37aG-Rl86UaAmFUEALw_wcB:G:s&s_kwcid=AL!3652!3!447292198730!!!g!!!10506731179!109642167491&cid=bid_pca_iva_r01_co_cp1359_pjt0000_bid00000_0se_gaw_dy_pur_con&gclid=Cj0KCQjw756lBhDMARIsAEI0Agka9Tl_HAOHMJSj9vyvETMCNL4UjLNJ4nw0M1BwwBNdd37aG-Rl86UaAmFUEALw_wcB
Filipin III, SAE0087 Sigma-Aldrich, 1:100
https://www.sigmaaldrich.com/CH/en/product/sigma/sae0087

Validation

All antibodies are commercially available and were validated by the manufacturers as documented on the website of the company.

Eukaryotic cell lines

Policy information about cell lines

Cell line source(s)	Yumm1.7, B16-F10 melanoma cells, Phoenix-Eco cells, 293T cells were obtained from the American Type Culture Collection.
Authentication	None of the cell lines were authenticated in these studies, but low passage number cell lines were utilized.
Mycoplasma contamination	All the cell lines are mycoplasma-free and were systematically tested for mycoplasma contamination.
Commonly misidentified lines (See ICLAC register)	No commonly misidentified lines were used.

Animals and other organisms

Policy information about studies involving animals; ARRIVE guidelines recommended for reporting animal research

Laboratory animals	C57BL/6 (B6) (CD45.2) mice were purchased from Charles River (France). Cd4-Cre (B6.Cg-Tg(Cd4-cre)1Cwi/BfluJ), whole body Cas9 (B6J.129(Cg)- Gt(ROSA)26Sortm1.1(CAG-cas9*,-EGFP)Fezh/J) and conditional Cas9 or Rosa26-LSL-Cas9 knock-in (B6;129-Gt(ROSA)26Sortm1(CAG-cas9*,-EGFP)Fezh/J) mice were bought from the Jackson Laboratory and bred in-house. OT1 T cell receptor (TCR) transgenic mice, expressing a TCR specific for the chicken egg ovalbumin SIINFEKL epitope in the context of H2Kb and CRISPR–Cas9 knock-in OT1 TCR-transgenic mice were obtained by crossing of Rosa26-LSL-Cas9 knock-in mice with Cd4-Cre mice on an OT1 background.

	NOD-SCID-gc−/− (NSG) mice (6 to 8 weeks old) were purchased from the Jackson laboratory and were bred and maintained at the animal facility of the University of Lausanne. CD4Cre+/wtTfamfl/fl mouse splenocytes were kindly gifted by the laboratory of prof. María Mittelbrunn (Madrid, Spain) and IDH2 whole body knockout mouse splenocytes by the laboratory of prof. Seung-Soon Im (Daegu, South Korea). Males and females between 6 to 10 weeks old were used for experiments and were age and sex matched for ACT experiments. Mice were kept in the SPF animal facility of the University of Lausanne in individually ventilated cages, between 19-23 °C with 45-65% humidity and a 12hour dark/light cycle.
Wild animals	No wild animals were involved
Field-collected samples	No samples were field-collected
Ethics oversight	Experimentation was performed in respect of protocols approved by the veterinary authorities of the Canton de Vaud (VD2688.2, VD3763b, VD3390x1e).

Note that full information on the approval of the study protocol must also be provided in the manuscript.

Human research participants

Policy information about studies involving human research participants

Population characteristics	Fresh peripheral blood from healthy human donors, males and females between 20 to 60 years old, was collected, followed by density centrifugation to obtain bulk peripheral blood mononuclear cells (PBMCs) Bone marrow samples were obtained from multiple myeloma patients at the Lausanne University Hospital under an approved research protocol. Malignant plasma cells were separated from whole bone marrow by performing a CD138 positive selection with beads (EasySep, #17877). The positive fraction containing CD138+ cells and the negative fraction containing marrow infiltrating lymphocytes and other cells were frozen using 40% RPMI 1640 (Gibco, #61870010), 50% Fetal bovine serum ((FBS) Gibco, #10270-106; lot: 2166446) and 10% DMSO (Sigma-Aldrich, #41639) and stored in liquid nitrogen until use. The negative fraction was used in these experiments.
Recruitment	Fresh PBMCs were obtained from healthy human volunteers of unknown sex and age at the Interregional Transfusion Center of Switzerland. Therefore a bias might be present towards individuals younger than 60 years. Bone marrow samples were obtained from multiple myeloma patients at the Lausanne University Hospital, amplified and frozen before use in experiments. Only successfully amplified samples were used, which might have created a bias towards patients with "fitter" starting material.
Ethics oversight	Commission cantonale d'éthique de la recherche sur l'être humain (CER-VD) at Lausanne University Hospital (CHUV)

Note that full information on the approval of the study protocol must also be provided in the manuscript.

Flow Cytometry

Plots

Confirm that:

☒ The axis labels state the marker and fluorochrome used (e.g. CD4-FITC).

☒ The axis scales are clearly visible. Include numbers along axes only for bottom left plot of group (a 'group' is an analysis of identical markers).

☒ All plots are contour plots with outliers or pseudocolor plots.

☒ A numerical value for number of cells or percentage (with statistics) is provided.

Methodology

Sample preparation	Tumours were dissected, single cell suspensions were obtained using Mouse Tumour Dissociation Kit (Miltenyi, 130–096-730) following the manufacturer protocol. Draining lymph nodes and spleens were smashed on a 70µm cell strainer. Antibody staining was done on single cell suspensions for flow cytometry analysis. Staining for flow cytometry was done in PBS with 2% FBS and 2mM EDTA, at 4°C in the dark. The Life/Dead Fixable Blue Cell Stain Kit (Thermo Fisher Scientific) was used to mark dead cells. The Foxp3 staining kit (Thermo Fisher Scientific) was used for intracellular staining, following the manufacturer's instructions.
Instrument	Acquisition was done on LSR II, Fortessa and Cytek Aurora flow cytometers. In vivo imaging was done using the Xenogen in vivo imaging system (IVIS) (Caliper Life Sciences).
Software	BD FACSDiva was used for data acquirement and FlowJo v10.8.1 was used to analyse flow cytometry data.
Cell population abundance	All analysis have been performed on a population that included between 20 and 10000 cells, depending on initial material abundance.
Gating strategy	Transferred CD8 T cells were discriminated from CD45.2+ hosts by their expression of the CD45.1 marker. Short-lived effector cells (SLECs) were defined as live, CD8+, KLRG1+, CD127-

Memory precursor effector cells (MPECs) were defined as live, CD8+, KLRG1-, CD127+
Central memory CD8 T cells were defined as live, CD8+, CD44+, CD62L+
Effector memory CD8 T cells were defined as live, CD8+, CD44+, CD62L-
Transduced cells were identified by their Thy1.1 (CD90.1) or their HER2 expression.
Progenitor exhausted CD8 T cells were defined as CD8+, PD1+, TCF1+
Terminally exhausted CD8 T cells were defined as CD8+, PD1+, TCF1-
Human stem cell memory T (Tscm) cells were defined as CD45RA+, CD62L+, CD45RO-, CCR7+, CD95+, CD28+, CD27+.

☒ Tick this box to confirm that a figure exemplifying the gating strategy is provided in the Supplementary Information.